

Article

Computationally Efficient Force and Moment Models for Propellers in UAV Forward Flight Applications

Rajan Gill * and Raffaello D'Andrea

Institute for Dynamic Systems and Controls, ETH Zurich, 8092 Zurich, Switzerland; rdandrea@ethz.ch

* Correspondence: rgill@ethz.ch

Received: 18 September 2019; Accepted: 5 October 2019; Published: 8 October 2019



Abstract: Two low-order, parametric models are developed for the forces and moments that a rotating propeller undergoes in forward flight. The models are derived using a first-principles-based approach, and are computationally efficient in the sense of being represented by explicit expressions. The parameters for the models can be identified either using supervised learning/grey-box fitting from labelled data, or can be predicted using only the static load coefficients (i.e., the hover thrust and torque coefficients). The second model is a multinomial model that is derived by means of a Taylor series expansion of the first model, and can be viewed as a lower-order lumped parameter model. The models and parameter generation methods are experimentally tested against 19 propellers tested in a wind tunnel under oblique flow conditions, for which the data is made available. The models are tested against 181 additional propellers from existing datasets.

Keywords: propeller; parametric model; grey-box identification; oblique flow dataset

1. Introduction

Aerodynamic models of a rotating propeller in forward flight can be broadly classified into two categories. The first category is high fidelity models that may involve a fluid dynamics simulation and uses relatively high compute power to resolve. These models are typically used to aid the design of the propeller and/or vehicle [1–3]. The other category, which is the focus herein, are low-order yet computationally efficient models that can make use of experimental data for grey-box identification. There is a lack of literature on the latter category, as noted in [4–7], especially for vertical take-off and landing (VTOL) unmanned aerial vehicles (UAVs) due to the wide operating regime spanning hover, axial, and oblique flows. Such models would be useful for model-based control and state estimation [8–10], where only the salient features need to be captured, and can improve the fidelity of simulations of UAV control systems.

Specifically, the goal herein is to derive parametric models via first-principles for the propeller thrust F_T , “H-force” (sometimes referred to as rotor drag) [11,12] F_H , rotor torque M_Q , rolling moment M_R , and pitching moment M_P (see Figure 1; the lateral/side force F_S is two orders of magnitude smaller than the thrust, as can be seen in Supplementary Dataset S1, and thus is assumed to be negligible), given a propeller’s rotation rate Ω , incoming wind speed V and angle between the rotor plane and incoming wind β , to a reasonable degree of accuracy. That is,

$$(\Omega, V, \beta) \mapsto (F_T, F_H, M_Q, M_R, M_P) \quad (1)$$

where the above map is given as an explicit expression of its arguments Ω , V and β . That is, no implicit equations, no numerical computation of integrals, etc. This is a useful attribute because explicit expressions are simple and typically fast to compute and have low memory footprint. The benefit of such grey-box models is that they are good at extrapolating measurement data (compared to a

black-box approach). For instance, as will be shown in Section 4.2, the parameters to the model can be learned only from the hover thrust and torque coefficients, resulting in good extrapolation of the loads in the forward flight operating regime.

This paper is organized as follows:

- Sections 2 and 3: a first-principles-based analytical model is derived for (1). This model is parametrized by nine parameters, which can either be optimized over using labelled data generated from flight experiments as in [13–15], or against wind tunnel data as will be done herein. In contrast to the literature, this section provides a consolidated and analytical grey-box model for (1) without limiting restrictions on β . To the best of the authors' knowledge, such a model does not exist in the literature. Additionally, wind tunnel tests were performed, generating a dataset consisting of 19 propellers under oblique flow ($\beta \neq 0$), for which the models will be tested against. This dataset can be found in Supplementary Dataset S1. The models will be additionally tested against existing datasets which are predominately for axial flow ($\beta \equiv 0$).
- Section 4: an algorithm for which the nine parameters can be predicted using only the static thrust and torque coefficients (i.e., the hover model). Again, this approach is assessed with the full wind tunnel dataset. To the best of the authors' knowledge, such an approach has not been explored in the literature.
- Section 5: a second-order Taylor series expansion is performed to yield a simplified lumped-parameter model. The contribution of this section over a brute-force, black-box multinomial surface fitting approach is that, based on the first-principles model, some terms disappear in the Taylor expansion, resulting in a reduced multinomial that is physically motivated. Again, this has not been done in the literature to the best of the authors' knowledge, and the approach is assessed with the wind tunnel data.

The assessment against the wind tunnel data for each section not only assesses the quality of the models, but also provides a typical range of values for the parameters.

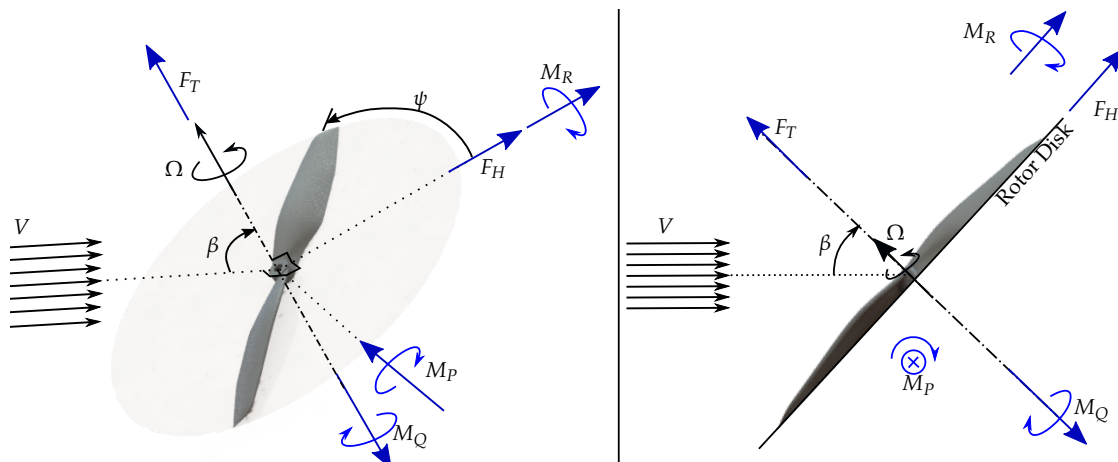


Figure 1. A counter-clockwise propeller rotating at a rate of Ω , with incident wind with speed V forming an angle β with the rotor plane normal. ψ is the azimuth angle of the propeller blade. The left figure is a 3D view and the figure on the right is a 2D side view. Note that the direction of the incoming flow is perpendicular to the direction of pitching moment M_P , which is perpendicular to the direction of H-force F_H (and rolling moment M_R), which is perpendicular to the direction of thrust F_T (and rotor torque M_Q). The forces act at the centre of the rotor disk. For a clockwise propeller, the directions of assumed positive rotor torque and rolling moment are flipped. The lateral or side force F_S (in the direction of the pitching axis), is assumed to be negligible and is indeed the case in experiments, see Supplementary Dataset S1 and Figure 6.

Literature Review

In the context of control of multirotor vehicles, the typical modelling approach has been to use a hover or ‘static’ model, that is, the thrust and rotor torque are proportional to the square of the propeller rotation rate, and to neglect H-force, pitching and rolling moments [16–33]. As shown in [15], this model breaks down when a quadrotor flies at moderate speeds. Thus in such cases, feedback control is relied upon to achieve adequate tracking.

In [9,10], model-based state estimation was improved upon by incorporating some of the forward flight effects of the propeller, namely the H-force F_H (though this model still differs to the H-force models proposed herein). Furthermore, when considering the reduction in thrust F_T in forward flight, one approach is to use momentum theory and Glauert’s flow model for helicopter rotors to yield an implicit equation for the induced flow that must be solved numerically [11,34–37]. This has been used in [38,39] to develop a thrust model as a function of the ideal power consumption of the rotor. This has also been used in [12] to model the thrust, H-force, and rotor torque for a helicopter rotor. In [35], building on [36], some simplifying assumptions are used in the context of helicopter rotors (e.g., $\beta \approx \pi/2$) to derive an analytical model for the thrust. A similar modelling assumption is used in [40], yielding a model (with M_P neglected) that was used in [41] for improving the simulation of a quadrotor. In addition, a wind estimation algorithm using a quadrotor was developed in [42], where the rotor thrust was modelled using a black-box model using wind tunnel data.

In the context of fixed-wing aircraft control, some works forego the modelling task and elect to rely solely on feedback for thrust tracking, which has been shown to work for nominal cruise conditions [43–47]. Others also use the hover model mentioned earlier [48–50]. In [51–54], a black-box modelling approach is performed by using data from flight experiments and assuming a linear system about a specific operating point in order to achieve better closed-loop control performance.

Other fixed-wing works, such as [55,56], use a black-box modelling approach given wind tunnel data for the thrust F_T and under axial flow conditions. In particular, it is stated in [55] that no physical explanation can be provided for their thrust model. In [57], a look-up table is used based on thrust values provided by the propeller’s manufacturer for various flight speeds under axial flow. Similarly, a look-up table approach is used in [58] to enhance the fidelity of flight simulations, where the values are generated under axial conditions for the thrust F_T and torque M_Q using computational software. In [59,60], a model for F_T is used that takes into account some of the forward flight effects under axial flow conditions. In [61], attitude control was improved upon by incorporating the forward flight effects of the propeller using a grey-box model, but the modelling was done for a fixed angle of attack.

Recently, a few works have used blade element theory (BET) [5,6,14,15,62–66], usually in conjunction with the Glauert flow model [34] for both axial and oblique flow conditions, resulting in models with no closed form expressions. Additionally, the models are fragmented in the literature, with some focusing only on the axial flow condition, and others only considering a subset of the outputs in (1). In [13], a combination of first-principles and black-box modelling using stepwise regression was used given flight performance data. This is similar to our previous work [15], but the models were quite computationally expensive in the sense that they were not representable by analytical expressions, and thus must be solved numerically.

Performance data was gathered from wind tunnel experiments for a UAV and an isolated propeller in [67], and it was noted that there is a lack of published data for the aerodynamic performance for UAVs in general. In [58,68,69], a thorough wind tunnel data collection was performed for axial flow, resulting in a database for 180 different propellers. An additional wind tunnel measurement campaign was performed in [7] for both axial and oblique flow for a single propeller. All the models proposed herein will be assessed against these datasets, as well as against 19 additional propellers that were tested in a wind tunnel under oblique flow conditions (see Supplementary Dataset S1).

2. First-Principles Derivation

The overall derivation involves a blade element approach, where the propeller blade is divided into infinitesimal segments. A quasi-steady flow assumption is used, in the sense that the fluid equilibrates at a negligible time constant with respect to the time period of the propeller rotation. Furthermore, each blade segment is assumed to be independent of other segments in the sense that the flow around each segment can be viewed as being purely two-dimensional. This approach will be combined with momentum theory in Section 2.6 to resolve further variables in the model, namely the induced inflow. For convention, the direction of positive forces and moments are fixed and shown in Figure 1. Only the forward flight scenario is considered, that is $V \geq 0$, $\beta \in [-\pi/2, \pi/2]$, and $\Omega > 0$.

Consider now an infinitesimal blade segment at a distance $y \in [0, R]$ from the centre of the propeller, and let the segment have a width of dy (see Figure 2). Then, the components of the air velocity U_{\parallel} , U_{\perp} , as defined in Figure 2, with respect to the moving blade segment are given by

$$U_{\parallel}(\Omega, V, \beta, y, \psi) = \Omega y + V \sin(\beta) \sin(\psi) \quad (2)$$

$$U_{\perp}(V, \beta, v_i) = V \cos(\beta) + v_i \quad (3)$$

where v_i is the induced inflow velocity through the rotor disk and is in a direction perpendicular to the rotor disk [34], and in the tangential direction is assumed to be negligible (see Section 2.6). It is assumed that the induced inflow is uniformly distributed across the rotor disk. The flow angle ϕ in Figure 2 is given by

$$\phi(\Omega, V, \beta, y, \psi, v_i) = \arctan 2 \left(U_{\perp}(\Omega, V, \beta, y, \psi), U_{\parallel}(V, \beta, v_i) \right) \quad (4)$$

The effects of blade flapping [10] have been ignored in the above. Simple models is one of the goals herein, and assuming that the UAV propellers are rigid enough to mitigate flapping effects will prove to be a good enough assumption as the models behave well in experiments. However, extending the derivation to include blade flapping effects to improve the models, especially for soft propellers, may be an interesting direction for future work.

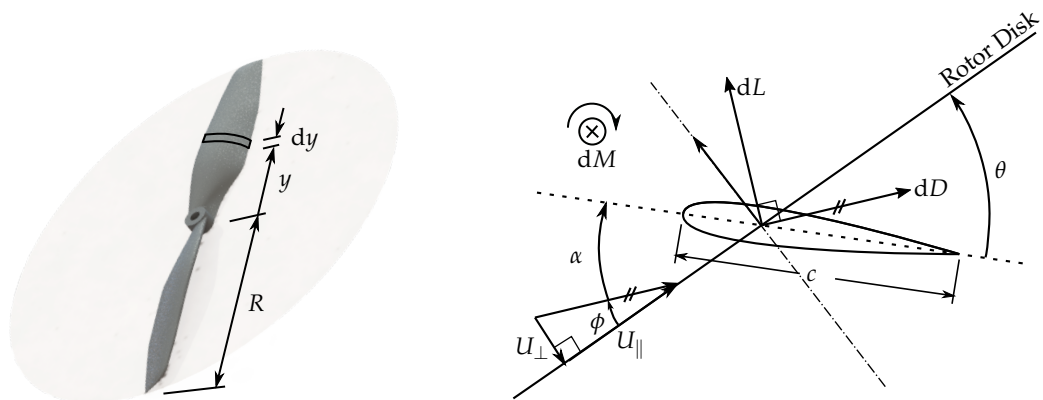


Figure 2. An infinitesimal blade element (right) located at a distance y from the rotor centre with width dy . α is the angle of attack of the blade element, c is its chord length, and θ is the pitch angle, the angle of the blade element's chord line [70] with respect to the rotor disk. The infinitesimal loads of the blade element are the lift dL , drag dD , and pitching moment dM .

Henceforth it will be convenient to work in normalized units. First define the following:

$$r := y/R \quad (5)$$

$$\lambda_c := V \cos(\beta) / (\Omega R) \quad (6)$$

$$\lambda_i := v_i / (\Omega R) \quad (7)$$

$$\mu := V \sin(\beta) / (\Omega R) \quad (8)$$

$$\lambda := \lambda_c + \lambda_i \quad (9)$$

where μ is known as the advance ratio, λ_c the climb ratio, and λ_i the induced inflow ratio [34]. Thus by dividing both U_{\parallel} and U_{\perp} in (4) by ΩR , (4) becomes

$$\phi(\lambda_c, \mu, \lambda_i, r, \psi) = \arctan 2(\lambda, r + \mu \sin(\psi)) \quad (10)$$

Occasionally functions will be overloaded as such, and it should be clear from context (i.e., the input variables) which function is being referred to. Henceforth the approximation that $U_{\parallel} \gg U_{\perp}$ is made, such that

$$\phi(\lambda_c, \mu, \lambda_i, r, \psi) = \frac{\lambda}{r + \mu \sin(\psi)} \quad (11)$$

This assumption is not true everywhere on the rotor disk (i.e. for all r and ψ) and for all λ_c, μ , and a corresponding discussion is provided in Section 2.8. Nevertheless, this assumption is used in order to develop low order, computationally efficient maps. The local angle of attack, α , of the infinitesimal blade element is then given by

$$\alpha(\lambda_c, \mu, \lambda_i, r, \psi) = \theta(r) - \phi(\lambda_c, \mu, \lambda_i, r, \psi) \quad (12)$$

where $\theta(r)$ is the pitch angle of the blade element located at a distance $y = Rr$ from the centre.

Under the quasi-steady flow assumption, and again under the assumption that $U_{\parallel} \gg U_{\perp}$, the aerodynamic lift, drag, and pitching moment of the blade element are governed by the following standard formulae [70]:

$$dL(\Omega, V, \beta, y, \psi, v_i) \approx \frac{1}{2} \rho U_{\parallel}(\Omega, V, \beta, y, \psi)^2 C_L(\alpha(\Omega, V, \beta, y, \psi, v_i)) c(y/R) dy \quad (13)$$

$$dD(\Omega, V, \beta, y, \psi, v_i) \approx \frac{1}{2} \rho U_{\parallel}(\Omega, V, \beta, y, \psi)^2 C_D(\alpha(\Omega, V, \beta, y, \psi, v_i)) c(y/R) dy \quad (14)$$

$$dM(\Omega, V, \beta, y, \psi, v_i) \approx \frac{1}{2} \rho U_{\parallel}(\Omega, V, \beta, y, \psi)^2 C_M(\alpha(\Omega, V, \beta, y, \psi, v_i)) c(y/R)^2 dy \quad (15)$$

where ρ is the air density and $c(y/R)$ is the chord length of the blade element located a distance y from the centre of the propeller. The above can be normalized to yield the loads in dimensionless units:

$$dL_N(\lambda_c, \mu, r, \psi, \lambda_i) := \frac{dL(\Omega, V, \beta, y, \psi, v_i)}{\frac{1}{2} \rho A(\Omega R)^2} = \frac{c(r)}{\pi R} (r + \mu \sin(\psi))^2 C_L(\alpha(\lambda_c, \mu, \lambda_i, r, \psi)) dr \quad (16)$$

$$dD_N(\lambda_c, \mu, r, \psi, \lambda_i) := \frac{dL(\Omega, V, \beta, y, \psi, v_i)}{\frac{1}{2} \rho A(\Omega R)^2} = \frac{c(r)}{\pi R} (r + \mu \sin(\psi))^2 C_D(\alpha(\lambda_c, \mu, \lambda_i, r, \psi)) dr \quad (17)$$

$$dM_N(\lambda_c, \mu, r, \psi, \lambda_i) := \frac{dL(\Omega, V, \beta, y, \psi, v_i)}{\frac{1}{2} \rho A(\Omega R)^2 R} = \frac{c(r)^2}{\pi R^2} (r + \mu \sin(\psi))^2 C_M(\alpha(\lambda_c, \mu, \lambda_i, r, \psi)) dr \quad (18)$$

where $A = \pi R^2$ is the rotor disk area.

The lift, drag, and pitching moment coefficients are assumed to be of the form

$$C_L(\alpha) = c_{l,0} + c_{l,\alpha}\alpha \quad (19)$$

$$C_D(\alpha) = c_{d,0} + c_{d,\alpha}\alpha^2 \quad (20)$$

$$C_M(\alpha) = c_{m,0} + c_{m,\alpha}\alpha \quad (21)$$

The $c_{l,0}$ and $c_{m,0}$ terms are needed as the airfoils for UAV propellers are typically very positively cambered [70]. Furthermore, such models may not be valid for high-pitch propellers operating at low speeds, thereby operating in the stall regime; an approach similar to [15] could be used, but would then result in more computationally complex models.

We must also assume a form for the propeller geometry, that is, $\theta(\cdot)$ and $c(\cdot)$. Henceforth the following will be used:

$$\theta(r) = \begin{cases} \frac{\theta_{\text{tip}}}{r} & 1 \geq r \geq \delta \\ 0 & \text{else} \end{cases} \quad (22)$$

$$c(r) = \begin{cases} \frac{c_{\text{tip}}}{r} & 1 \geq r \geq \delta \\ 0 & \text{else} \end{cases} \quad (23)$$

where $\delta \in (0, 1)$ is a parameter that represents the fraction of the propeller blade that is “not useful” [34]. The inverse relationship represents the ideal geometry for minimizing power consumption for hover and axial flight [34]. This chord model, however, is not the case for some propellers, notably APC’s slow-fly series, or micro UAV propellers that typically have a constant chord model. Thus, one could use another parametrization, e.g., as in [40] which uses a linear twist profile, instead of the ones above using additional parameters, or use a specific model for a specific propeller. Nevertheless, (22) and (23) are used for simplicity.

2.1. Thrust F_T

The infinitesimal thrust of the rotor, in dimensionless units, is given by

$$N_b(dL_N \cos(\phi) - dD_N \sin(\phi)) \approx N_b dL_N \quad (24)$$

where N_b is the number of blades the propeller has, and the approximation on the right-hand side comes from assuming $dL \gg dD$, and enforcing the prior assumption that ϕ is small as in (11). Integrating the above with respect to r yields the normalized thrust C_{FT} as a function of the azimuth angle ψ :

$$C_{FT}(\lambda_c, \mu, \lambda_i, \psi) = N_b \int_0^1 \frac{dL_n(\lambda_c, \mu, r, \psi, \lambda_i)}{dr} dr \quad (25)$$

However, in general, knowing the loads as a function of ψ is not so interesting, as the propeller rotates at high rates; one generally cares about the average thrust produced (although it is important to keep this in mind, as the varying loads can excite vibrational modes of a system [71,72], and may be observed using an approach as in [73]). Thus the average thrust over a complete rotation of the propeller is given by

$$C_{FT}(\lambda_c, \mu, \lambda_i) = \frac{1}{2\pi} \int_0^{2\pi} C_{FT}(\lambda_c, \mu, \lambda_i, \psi) d\psi \quad (26)$$

$$= \frac{1}{2\delta} \sigma \left((1 - \delta) \left(c_{l,0} \delta (1 + \delta) - 2c_{l,\alpha} \delta (\lambda - \theta_{\text{tip}}) + c_{l,\alpha} \mu^2 \theta_{\text{tip}} \right) - c_{l,0} \delta \mu^2 \ln(\delta) \right) \quad (27)$$

where $\sigma := \frac{N_b c_{\text{tip}}}{\pi R}$ is the solidity ratio [34].

Note that the average thrust in dimensioned units can be recovered by multiplying by the normalization constant:

$$F_T(\Omega, V, \beta, v_i) = \frac{1}{2} \rho \pi R^2 (\Omega R)^2 C_{FT}(\lambda_c, \mu, \lambda_i) \quad (28)$$

In Section 2.6, the induced inflow $v_i \sim \lambda_i$ will be determined analytically as a function of Ω, V, β , so as to conform with the goal (1).

2.2. H-Force F_H

The infinitesimal H-force, in dimensionless units, is given by

$$N_b (dL_N \sin(\phi) + dD_N \cos(\phi)) \sin(\psi) \approx N_b (dL_N \phi + dD_N) \sin(\psi) \quad (29)$$

where the usual approximations are applied to yield the right hand side. Integrating with respect to r yields the normalized H-force C_{FH} as a function of ψ :

$$C_{FH}(\lambda_c, \mu, \lambda_i, \psi) = N_b \int_0^1 \left(\frac{dL_N(\lambda_c, \mu, \lambda_i, r, \psi)}{dr} \phi(\lambda_c, \mu, \lambda_i, r, \psi) + \frac{dD_N(\lambda_c, \mu, \lambda_i, r, \psi)}{dr} \right) \quad (30)$$

$$\sin(\psi(\lambda_c, \mu, \lambda_i, r, \psi)) dr \quad (31)$$

The average H-force over a complete rotation of the propeller is given by

$$C_{FH}(\lambda_c, \mu, \lambda_i) = \frac{1}{2\pi} \int_0^{2\pi} C_{FH}(\lambda_c, \mu, \lambda_i, \psi) d\psi \quad (32)$$

$$= \frac{1}{2\delta} \mu \sigma ((1 - \delta) (2c_{d,0}\delta + \theta_{tip} ((c_{l,\alpha} - 2c_{d,\alpha})\lambda + 2c_{d,\alpha}\theta_{tip})) - c_{l,0}\delta\lambda \ln(\delta)) \quad (33)$$

Similarly, the lateral force F_S given by $(dL \sin(\phi) + dD \cos(\phi)) \cos(\psi) \approx (dL\phi + dD) \cos(\psi)$ can be shown to be 0 on average (for a constant λ_i across the rotor disk as in this case).

2.3. Rotor Torque M_Q

The infinitesimal rotor torque, in dimensionless units, is given by

$$N_b (dL_N \sin(\phi) + dD_N \cos(\phi)) r \approx N_b (dL_N \phi + dD_N) r \quad (34)$$

Integrating with respect to r yields the normalized rotor torque C_{MQ} as a function of ψ :

$$C_{MQ}(\lambda_c, \mu, \lambda_i, \psi) = N_b \int_0^1 \left(\frac{dL_N(\lambda_c, \mu, \lambda_i, r, \psi)}{dr} \phi(\lambda_c, \mu, \lambda_i, r, \psi) + \frac{dD_N(\lambda_c, \mu, \lambda_i, r, \psi)}{dr} \right) r dr \quad (35)$$

The average rotor torque over a complete rotation of the propeller is given by

$$C_{MQ}(\lambda_c, \mu, \lambda_i) = \frac{1}{2\pi} \int_0^{2\pi} C_{MQ}(\lambda_c, \mu, \lambda_i, \psi) d\psi \quad (36)$$

$$= \frac{1}{6} (1 - \delta) \sigma (2c_{d,0} (1 + \delta + \delta^2) + 3c_{l,0}(\delta + 1)\lambda + \quad (37)$$

$$6 (c_{d,\alpha}(\lambda - \theta_{tip}) - c_{l,\alpha}\lambda) (\lambda - \theta_{tip}) + \frac{3\mu^2 (c_{d,0}\delta + c_{d,\alpha}\theta_{tip}^2)}{\delta} \quad (38)$$

2.4. Rolling Moment M_R

The infinitesimal rolling moment, in dimensionless units, is given by

$$N_b (\mathrm{d}L_N \cos(\phi) - \mathrm{d}D_N \sin(\phi)) r \sin(\psi) \approx N_b \mathrm{d}L_N r \sin(\psi) \quad (39)$$

Integrating with respect to r yields the normalized rolling moment C_{MR} as a function of ψ :

$$C_{MR}(\lambda_c, \mu, \lambda_i, \psi) = N_b \int_0^1 \frac{\mathrm{d}L_N(\lambda_c, \mu, \lambda_i, r, \psi)}{\mathrm{d}r} r \sin(\psi(\lambda_c, \mu, \lambda_i, r, \psi)) \mathrm{d}r \quad (40)$$

The average rolling moment over a complete rotation of the propeller is given by

$$C_{MR}(\lambda_c, \mu, \lambda_i) = \frac{1}{2\pi} \int_0^{2\pi} C_{MR}(\lambda_c, \mu, \lambda_i, \psi) \mathrm{d}\psi \quad (41)$$

$$= \frac{1}{2}(1 - \delta)\sigma\mu (c_{l,0}(\delta + 1) - c_{l,\alpha}(\lambda - 2\theta_{\text{tip}})) \quad (42)$$

2.5. Pitching Moment M_P

The infinitesimal pitching moment, in dimensionless units, is given by

$$N_b (\mathrm{d}M_N \sin(\psi) - (\mathrm{d}L_N \cos(\phi) - \mathrm{d}D_N \sin(\phi)r \cos(\psi))) \approx N_b (\mathrm{d}M_N \sin(\psi) - \mathrm{d}L_N r \cos(\psi)) \quad (43)$$

Integrating with respect to r yields the normalized pitching moment C_{MP} as a function of ψ :

$$C_{MP}(\lambda_c, \mu, \lambda_i, \psi) = N_b \int_0^1 \left(\frac{\mathrm{d}M_N(\lambda_c, \mu, \lambda_i, r, \psi)}{\mathrm{d}r} \sin(\psi(\lambda_c, \mu, \lambda_i, r, \psi)) - \right. \quad (44)$$

$$\left. \frac{\mathrm{d}L_N(\lambda_c, \mu, \lambda_i, r, \psi)}{\mathrm{d}r} r \cos(\psi(\lambda_c, \mu, \lambda_i, r, \psi)) \right) \mathrm{d}r \quad (45)$$

The average pitching moment over a complete rotation of the propeller is given by

$$C_{MP}(\lambda_c, \mu, \lambda_i) = \frac{1}{2\pi} \int_0^{2\pi} C_{MP}(\lambda_c, \mu, \lambda_i, \psi) \mathrm{d}\psi \quad (46)$$

$$= \frac{c_{\text{tip}}}{2\delta R} \sigma\mu (c_{m,\alpha}(\delta - 1)(\lambda - 2\theta_{\text{tip}}) - 2c_{m,0}\delta \ln(\delta)) \quad (47)$$

2.6. Induced Inflow λ_i

A two-dimensional Eulerian control volume analysis [70] is used to determine the induced inflow ratio λ_i (see Figure 3), assuming a steady, adiabatic and isentropic process (i.e., neglecting viscous effects). It is important to be aware that assuming an isentropic flow is not a good assumption when there is drag, however, only an approximation is sought here. Note that the control volume herein differs from the approaches in the literature, which use the Glauert flow model (which itself has no rigorous basis for its use [34]) which in the end yields an implicit equation for the induced inflow v_i , for which no closed form expression exists.

The mass flow rate is

$$\dot{m} = \iint_0 \rho \langle \vec{v}, \mathrm{d}\vec{s} \rangle = \iint_2 \rho \langle \vec{v}, \mathrm{d}\vec{s} \rangle = \iint_3 \rho \langle \vec{v}, \mathrm{d}\vec{s} \rangle \quad (48)$$

$$= \rho A_0 V = \rho A(v_i + V \cos(\beta)) = \rho A_3 V_3 \quad (49)$$

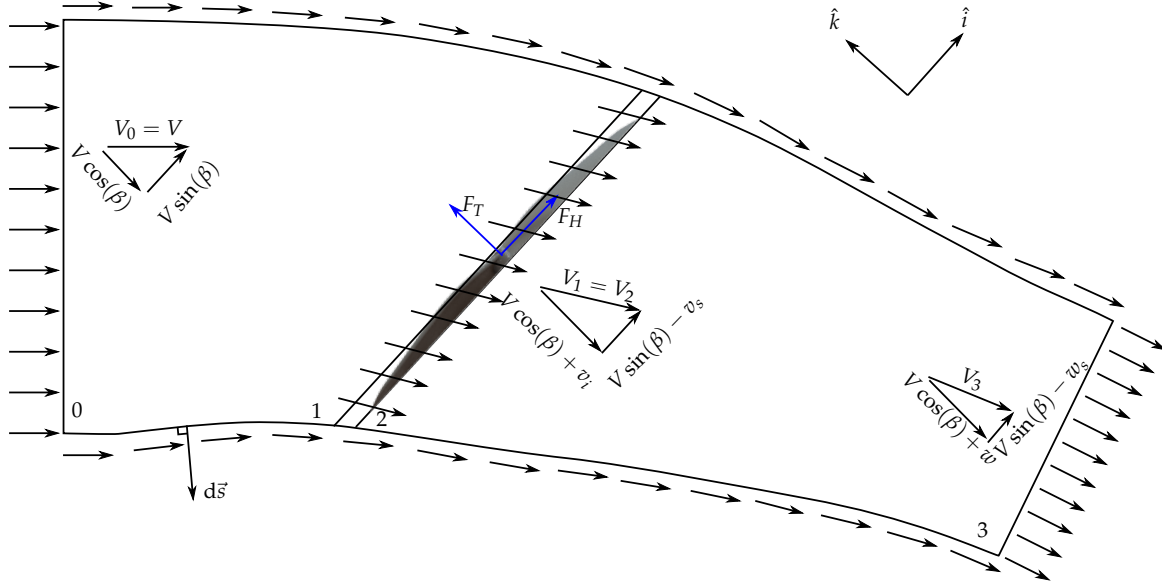


Figure 3. Two-dimensional Eulerian control volume applied to a propeller in forward flight conditions. The vector $d\vec{s}$ represents an infinitesimal surface area of the control volume, whose direction is outwards.

Applying the conservation of momentum on the entire control volume, neglecting gravitational effects on the fluid, and assuming constant static pressure around the entire control volume, we have in the thrust direction \hat{k}

$$F_T^{\text{mt}} = - \iint_S \rho \langle \vec{v}, d\vec{s} \rangle \langle \vec{v}, \hat{k} \rangle \quad (50)$$

$$= - \iint_3 \rho \langle \vec{v}, d\vec{s} \rangle \langle \vec{v}, \hat{k} \rangle - \iint_0 \rho \langle \vec{v}, d\vec{s} \rangle \langle \vec{v}, \hat{k} \rangle \quad (51)$$

$$= \rho A_3 V_3 (w + V \cos(\beta)) + \rho A_0 V (V \cos(\beta)) \quad (52)$$

$$= \dot{m} w \quad (53)$$

and similarly in the drag direction \hat{i}

$$F_H^{\text{mt}} = - \iint_S \rho \langle \vec{v}, d\vec{s} \rangle \langle \vec{v}, \hat{i} \rangle \quad (54)$$

$$= - \iint_3 \rho \langle \vec{v}, d\vec{s} \rangle \langle \vec{v}, \hat{i} \rangle - \iint_0 \rho \langle \vec{v}, d\vec{s} \rangle \langle \vec{v}, \hat{i} \rangle \quad (55)$$

$$= - \rho A_3 V_3 (V \sin(\beta) - w_s) + \rho A_0 V (V \sin(\beta)) \quad (56)$$

$$= \dot{m} w_s \quad (57)$$

Now applying the conservation of energy:

$$F_T^{\text{mt}}(V \cos(\beta) + v_i) - F_H^{\text{mt}}(V \sin(\beta) - v_s) = \iint_S \frac{1}{2} \rho \langle \vec{v}, d\vec{s} \rangle v^2 \quad (58)$$

$$= \iint_3 \frac{1}{2} \rho \langle \vec{v}, d\vec{s} \rangle v^2 + \iint_0 \frac{1}{2} \rho \langle \vec{v}, d\vec{s} \rangle v^2 \quad (59)$$

$$= \frac{1}{2} \rho A_3 V_3^3 - \frac{1}{2} \rho A_0 V^3 \quad (60)$$

$$= \frac{1}{2} \dot{m} (V_3^2 - V^2) \quad (61)$$

$$= \frac{1}{2} \dot{m} (w^2 + w_s^2 + 2V \cos(\beta) w - 2V \sin(\beta) w_s) \quad (62)$$

Combining (53), (57) and (62) yields

$$2(wv_i + w_s v_s) = w^2 + w_s^2 \quad (63)$$

$$\Rightarrow 2v_i \approx w \quad (64)$$

where the approximation results from assuming that $w \gg w_s$ and $v_i \gg v_s$, which is equivalent to assuming that the rotor thrust is much larger than the H-force. From Supplementary Dataset S1 (or Figure 6), this is the case as the thrust is an order of magnitude larger than the H-force, consistent with the observations in [65] (and it is worth mentioning, the H-force is about an order of magnitude larger than the lateral force F_S). Thus,

$$F_T^{\text{mt}} = 2\rho A(v_i + V \cos(\beta))v_i \quad (65)$$

or in the normalized form

$$\frac{F_T^{\text{mt}}}{\frac{1}{2}\rho A(\Omega R)^2} = 4(\lambda_i + \lambda_c)\lambda_i =: C_{FT}^{\text{mt}}(\lambda_c, \lambda_i) \quad (66)$$

Therefore, λ_i can be solved for via the following:

$$\lambda_i(\lambda_c, \mu) = \text{find } \lambda_i \text{ s.t. } C_{FT}(\lambda_c, \mu, \lambda_i) = C_{FT}^{\text{mt}}(\lambda_c, \lambda_i) \quad (67)$$

yielding

$$\lambda_i(\lambda_c, \mu) = \frac{1}{8} \left(-4\lambda_c + c_{l,\alpha}\sigma(\delta - 1) + \left[16\lambda_c^2 + 8c_{l,\alpha}(\delta - 1)\lambda_c\sigma + \right. \right. \quad (68)$$

$$\left. \left. \frac{1}{\delta}(\delta - 1)\sigma \left(-8c_{l,0}\delta(1 + \delta) + c_{l,\alpha} \left(c_{l,\alpha}(\delta - 1)\delta\sigma - 8 \left(2\delta + \mu^2 \right) \theta_{\text{tip}} \right) \right) - 8c_{l,0}\mu^2\sigma \ln(\delta) \right]^{1/2} \right) \quad (69)$$

2.7. Summary

In light of the inflow mapping (68), with abuse of notation we define

$$C_{FT}(\lambda_c, \mu) := C_{FT}(\lambda_c, \mu, \lambda_i(\lambda_c, \mu)) \quad (70)$$

and similarly for the remaining normalized force and torque maps. Furthermore, let x define the parameter vector that parametrizes the above models:

$$x := (c_{l,0}, c_{l,\alpha}, c_{d,0}, c_{d,\alpha}, c_{m,0}, c_{m,\alpha}, \delta, \theta_{\text{tip}}, c_{\text{tip}}) \quad (71)$$

Thus, to make it clear that the maps are actually parametrized by x , a superscript will be used as follows:

$$C_{FT}^x(\lambda_c, \mu) \quad (72)$$

Therefore, the model for (1) can be summarized as follows:

$$(\Omega, V, \beta) \mapsto \begin{bmatrix} F_T \\ F_H \\ M_Q \\ M_R \\ M_P \end{bmatrix} = \begin{bmatrix} C_{FT}^x(\lambda_c, \mu) \frac{1}{2}\rho\pi R^2(\Omega R)^2 \\ C_{FH}^x(\lambda_c, \mu) \frac{1}{2}\rho\pi R^2(\Omega R)^2 \\ C_{MQ}^x(\lambda_c, \mu) \frac{1}{2}\rho\pi R^2(\Omega R)^2 R \\ C_{MR}^x(\lambda_c, \mu) \frac{1}{2}\rho\pi R^2(\Omega R)^2 R \\ C_{MP}^x(\lambda_c, \mu) \frac{1}{2}\rho\pi R^2(\Omega R)^2 R \end{bmatrix}, \quad \begin{aligned} \lambda_c &= \frac{V \cos(\beta)}{\Omega R} \\ \mu &= \frac{V \sin(\beta)}{\Omega R} \end{aligned} \quad (73)$$

2.8. Check if the Assumption ϕ is Small is Violated

Now that the inflow mapping (68) has been solved for, the goal here is to check if we have contradicted our small-angle approximation to simplify the flow angle ϕ from (10) to (11). This will be done by plotting the values of ϕ using (10), which is a function of λ_i for which (68) is used, as a heat map over the rotor disk. This is done for four different combinations of operating conditions in (λ_c, μ) , as done in Figure 4. The largest value of λ_c and μ chosen is 0.2, as $\lambda_c \approx 0.2$ roughly corresponds to when UAV propellers produce zero thrust (see Section 3.2 for examples), an already extreme operating condition. If there are large portions of the rotor disk where the small-angle assumption is violated, then we can necessarily say that our proposed model (73) is invalid.

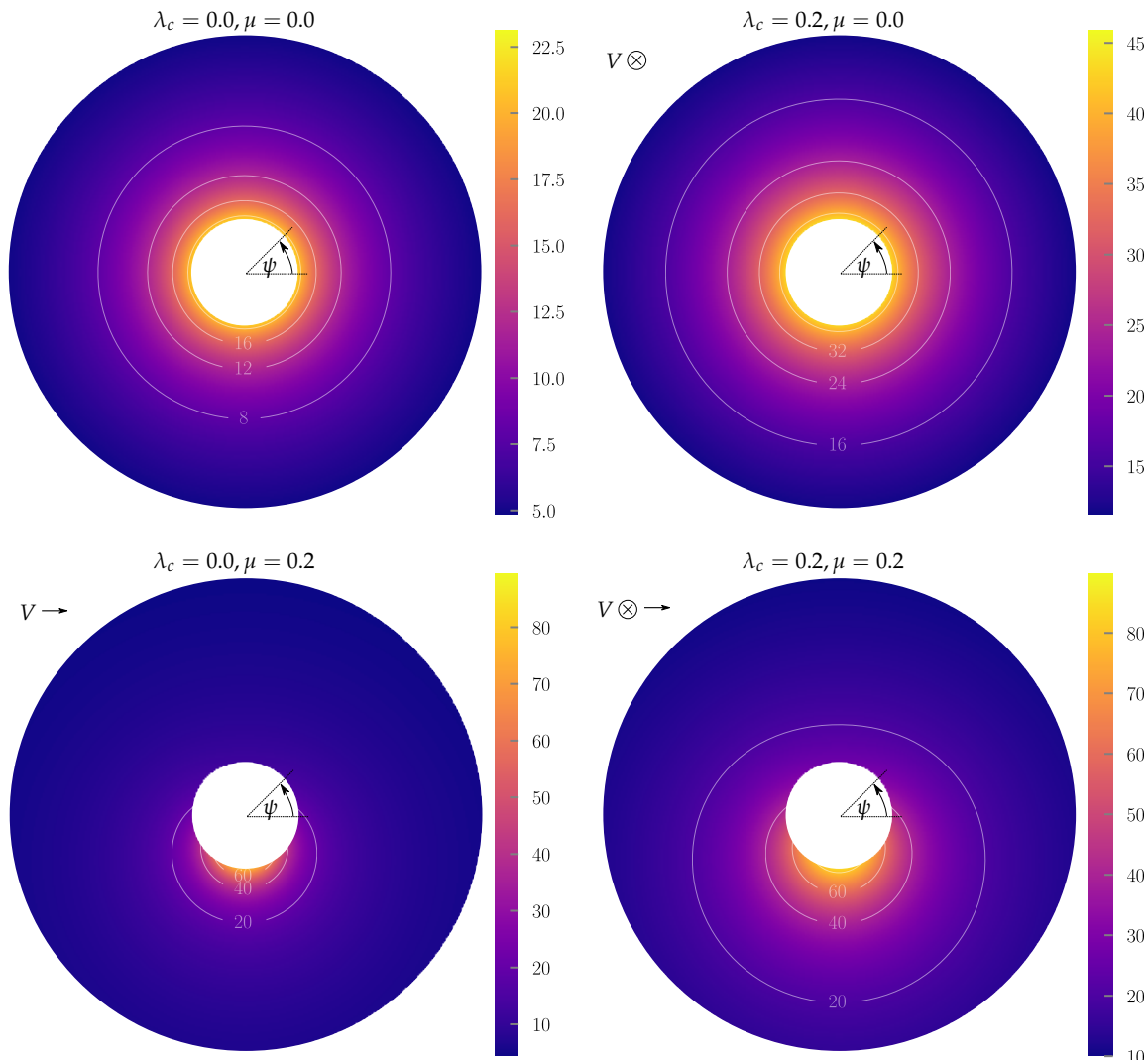


Figure 4. Heat map of the flow angles ϕ (in degrees) over the rotor disk (top view), evaluated using the exact map (10) with λ_i from (68) for four different operating conditions in (λ_c, μ) . For $\lambda_c > 0$, the incoming flow goes into the page, and for $\mu > 0$, the incoming flow comes from the left. The relevant parameter values used are $c_{l,0} = 0.4, c_{l,\alpha} = 3, \delta = 0.2, \sigma = 0.084$, which are typical values for UAV propellers (see Appendix A). The goal is to have an idea of the flow angles, and whether we contradict our small-angle approximation used in (11).

As can be seen in Figure 4, for hover flight ($\lambda_c = 0, \mu = 0$) the angle reaches approximately 22 degrees, which is small enough for the small-angle approximation to hold. In the extreme axial flight scenario ($\lambda_c = 0.2, \mu = 0$), the angle reaches above 40 degrees, which violates the small-angle approximation, but this occurs in a relatively small region of the rotor disk. The same is also true for

the oblique flow scenario ($\mu = 0.2$). Nevertheless, the region in which the violation occurs will become larger as λ_c and μ increases. It is also interesting to note that the angle doesn't reach near 180 [deg], the "reverse flow region" [36], unless μ is (roughly) larger than 0.5. Thus we can conclude that for the operating regions considered, the proposed model (73) is not invalid, but the error of the model can become substantial for larger λ_c and μ .

3. Inferring Parameters from Labelled Data (Supervised Learning)

The goal in this section is two-fold: to determine the parameter vector x for the model (73) using labelled data, and to assess the fidelity of the corresponding model.

3.1. Algorithm

Let any variable with a bar denote a vector of measurements. For example, $\bar{\Omega} \in \mathbb{R}^{N_m}$ is a tuple of N_m measured Ω values, and $\bar{\Omega}_i$ is the i -th measured value. Similarly, the i -th measured force coefficient is given as $\bar{C}_{y,i} := \bar{y}_i / \frac{1}{2}\rho A(\bar{\Omega}_i R)^2$ for $y \in \{F_T, F_H\}$, and for the moment coefficient is given as $\bar{C}_{y,i} := \bar{y}_i / \frac{1}{2}\rho A(\bar{\Omega}_i R)^2 R$ for $y \in \{M_Q, M_R, M_P\}$.

The measured root mean square error for the force/moment coefficient of $y \in \{F_T, F_H, M_Q, M_R, M_P\}$ is

$$RMSE_y(x) := \sqrt{\frac{1}{N_m} \sum_{i=1}^{N_m} \left(C_y^x(\bar{\lambda}_{ci}, \bar{\mu}_i) - \bar{C}_{y,i} \right)^2} \quad (74)$$

Thus the optimization algorithm to infer the parameters x is simply

$$x^* = \arg \min_x \sum_{y \in \{F_T, F_H, M_Q, M_R, M_P\}} RMSE_y(x) \quad (75)$$

This problem is not convex (the model is not linear in the parameters x), and is solved in practice using Python's SciPy package [74] via the Differential Evolution optimization routine from [75] (the settings given to the `scipy.optimize.differential_evolution` routine are: `popsize=200`, `polish=True`, `workers=-1`, `bounds=[(0,1), (1,10), (0,0.5), (0,5), (-10,10), (0,30), (0.1,0.4), (0, numpy.radians(30)), (0.01*R,0.3*R)]`). The bounds were added to limit the search space in order to speed up convergence. The optimization procedure runs for approximately 2 minutes using measurements as outlined in Section 3.2 on a laptop with an Intel i7-6700HQ processor).

To assess the quality of the fit, the standard metrics outlined in [76,77] are used: the coefficient of determination R^2 :

$$R_y^2(x) = 1 - \frac{RMSE_y(x)^2}{\text{SampleVariance}(\bar{C}_y)} \quad (76)$$

and the normalized root-mean-squared-error (nRMSE):

$$nRMSE_y(x) = \frac{RMSE_y(x)}{\max_i \bar{C}_{y,i} - \min_i \bar{C}_{y,i}} \quad (77)$$

3.2. Experimental Assessment

3.2.1. Oblique Flow Results

Two datasets for oblique flows are used. The first contains load measurements at various operating conditions V , Ω and β for 19 propellers collected at the "Large Subsonic Wind Tunnel" at the Institute of Fluid Dynamics at ETH Zurich (see Figure 5 for the experimental set-up). In particular, the tested wind speeds V were set between 0, 6, 18 [m/s]. At each given wind speed, the propeller rotation rate Ω

was set to vary sinusoidally at $1/60 \approx 0.017$ [Hz] between 150 and 600 [rad/s]. Meanwhile, the angle β is varied with a servo motor at a rate of 0.2 [deg/s] between -10 and 90 [deg]. The low bandwidth in these operating conditions is assumed to be sufficiently small for the quasi-steady flow assumption to hold, and the torque resulting from the gyroscopic precession is negligible. Load data was collected at a rate of 1 [kHz], which is then passed through an ideal low pass filter in post-processing with cut-off 0.1 [Hz] to obtain the average loads, and then translated to the centre of the rotor disk (in particular, the moment caused by F_H at the loadcell is removed from the measured pitching moment, to yield M_P). The resulting dataset can be found in Supplementary Dataset S1 (the samples in Supplementary Dataset S1 have been down-sampled to 50 [Hz] to reduce size; some propellers have data for $\beta > 90$ [deg]).

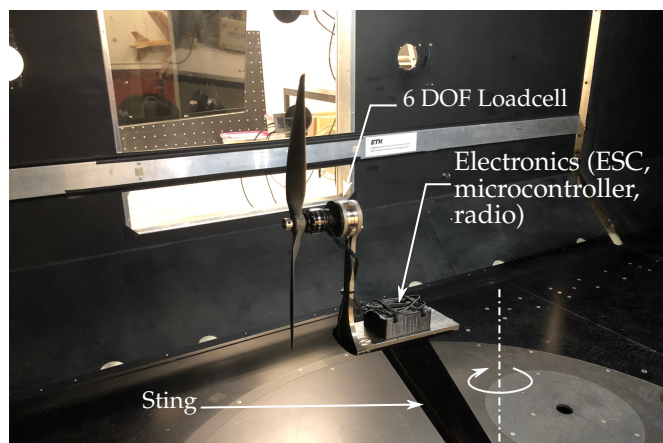


Figure 5. Experimental set-up for oblique flow inside the “Large Subsonic Wind Tunnel” at ETH Zurich. The sting is mounted on a servo motor underneath the tunnel that rotates around the vertical axis to test various β angles. The loads measured at the loadcell are translated to the centre of the propeller. The loadcell used is an ATI Mini40 with the SI-20-1 calibration, and communicates the load data to the host computer via a direct Ethernet connection. The propeller is rotated via a brushless DC motor that is driven by an SN20A electronic speed controller (ESC). The measured rotation rate Ω based on the zero-phase crossings of the motor is computed by an STM32F4 microcontroller, which then communicates the Ω to the host computer via a Laird RM024 radio. Both the wind speed V , which is measured using a pitot tube and pressure sensor, and servo angle β , are sampled via a LabJack U12 data acquisition board and sent to the host PC over a USB connection.

The data points corresponding to $\lambda_c > 0.3$ and $\mu > 0.3$ are thrown away (far too extreme of an operating condition and practically uninteresting), after which the grey-box identification is performed. Figure 6 shows the results for one of the tested propellers, and Figure 7 shows the same but in the dimensionless space. The plots for the rest of the tested propellers can be found in Supplementary Dataset S1. In Figure 6, the standard hover model is also shown for reference, which has clear mismatch for non-zero V .

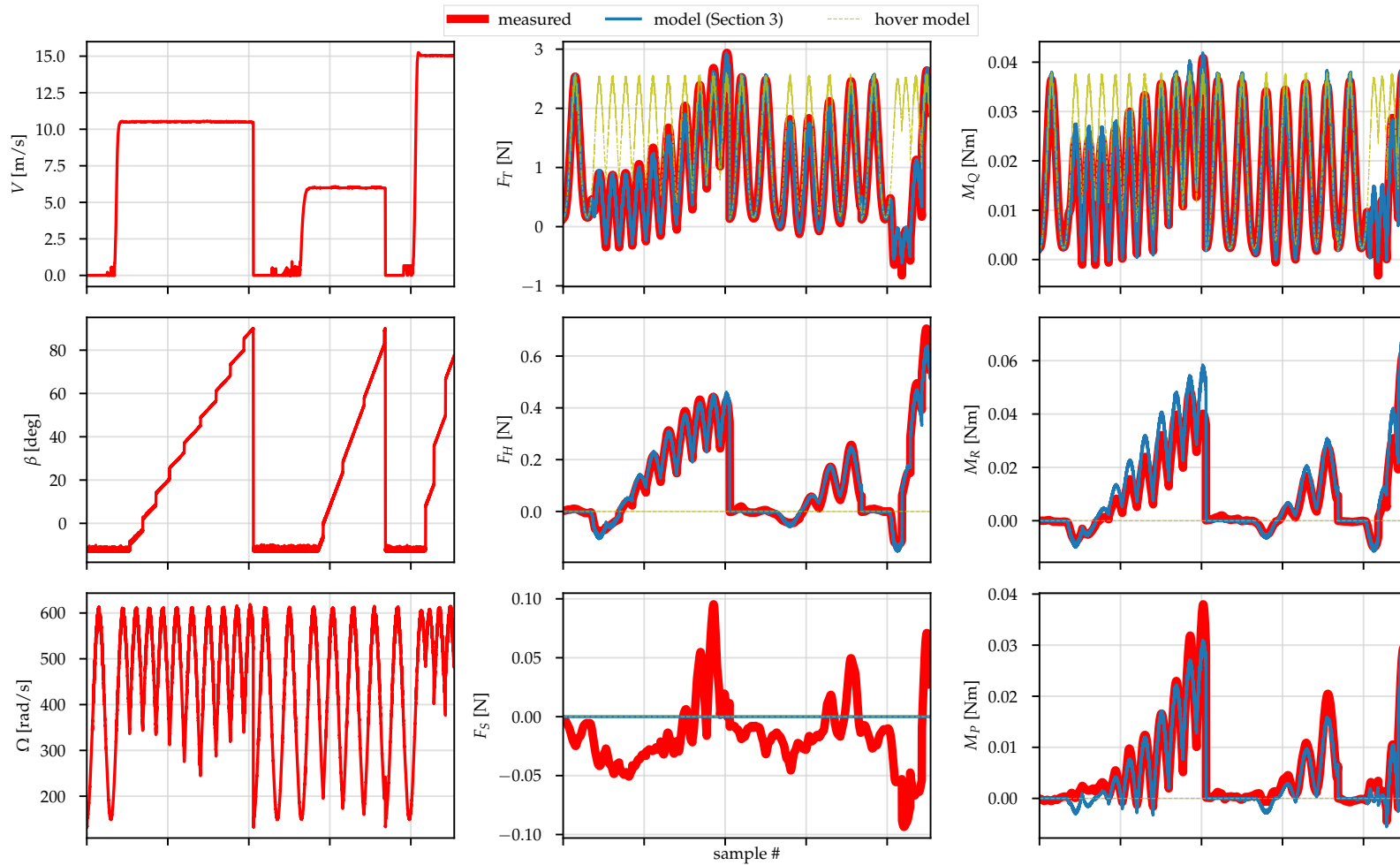


Figure 6. Propeller: mamr-8x4.5. Note that the points corresponding to $\lambda_c < 0$, $\lambda_c > 0.3$ and $\mu > 0.3$ have been omitted, as mentioned in Section 3.2. Note that (1) neglects the side force F_S , so the model is set to output 0 [N]. Model is as per Section 3. The prediction made by the standard hover model is also shown for reference.

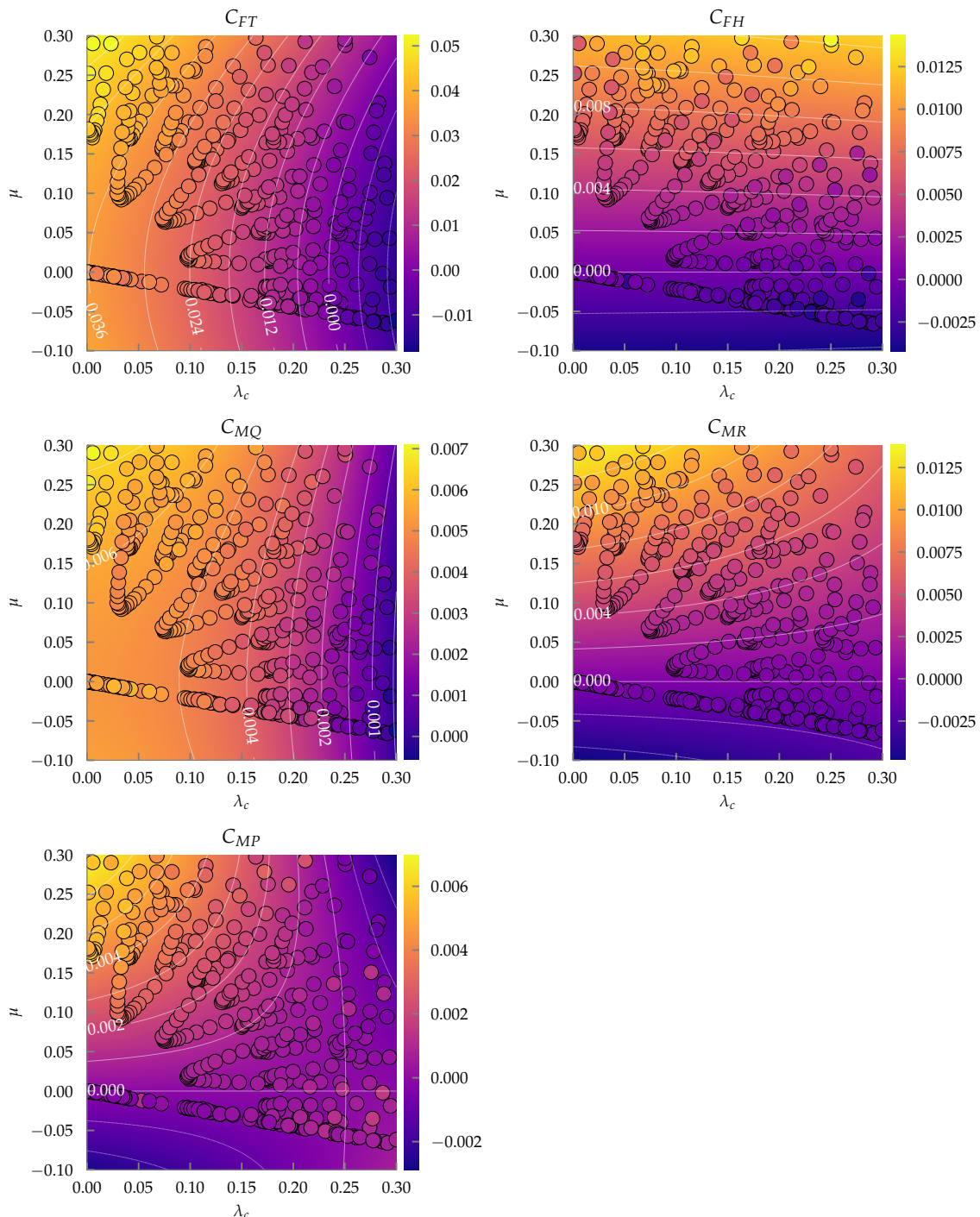


Figure 7. Propeller: mamr-8x4.5, in the dimensionless space. Measured data are shown as circles, and the fitted model as described in Section 3 is depicted as a contour plot with associated labelled contour lines.

The second dataset is provided by the authors of [7], who did a similar data collection of load data but for a single, Graupner electric 9x5 propeller. Figure 8 shows the corresponding plots.

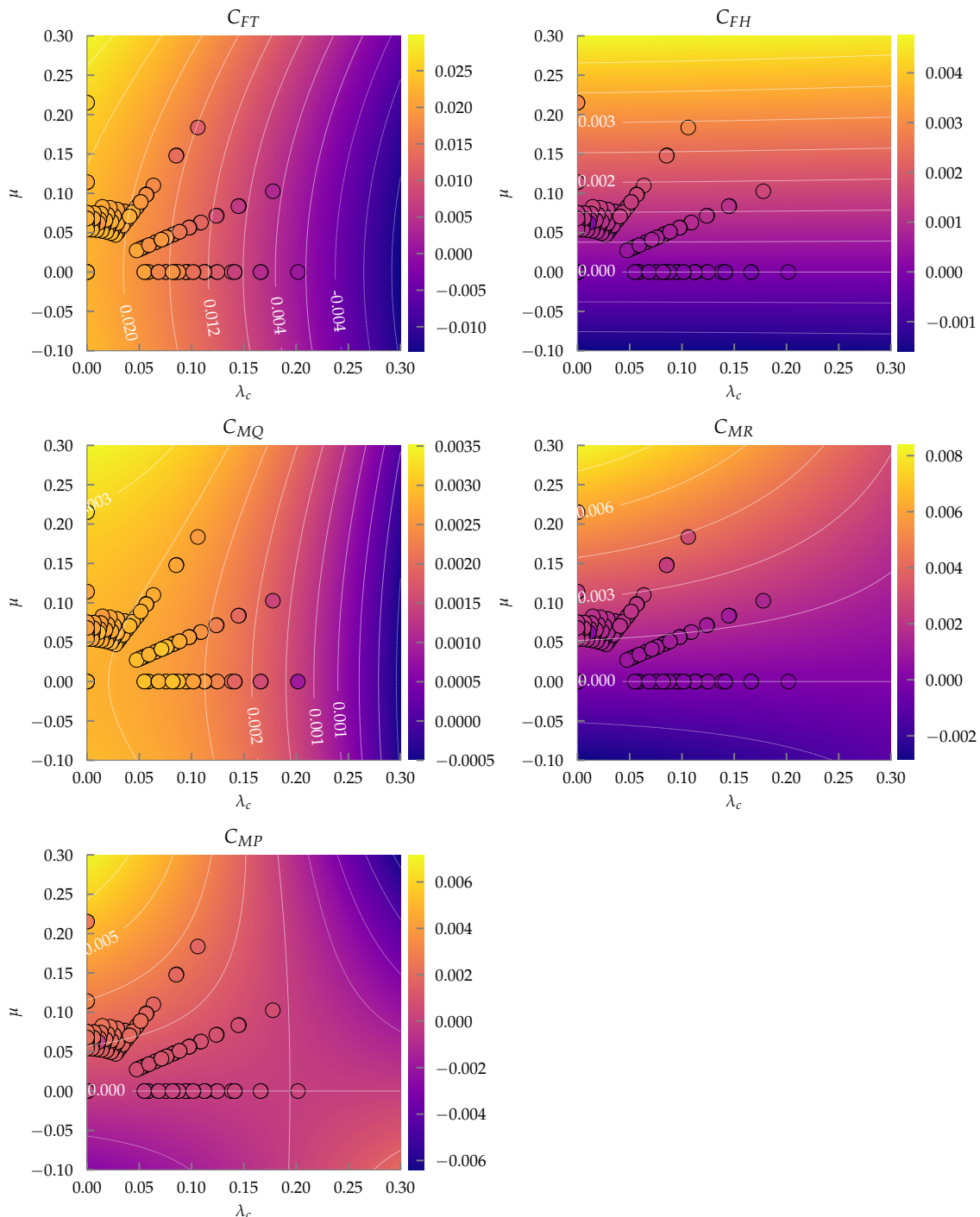


Figure 8. Propeller: gre-9x5, in the dimensionless space. Measured data from [7] are shown as circles, and the fitted model as described in Section 3 is depicted as a contour plot with associated labelled contour lines.

The fitting errors across the two datasets are depicted in Figure 9, and the results along with the optimal parameter values can be found in tabular format in Table A1 in Appendix A. A few observations can be made:

- From the histograms in Figure 9, we can see that the models perform well, especially for the forces F_T , F_H and the rotor torque M_Q which have median R^2 values above 0.93 (an R^2 of 1 corresponds to perfect fit). The rolling and pitching moments have slightly reduced accuracy,

with median R^2 of 0.86 and 0.79, respectively. However, the R^2 metric tends to underestimate the model performance when the data has small values [76], as is the case for the moment coefficients. The $nRMSE$ values found in Appendix A, or the plots in Supplementary Dataset S1, indeed shows that the model performance is still reasonable for the propellers that have poorer R^2 values.

- From the fitted parameter values in Appendix A, we can see that the parameters are in a consistent range of values for both datasets. Occasionally the fitted $c_{l,\alpha}$ value exceeds 2π (the theoretical value for a flat plate [70]), which can be expected for non-symmetric airfoils with positive camber [70]. Furthermore, the pitching moment constants $c_{m,0}, c_{m,\alpha}$, are consistently large in magnitude. From thin airfoil theory, this could again be expected for airfoils with very large positive camber [70]; however, there could be some unmodelled phenomena, possibly due to blade flapping [34], or an artefact of the assumptions made to derive the map (73), and could be a subject for future investigation.

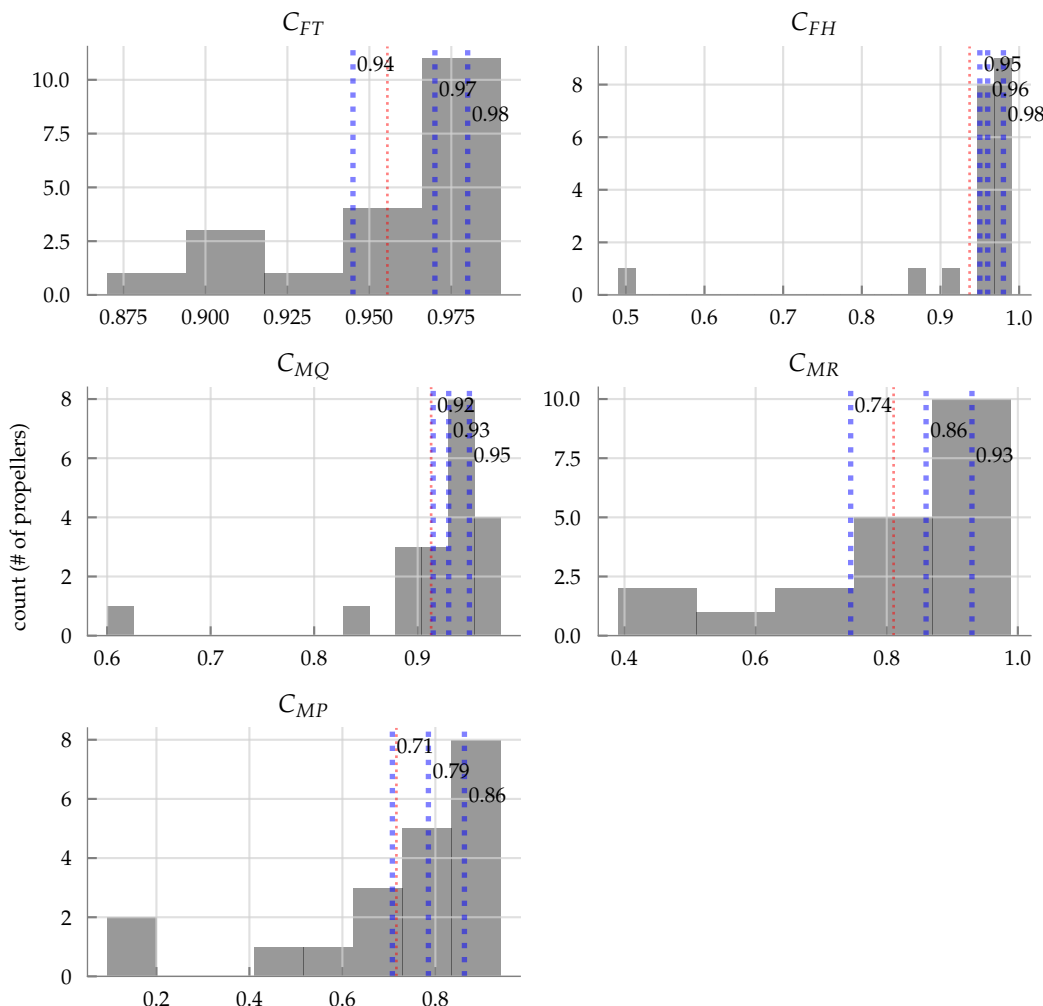


Figure 9. Histogram of R^2 values for each force and moment coefficient using the fitted model as described in Section 3 for all 20 propellers tested under oblique flow. The errors along with the parameter values can be found in tabular format in Table A1 in Appendix A. The blue dotted lines represent the 25, 50, and 75th percentiles and are labelled, and the red dotted line represents the mean.

3.2.2. Axial flow Results

The same fitting procedure is performed against the dataset for axial flow provided by [68], and as such we only consider the thrust and rotor torque. Figure 10 show the plots for four out of the 180 propellers, and the histogram of fitting errors are shown in Figure 11. The parametric models

perform very well, with a median R^2 value of above 0.97, and from Table A2 in Appendix A, there is good consistency with the range of parameter values.

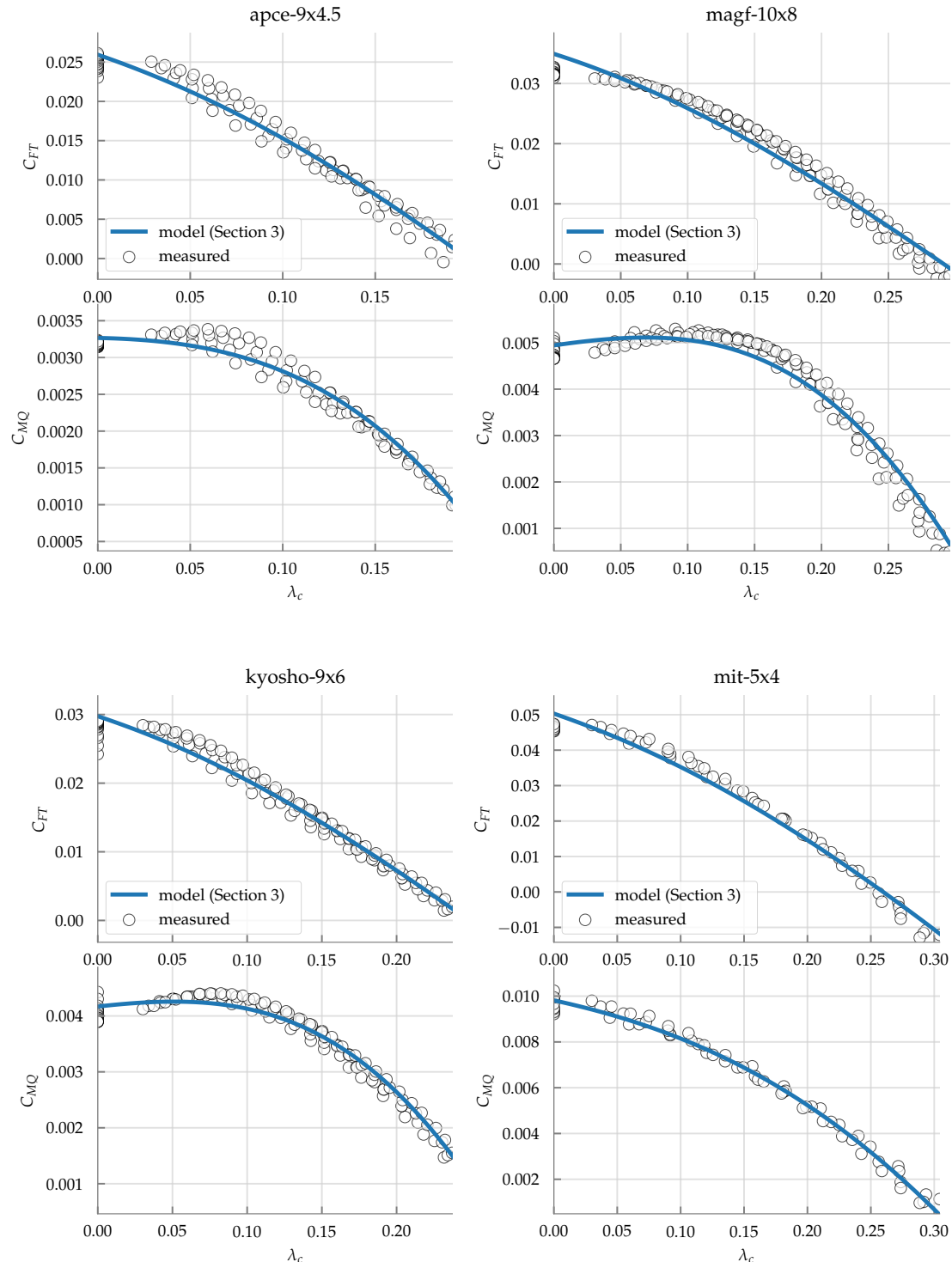


Figure 10. Models as described in Sections 3 tested against measured data provided by [68] for four propellers.

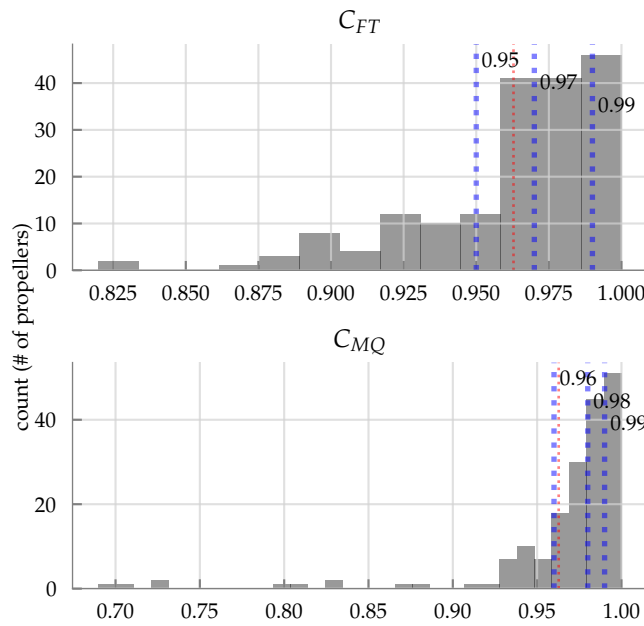


Figure 11. Histogram of R^2 values for each force and moment coefficient using the fitted model as described in Section 3 for the 180 propellers tested under axial flow from the dataset [68]. The errors along with the parameter values can be found in tabular format in Table A2 in Appendix A. The blue dotted lines represent the 25, 50, and 75th percentiles and are labelled, and the red dotted line represents the mean.

4. Inferring Parameters a-priori, without Labelled Data

The goal in this section is to infer the parameters x for the model (73) using only the static load coefficients to construct a prediction for the parameter vector x and to assess the corresponding model's fidelity.

4.1. Parameter Prediction

Start by fixing $c_{d,0} = 0.05$, about the average of the optimal fit values from Tables A1 and A2 in Appendix A, and consistent with typical values in literature for airfoils [59,70]. Similarly, fix $\delta = 0.20$, a typical value as used in [34]. The value c_{tip} is measured directly from the propeller. Some propellers have a sharp taper near the tips and it becomes difficult to define where to measure; we measured at the point just before it starts to taper off, around $r = 0.93$.

Furthermore, assume that the airfoil of the blades is symmetric, and thus as a consequence fix $c_{l,0} = c_{m,0} = c_{m,\alpha} = 0$ (we have no other information to infer these parameters).

The value of θ_{tip} can be inferred: propellers are typically specified as $R \times P$, with R the radius of the propeller (usually in inches), and P is the mean geometric pitch (also usually in inches). The geometric pitch $p(r)$ is defined to be the amount a blade element at $y = Rr$ travels forward over one rotation of the propeller through a solid medium (i.e., without flow slippage) [78,79], and is given by the following geometric relationship (some manufacturers may use their own definition for the pitch, but nevertheless this is used as a starting point):

$$\tan(\theta(r)) = \frac{p(r)}{2\pi Rr} \quad (78)$$

Thus the mean geometric pitch P is given by

$$P = \int_0^1 2\pi Rr \tan(\theta(r)) dr \quad (79)$$

Using our definition of $\theta(r)$ from (22),

$$P = 2\pi R \int_{\delta}^1 r \tan\left(\frac{\theta_{\text{tip}}}{r}\right) dr \quad (80)$$

$$\approx 2\pi R \int_{\delta}^1 \theta_{\text{tip}} dr \quad (81)$$

$$\Rightarrow \theta_{\text{tip}} = \frac{P}{2\pi R(1-\delta)} = 1.25 \frac{P}{2\pi R} \quad (82)$$

It is interesting to note that the models are very sensitive to the θ_{tip} value, and using even a slightly adjusted value to the one proposed in (82) can result in grossly inaccurate models.

Next assume that the static thrust and torque coefficients have been measured, using a procedure as in e.g., [80], i.e., by fitting the standard quadratic model with coefficients α_T , α_Q at hover such that

$$F_T(\Omega, V = 0, \beta = \times) = \alpha_T \Omega^2 \quad (83)$$

$$M_Q(\Omega, V = 0, \beta = \times) = \alpha_Q \Omega^2 \quad (84)$$

The equivalent coefficients in normalized units are given by

$$C_{FT}^{\text{static}} := \frac{\alpha_T}{\frac{1}{2}\rho\pi R^4} \quad (85)$$

$$C_{MQ}^{\text{static}} := \frac{\alpha_Q}{\frac{1}{2}\rho\pi R^5} \quad (86)$$

The remaining coefficients to be determined are $c_{l,\alpha}$ and $c_{d,\alpha}$. These can be determined by using the static coefficients from (85) and (86) in a root finding routine as follows:

$$c_{l,\alpha} = \text{find } x_1 \text{ s.t. } C_{FT}^x(0, 0) = C_{FT}^{\text{static}} \quad (87)$$

$$c_{d,\alpha} = \text{find } x_3 \text{ s.t. } C_{MQ}^x(0, 0) = C_{MQ}^{\text{static}} \quad (88)$$

where x_i denotes the i -th element of the parameter vector x . Note that (87) must be performed before (88), since the rotor torque map depends on the parameter $c_{l,\alpha}$. If a root cannot be found, then the above can be converted to a least squares optimization problem.

4.2. Experimental Assessment

4.2.1. Oblique Flow Results

The approach is tested against the two oblique flow datasets as described in Section 3.2; as before, the models can be viewed for one of the propellers in Figures 12 and 13 (the plots for the remaining tested propellers are available in Supplementary Dataset S1), and the histogram of errors across all propellers can be found in Figure 14. A couple of observations can be made:

- The thrust, H-force, and rolling moments have (surprisingly) high accuracy, with median R^2 values above 0.88.
- The rotor torque (median R^2 of 0.61) has reduced accuracy for few of the propellers, such as the apcsf, most likely due to severity in the mismatch of the assumed chord model (23). However, typically most of the error for the rotor torque comes at the high λ_c, μ ratios, as seen in Figures 12 and 13: in Figure 12, the mismatch in torque occurs when the rotor is producing negative thrust, that is λ_c near 0.3 in Figure 13. Thus for small enough operating conditions in λ_c, μ , this approach may prove feasible for predicting the rotor torque as well. The pitching moments also have reduced accuracy (median R^2 of -0.35), as expected as assuming symmetric airfoils results in the predicted pitching moments to be identically equal to zero, which evidently is not the case.

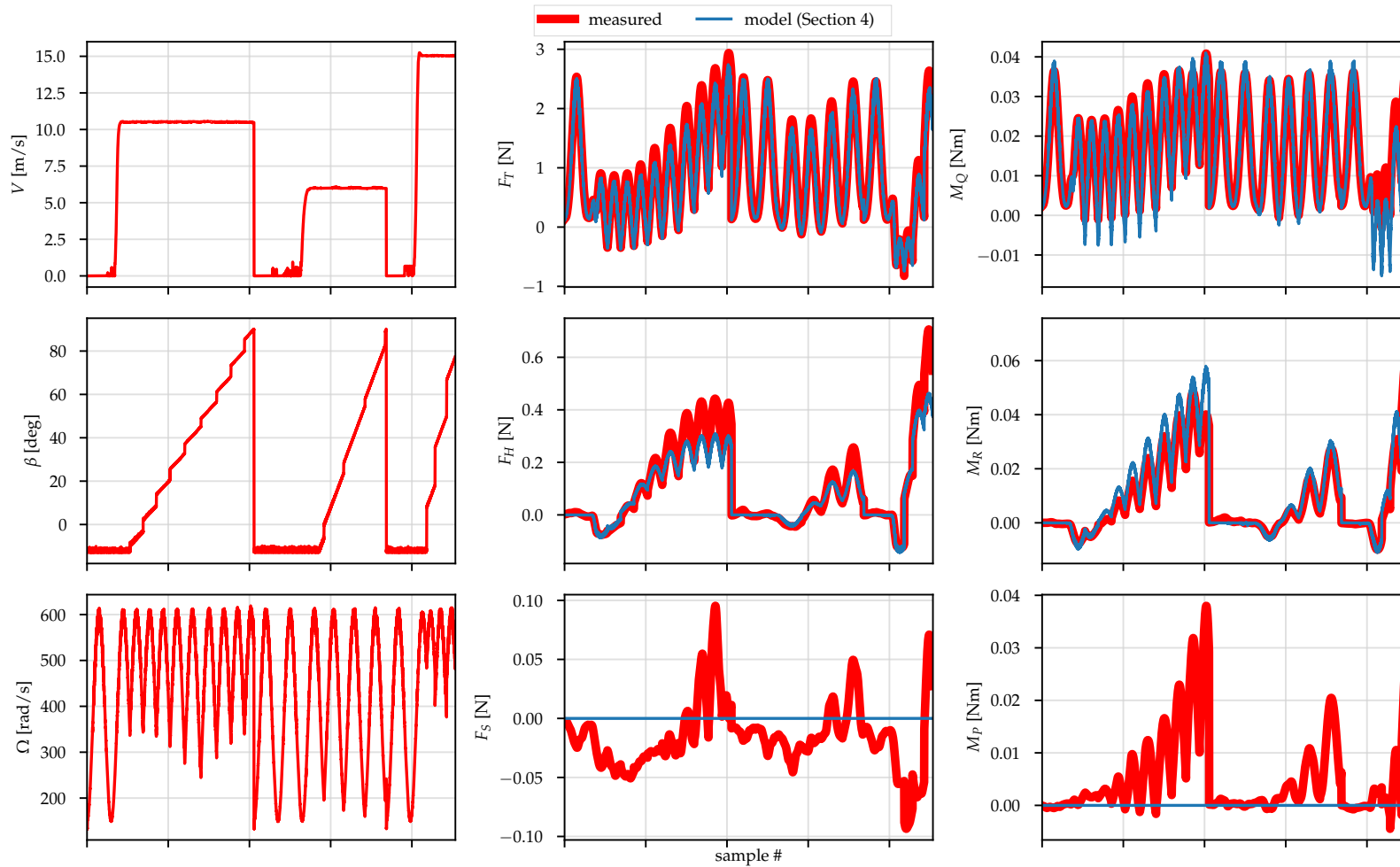


Figure 12. Propeller: mamr-8x4.5. Note that the points corresponding to $\lambda_c < 0$, $\lambda_c > 0.3$ and $\mu > 0.3$ have been thrown away, as mentioned in Section 3.2. Note that (1) neglects the side force F_S , so the model is set to output 0 [N]. Model is as per Section 4.

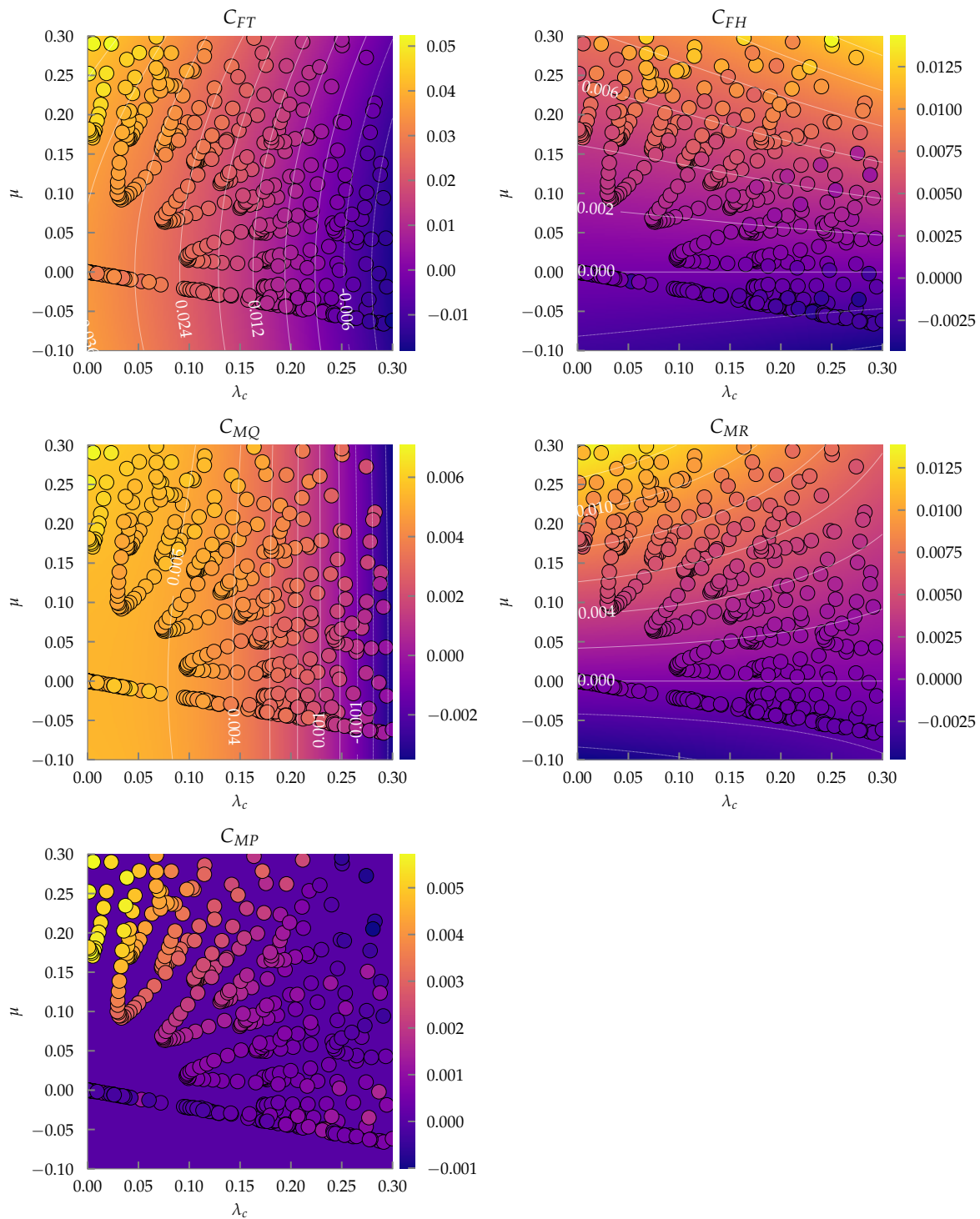


Figure 13. Propeller: mamp-8x4.5, in the dimensionless space. Measured data are shown as circles, and the model as described in Section 4 is depicted as a contour plot with associated labelled contour lines.

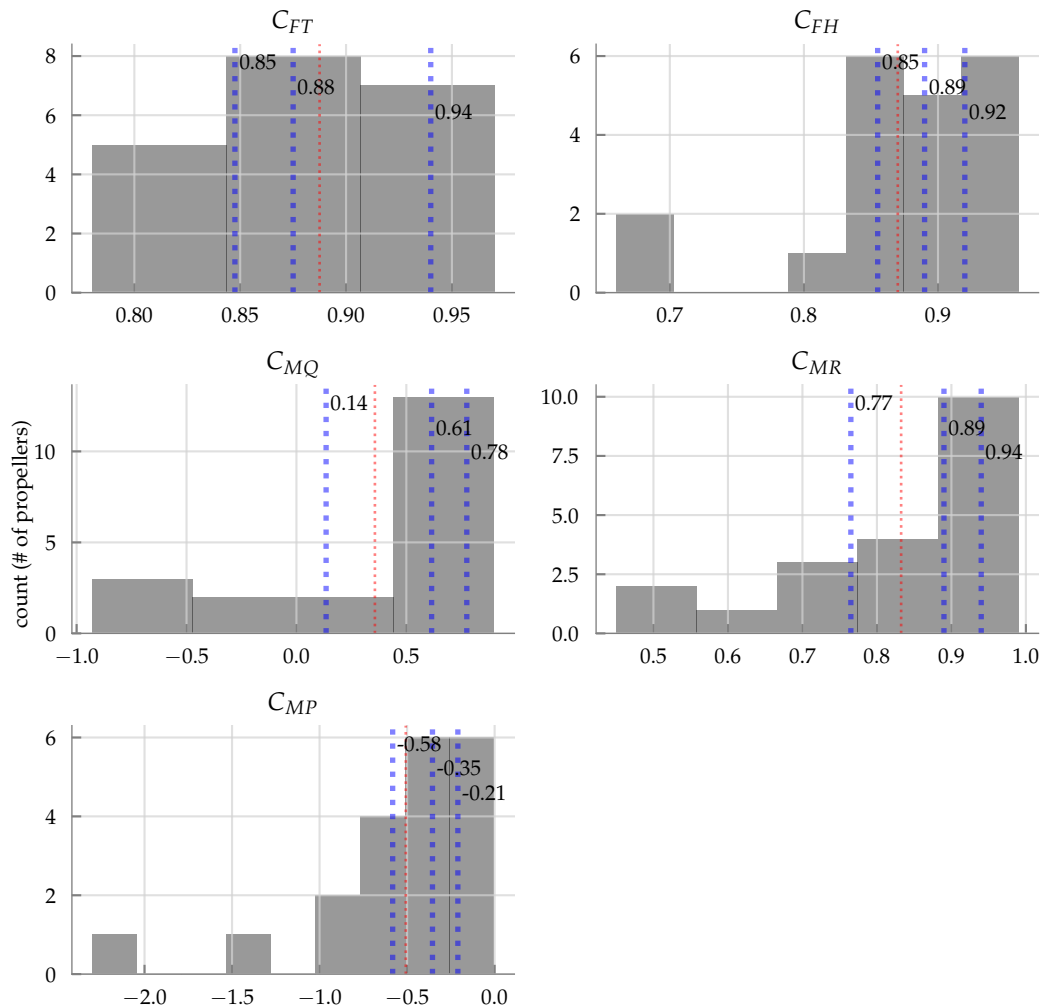


Figure 14. Histogram of R^2 values for each force and moment coefficient using the predicted model as described in Section 4 for all 20 propellers tested under oblique flow. The errors along with the parameter values can be found in tabular format in Table A3 in Appendix A. The blue dotted lines represent the 25, 50, and 75th percentiles and are labelled, and the red dotted line represents the mean.

4.2.2. Axial Flow Results

The same approach was tested against the database provided in [68] (not all propellers could be tested, since the chord measurements were not provided for all propellers). The histogram of the errors using the R^2 metric are shown in Figure 15.

Again, the results are surprisingly good (median R^2 for thrust is 0.90, and for the torque is 0.75). The propellers that do have issues are the APC slowfly propellers, as was the case for the oblique flow, as well as for some of the smaller propellers with diameter less than five inches (e.g., the small gwsdd and the mi propellers). This again can be attributed to the mismatch between the assumed chord model (23), as these small propeller blades usually have a constant chord model. This could be a subject for further investigation.

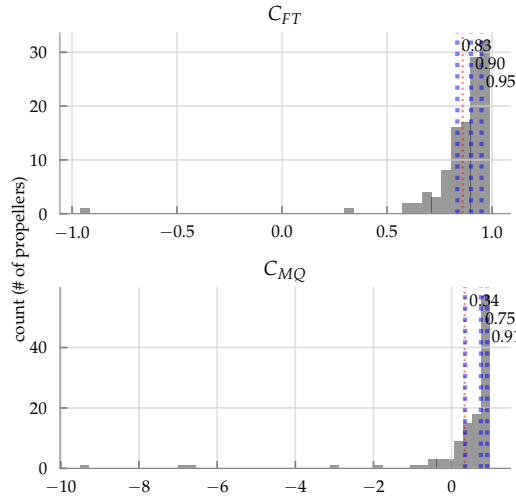


Figure 15. Histogram of R^2 values for each force and moment coefficient using the predicted model as described in Section 4 for 115 propellers tested under axial flow from the dataset [68]. The errors along with the parameter values can be found in tabular format in Table A4 in Appendix A. The blue dotted lines represent the 25, 50, and 75th percentiles and are labelled, and the red dotted line represents the mean.

5. Second-Order Lumped Parameter Models

The goal in this section is to simplify the models of the load coefficients (73) even further using a second-order Taylor series expansion. This yields a lower-order, and yet even more computationally inexpensive model for the propeller loads, as the models become multinomials.

5.1. Models

First consider the thrust coefficient, $C_{FT}(\lambda_c, \mu)$. The second-order Taylor expansion around $(\lambda_c = 0, \mu = 0)$ yields:

$$C_{FT}(\lambda_c, \mu) \approx C_{FT}^{2nd}(\lambda_c, \mu) := \underbrace{C_{FT}^x(0, 0)}_{=C_{FT}^{\text{static}}} + \begin{bmatrix} \frac{\partial C_{FT}^x}{\partial \lambda_c} & \frac{\partial C_{FT}^x}{\partial \mu} \end{bmatrix} \begin{bmatrix} \lambda_c \\ \mu \end{bmatrix} + \frac{1}{2} \begin{bmatrix} \lambda_c & \mu \end{bmatrix} \begin{bmatrix} \frac{\partial^2 C_{FT}^x}{\partial \lambda_c^2} & \frac{\partial^2 C_{FT}^x}{\partial \lambda_c \partial \mu} \\ \frac{\partial^2 C_{FT}^x}{\partial \lambda_c \partial \mu} & \frac{\partial^2 C_{FT}^x}{\partial \mu^2} \end{bmatrix} \begin{bmatrix} \lambda_c \\ \mu \end{bmatrix} \quad (89)$$

where the partial derivatives in (89) are evaluated at $(\lambda_c = 0, \mu = 0)$.

It can be shown that

$$\left. \frac{\partial C_{FT}^x}{\partial \lambda_c} \right|_{\lambda_c=0, \mu=0} = \frac{1}{8} c_{l,\alpha} (\delta - 1) \sigma \left(4 + \frac{4 c_{l,\alpha} (\delta - 1) \sigma}{\sqrt{(\delta - 1) \sigma (-8 c_{l,0} (1 + \delta) + c_{l,\alpha} (c_{l,\alpha} (\delta - 1) \sigma - 16 \theta_{\text{tip}}))}} \right) \quad (90)$$

$$\left. \frac{\partial C_{FT}^x}{\partial \mu} \right|_{\lambda_c=0, \mu=0} = 0 \quad (91)$$

$$\left. \frac{\partial^2 C_{FT}^x}{\partial \lambda_c^2} \right|_{\lambda_c=0, \mu=0} = -\frac{16 c_{l,\alpha} (\delta - 1)^2 \sigma^2 (c_{l,0} + c_{l,0} \delta + 2 c_{l,\alpha} \theta_{\text{tip}})}{((\delta - 1) \sigma (-8 c_{l,0} (1 + \delta) + c_{l,\alpha} (c_{l,\alpha} (\delta - 1) \sigma - 16 \theta_{\text{tip}})))^{3/2}} \quad (92)$$

$$\left. \frac{\partial^2 C_{FT}^x}{\partial \lambda_c \partial \mu} \right|_{\lambda_c=0, \mu=0} = 0 \quad (93)$$

$$\left. \frac{\partial^2 C_{FT}^x}{\partial \mu^2} \right|_{\lambda_c=0, \mu=0} = -c_{l,0} \sigma \ln(\delta) - \frac{c_{l,\alpha} (\delta - 1) \sigma \left(\theta_{\text{tip}} + \frac{\sigma (c_{l,\alpha} (\delta - 1) \theta_{\text{tip}} + c_{l,0} \delta \ln(\delta))}{\sqrt{(\delta - 1) \sigma (-8 c_{l,0} (1 + \delta) + c_{l,\alpha} (c_{l,\alpha} (\delta - 1) \sigma - 16 \theta_{\text{tip}}))}} \right)}{\delta} \quad (94)$$

Thus,

$$C_{FT}^{2\text{nd}}(\lambda_c, \mu) = C_{FT}^{\text{static}} + k_1\lambda_c + k_2\mu^2 + k_3\lambda_c^2 \quad (95)$$

where

$$k_1 := \left. \frac{\partial C_{FT}^x}{\partial \mu} \right|_{\lambda_c=0, \mu=0} \quad (96)$$

$$k_2 := \left. \frac{1}{2} \frac{\partial^2 C_{FT}^x}{\partial \mu^2} \right|_{\lambda_c=0, \mu=0} \quad (97)$$

$$k_3 := \left. \frac{1}{2} \frac{\partial^2 C_{FT}^x}{\partial \mu^2} \right|_{\lambda_c=0, \mu=0} \quad (98)$$

However, one can view the k_i 's as lumped parameters over which a parameter fitting procedure can be carried out (or evaluated using the parameter generation given the static coefficients as explained in Section 4), similar to the approach outlined in Section 3. This will be done in practice in Section 5.2, and since the second-order model is linear in the new parameters k_i , the fitting problem becomes convex and CVXPY [81,82] is used to yield the optimal parameter vector k^* .

Performing the same second-order Taylor series expansion on the remaining coefficients yield

$$C_{FH}^{2\text{nd}}(\lambda_c, \mu) = k_4\mu + k_5\lambda_c\mu \quad (99)$$

$$C_{MQ}^{2\text{nd}}(\lambda_c, \mu) = C_{MQ}^{\text{static}} + k_6\lambda_c + k_7\mu^2 + k_8\lambda_c^2 \quad (100)$$

$$C_{MR}^{2\text{nd}}(\lambda_c, \mu) = k_9\mu + k_{10}\lambda_c\mu \quad (101)$$

$$C_{MP}^{2\text{nd}}(\lambda_c, \mu) = k_{11}\mu + k_{12}\lambda_c\mu \quad (102)$$

where the corresponding partial derivatives are evaluated in Appendix B. Note that the model now contains 14 total parameters to identify (including the hover thrust and torque coefficients). Note that a black-box second-order multinomial for (1) would contain $5(1 + 3 + 6) = 50$ parameters.

5.2. Experimental Assessment

5.2.1. Oblique Flow Results

The models can be viewed for one of the propellers in Figures 16 and 17 (the plots for the remaining tested propellers are available in Supplementary Dataset S1), and Figure 18 shows the errors for the oblique flow datasets. A few observations can be made:

- The models for thrust, H-force, rotor torque, and rolling moments all perform very well, even over the entirety of the tested domain ($\lambda_c \leq 0.3$, $\mu \leq 0.3$), with median R^2 values above 0.91. However, the model for the pitching moment does not, which implies that the domain over which the second-order Taylor expansion for the pitching moment is valid is far smaller than the rest of the models, as can be seen in Figure 17.
- From the parameter values in Table A5 in Appendix A, the parameters $k_5 \approx 0$ and $k_{10} \approx 0$, so these may potentially be ignored in a practical implementation.

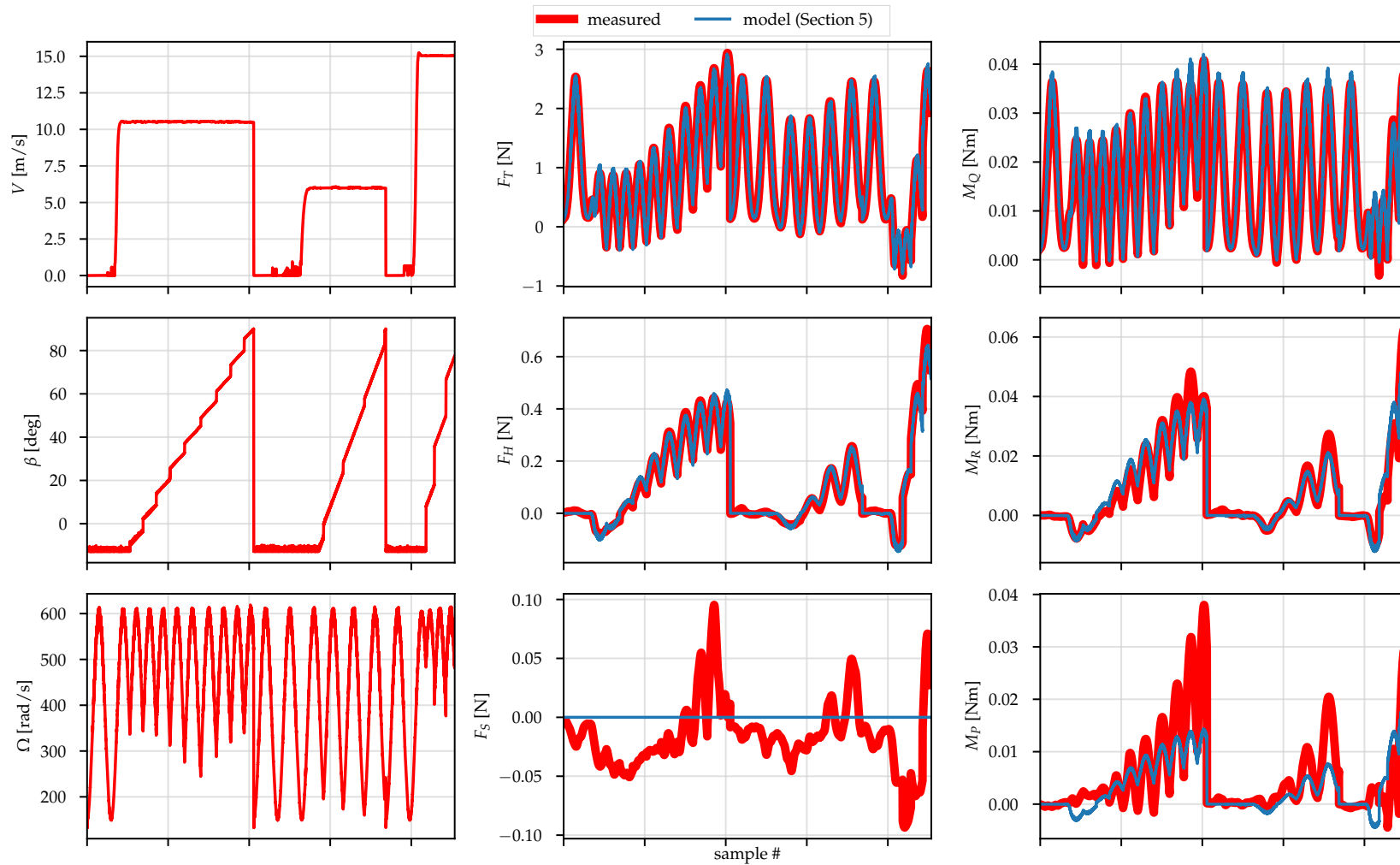


Figure 16. Propeller: mamr-8x4.5. Note that the points corresponding to $\lambda_c < 0$, $\lambda_c > 0.3$ and $\mu > 0.3$ have been thrown away, as mentioned in Section 3.2. Note that (1) neglects the side force F_S , so the model is set to output 0 [N]. Model is as per Section 5.

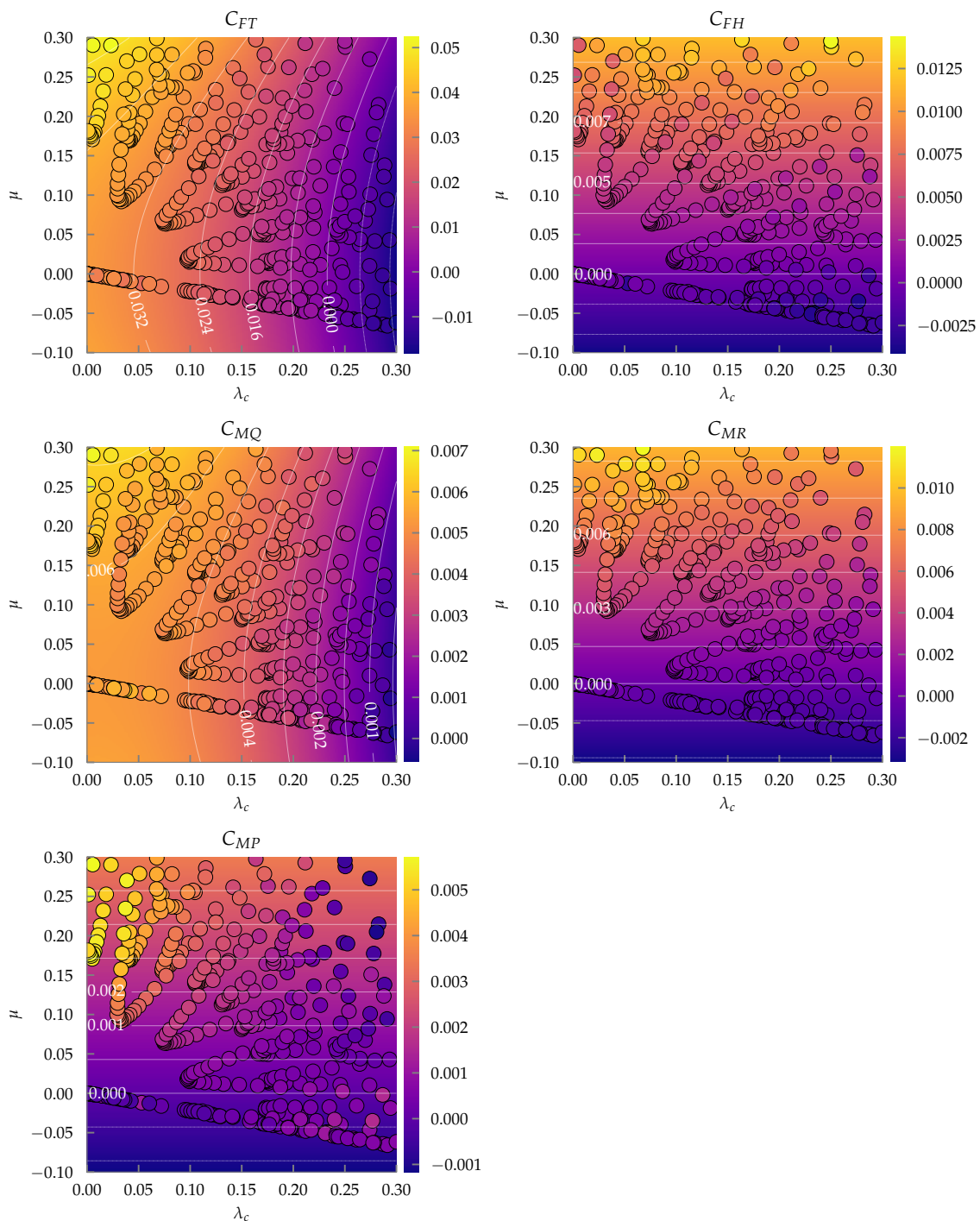


Figure 17. Propeller: mamr-8x4.5, in the dimensionless space. Measured data are shown as circles, and the fitted model as described in Section 5 is depicted as a contour plot with associated labelled contour lines.

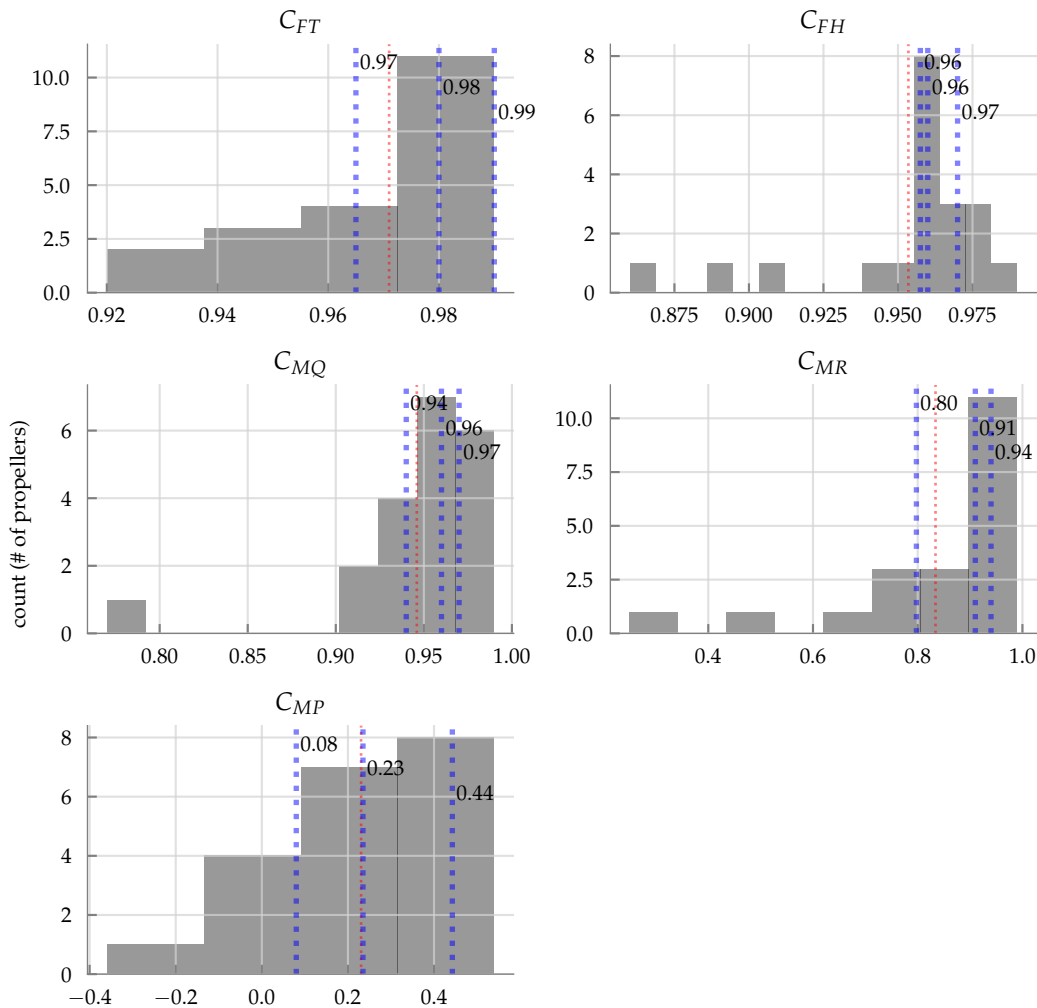


Figure 18. Histogram of R^2 values for each force and moment coefficient using the fitted model as described in Section 5 for all 20 propellers tested under oblique flow. The errors along with the parameter values can be found in tabular format in Table A5 in Appendix A. The blue dotted lines represent the 25, 50, and 75th percentiles and are labelled, and the red dotted line represents the mean.

5.2.2. Axial Flow Results

Figure 19 shows the errors for the axial flow dataset [68]. The model fitting is near perfect in this case.

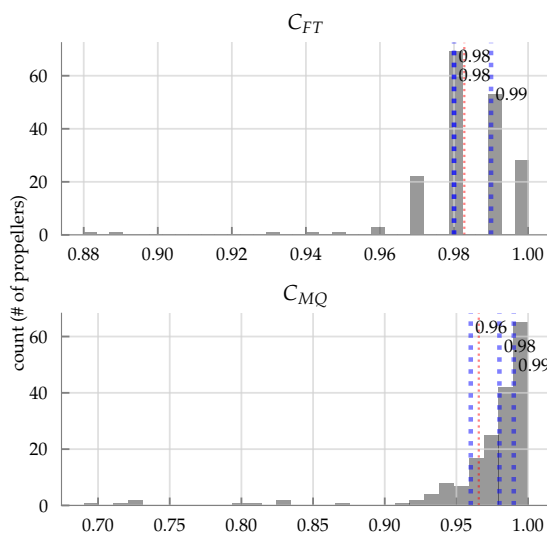


Figure 19. Histogram of R^2 values for each force and moment coefficient using the fitted model as described in Section 5 for the 180 propellers tested under axial flow from the dataset [68]. The errors along with the parameter values can be found in tabular format in Table A6 in Appendix A. The blue dotted lines represent the 25, 50, and 75th percentiles and are labelled, and the red dotted line represents the mean.

6. Conclusion and Future Work

Two analytical, parametric models have been developed for (1), with various parameter generation methods corresponding to Sections 2–5. An oblique flow dataset has also been collected for 19 UAV propellers. Because of the analytical nature, the models are simple to implement and fast to compute, suitable for real-time applications.

The accuracy of the first model is very high for all loads when trained using labelled data in a grey-box identification approach, as shown in Section 3. When no labelled data is available, and the parameter values already determined in Table A1 in Appendix A cannot be used, then one could elect to use the method outlined in Section 4 which only relies on the static thrust and torque coefficients, thereby providing good prediction of the loads in the full forward flight regime. The second-order Taylor series model of Section 5 also results in very accurate models, except for the pitching moment.

A simpler model for the pitching moment could be a suitable direction for future work. Another direction could be to look at micro UAV propellers specifically, which typically use a constant chord model, and to apply the methodology of Section 4 to see if the accuracy of the predicted model can be improved. Further directions in modelling include looking into the windmill-brake operating regime [34] ($\lambda_c < 0$). Another direction is to utilize the proposed models herein for real-time estimation, control, and simulation purposes.

Supplementary Materials: The following are available online at <http://www.mdpi.com/2504-446X/3/4/77/s1>, Dataset S1: Wind tunnel measurements of 19 propellers in oblique flow along with the plots of the proposed models.

Author Contributions: Conceptualization, R.G. and R.D.; methodology, R.G.; software, R.G.; validation, R.G.; formal analysis, R.G.; investigation, R.G.; resources, R.G. and R.D.; data curation, R.G.; writing—original draft preparation, R.G.; writing—review and editing, R.G. and R.D.; visualization, R.G.; supervision, R.D.; project administration, R.G. and R.D.; funding acquisition, R.G. and R.D.

Funding: This research was funded by the Swiss National Science Foundation (SNSF) grant number 200021_162365 and by the Natural Sciences and Engineering Research Council of Canada (NSERC) CGS-D scholarship.

Acknowledgments: The authors would like to thank Julian Humml, Andreas Mueller and Thomas Roesgen at the Institute of Fluid Dynamics (IFD), ETH Zurich, for access to the “Large Subsonic Wind Tunnel”.

Conflicts of Interest: The authors declare no conflict of interest.

Appendix A. Tables of Experimental Results

Table A1. Results of the model fitting as described in Section 3 for all propellers tested under oblique flow. Dimensioned units are in SI units (i.e., θ_{tip} is in radians, and c_{tip} is in meters). Data for gre-9x5 is provided by [7].

Name	x^*								R^2					$nRMSE$					
	$c_{I,0}$	$c_{I,\alpha}$	$c_{d,0}$	$c_{d,\alpha}$	$c_{m,0}$	$c_{m,\alpha}$	δ	θ_{tip}	c_{tip}	C_{FT}	C_{FH}	C_{MQ}	C_{MR}	C_{MP}	C_{FT}	C_{FH}	C_{MQ}	C_{MR}	C_{MP}
ance-12x6	0.72	6.5	0.053	3.3	-2.8	18	0.15	0.17	8.4e-3	0.99	0.91	0.97	0.91	0.85	0.033	0.056	0.050	0.077	0.072
ance-9x5	0.86	6.4	0.078	3.4	-1.9	13	0.12	0.16	6.5e-3	0.98	0.96	0.93	0.92	0.86	0.026	0.038	0.044	0.063	0.074
apce-10x7	0.75	6.6	0.12	2.8	-2.4	12	0.12	0.21	5.7e-3	0.95	0.99	0.92	0.98	0.71	0.038	0.024	0.032	0.034	0.12
apce-12x6	0.92	8.3	0.082	4.8	-2.5	24	0.10	0.14	5.7e-3	0.99	0.99	0.96	0.90	0.84	0.030	0.023	0.043	0.066	0.080
apce-6x4	0.27	8.2	0.14	2.7	-9.8	15	0.10	0.27	2.4e-3	0.93	0.98	0.93	0.91	0.11	0.039	0.029	0.038	0.068	0.14
apce-8x6	0.79	8.3	0.16	3.5	-7.8	22	0.12	0.23	4.0e-3	0.97	0.97	0.93	0.96	0.44	0.038	0.038	0.045	0.048	0.11
apce-8x8	0.26	10	0.16	4.3	7.2	3.2	0.16	0.39	2.4e-3	0.91	0.97	0.89	0.99	0.094	0.055	0.035	0.055	0.028	0.18
apcsf-10x4.7	0.94	6.2	0.055	3.9	-0.97	18	0.13	0.13	9.7e-3	0.97	0.95	0.94	0.70	0.92	0.030	0.044	0.031	0.11	0.063
apcsf-8x3.5	0.96	7.0	0.058	4.4	-1.2	16	0.10	0.13	6.6e-3	0.99	0.96	0.96	0.82	0.88	0.022	0.042	0.036	0.083	0.080
ef4b-10x6	0.75	6.3	0.065	4.3	-1.4	26	0.12	0.13	6.8e-3	0.97	0.98	0.92	0.42	0.94	0.036	0.034	0.056	0.18	0.050
grc-10x4	0.45	6.7	0.051	5.0	-2.4	27	0.17	0.097	7.1e-3	0.98	0.49	0.94	0.39	0.77	0.038	0.12	0.057	0.11	0.079
hqp-7x4.5	0.91	7.2	0.17	3.0	-5.9	22	0.12	0.17	4.6e-3	0.97	0.98	0.84	0.97	0.80	0.037	0.036	0.064	0.041	0.074
hqp-8x4.5	0.87	6.3	0.13	4.5	-0.30	8.3	0.14	0.16	5.9e-3	0.95	0.95	0.92	0.96	0.60	0.045	0.057	0.041	0.048	0.16
ma3b-10x5	0.12	5.8	0.079	3.8	-6.4	28	0.20	0.15	7.0e-3	0.96	0.88	0.95	0.54	0.83	0.052	0.074	0.057	0.15	0.061
ma3b-8x6	0.052	4.2	0.080	2.0	-9.8	25	0.21	0.24	6.5e-3	0.91	0.96	0.93	0.73	0.72	0.065	0.045	0.047	0.14	0.077
mae-12x6	0.84	7.7	0.17	4.8	-5.3	22	0.17	0.14	6.8e-3	0.95	0.96	0.90	0.75	0.70	0.052	0.049	0.051	0.11	0.068
magf-8x7	0.011	3.7	8.7e-3	2.4	-9.2	14	0.22	0.33	5.7e-3	0.87	0.97	0.90	0.82	0.73	0.075	0.040	0.054	0.11	0.069
mamr-10x4.5	0.87	6.8	0.066	4.6	-0.34	13	0.10	0.12	9.1e-3	0.99	0.98	0.98	0.80	0.87	0.029	0.027	0.035	0.10	0.079
mamr-8x4.5	0.97	6.7	0.087	4.0	-1.7	15	0.11	0.15	7.0e-3	0.98	0.96	0.95	0.92	0.90	0.030	0.041	0.041	0.065	0.066
gre-9x5	0.51	4.6	0.047	2.7	-4.3	30	0.16	0.15	7.6e-3	0.90	0.95	0.60	0.82	0.76	0.061	0.041	0.070	0.069	0.12

Table A2. Results of the model fitting as described in Section 3 for all propellers tested under axial flow in the dataset provided by [68]. Dimensioned units are in SI units (i.e., θ_{tip} is in radians, and c_{tip} is in meters).

Name	x^*							R^2		nRMSE	
	$c_{l,0}$	$c_{l,\alpha}$	$c_{d,0}$	$c_{d,\alpha}$	δ	θ_{tip}	c_{tip}	C_{FT}	C_{MQ}	C_{FT}	C_{MQ}
ance-8.5x6	8.0e-3	8.0	0.078	1.5	0.25	0.27	4.7e-3	0.97	0.97	0.048	0.048
ance-8.5x7	5.5e-3	9.8	0.085	2.3	0.24	0.29	3.8e-3	0.96	0.97	0.062	0.044
apc29ff-9x4	0.38	8.2	0.074	2.9	0.29	0.16	6.2e-3	0.98	0.99	0.042	0.026
apc29ff-9x5	0.013	9.9	0.082	2.0	0.30	0.23	4.6e-3	0.97	0.97	0.056	0.049
apccf-7.4x8.25	0.16	8.2	0.22	1.7	0.32	0.37	4.0e-3	0.93	0.98	0.072	0.037
apccf-7.8x6	7.4e-3	9.6	0.14	2.8	0.29	0.30	3.3e-3	0.94	0.98	0.072	0.039
apccf-7.8x7	3.1e-3	9.8	0.18	3.7	0.23	0.35	2.5e-3	0.91	0.98	0.083	0.037
apce-10x5	0.014	9.4	0.068	1.2	0.20	0.21	5.3e-3	0.98	0.97	0.044	0.051
apce-10x7	0.017	9.9	0.092	1.9	0.16	0.27	4.0e-3	0.95	0.97	0.062	0.047
apce-11x10	0.021	9.4	0.049	3.6	0.29	0.35	4.0e-3	0.88	0.95	0.10	0.056
apce-11x5.5	0.21	4.9	0.031	1.3	0.32	0.17	0.013	0.97	0.96	0.050	0.058
apce-11x7	3.1e-3	8.8	0.058	1.2	0.36	0.25	6.9e-3	0.96	0.96	0.058	0.062
apce-11x8	0.023	7.0	0.055	1.3	0.25	0.27	6.7e-3	0.94	0.96	0.071	0.061
apce-11x8.5	7.3e-3	9.5	0.084	2.2	0.24	0.29	4.6e-3	0.93	0.96	0.081	0.064
apce-14x12	0.012	9.9	0.078	3.6	0.21	0.32	4.2e-3	0.87	0.96	0.11	0.059
apce-17x12	0.0	9.8	0.053	2.8	0.31	0.29	6.6e-3	0.89	0.95	0.10	0.065
apce-19x12	5.8e-3	5.7	0.040	0.91	0.32	0.25	0.015	0.94	0.93	0.072	0.073
apce-8x4	0.49	7.4	0.080	2.7	0.13	0.18	4.5e-3	0.99	0.98	0.033	0.037
apce-8x6	5.9e-3	8.2	0.091	2.5	0.36	0.32	4.5e-3	0.94	0.97	0.077	0.049
apce-8x8	0.011	6.1	0.11	2.4	0.19	0.41	4.0e-3	0.90	0.97	0.090	0.043
apce-9x4.5	0.35	8.0	0.069	1.8	0.17	0.17	5.8e-3	0.98	0.98	0.046	0.044
apce-9x6	0.017	8.1	0.080	1.3	0.12	0.26	4.8e-3	0.98	0.98	0.042	0.041
apce-9x7.5	4.6e-4	4.6	0.061	1.4	0.16	0.33	7.2e-3	0.93	0.96	0.080	0.051
apce-9x9	0.027	9.4	0.11	3.4	0.33	0.38	3.9e-3	0.92	0.97	0.079	0.044
apcff-4.2x4	3.9e-3	8.2	0.22	4.0	0.22	0.34	1.9e-3	0.96	0.98	0.056	0.032
apcff-9x4	0.33	8.2	0.089	3.0	0.11	0.16	5.4e-3	0.98	0.99	0.044	0.029
apcsf-10x4.7	0.81	6.5	0.050	3.3	0.20	0.14	0.010	0.99	0.97	0.031	0.042
apcsf-10x7	0.77	6.4	0.064	2.6	0.26	0.20	9.9e-3	0.98	0.96	0.037	0.053
apcsf-11x3.8	0.59	6.3	0.029	4.5	0.37	0.092	0.017	0.99	0.98	0.030	0.040
apcsf-11x4.7	0.75	5.8	0.040	3.6	0.13	0.12	0.013	0.98	0.97	0.034	0.047
apcsf-11x7	1.0	8.0	0.083	3.0	0.21	0.19	8.7e-3	0.99	0.98	0.032	0.042
apcsf-8x3.8	0.65	5.5	0.056	3.3	0.22	0.13	8.5e-3	0.99	0.98	0.031	0.036
apcsf-8x6	0.66	8.7	0.11	2.9	0.27	0.27	4.8e-3	0.98	0.97	0.041	0.042
apcsf-9x3.8	0.65	5.7	0.045	3.6	0.20	0.11	0.010	0.98	0.97	0.032	0.041
apcsf-9x4.7	0.66	6.7	0.041	4.2	0.40	0.13	0.012	0.99	0.99	0.021	0.024
apcsf-9x6	0.64	6.5	0.067	2.2	0.32	0.23	8.9e-3	0.98	0.95	0.041	0.057
apcsf-9x7.5	0.69	7.2	0.097	3.1	0.24	0.28	6.5e-3	0.97	0.94	0.045	0.057
apcsp-10x10	9.5e-3	9.0	0.23	3.9	0.34	0.37	4.0e-3	0.93	0.99	0.074	0.029
apcsp-10x3	0.35	9.7	0.062	4.2	0.40	0.13	6.8e-3	0.97	0.99	0.049	0.030
apcsp-10x4	0.38	7.7	0.065	2.4	0.27	0.15	7.7e-3	0.98	0.99	0.036	0.024
apcsp-10x5	0.042	9.5	0.075	1.7	0.27	0.22	5.8e-3	0.98	0.98	0.042	0.033
apcsp-10x6	8.1e-3	8.5	0.092	1.3	0.14	0.26	5.0e-3	0.96	0.97	0.058	0.046
apcsp-10x7	0.015	9.5	0.11	2.0	0.28	0.27	4.9e-3	0.94	0.96	0.071	0.052
apcsp-10x8	6.7e-3	9.9	0.12	2.6	0.19	0.31	3.7e-3	0.91	0.95	0.089	0.059
apcsp-10x9	0.011	8.3	0.14	2.8	0.24	0.35	4.2e-3	0.89	0.96	0.095	0.048
apcsp-11x3	0.49	8.4	0.080	3.8	0.18	0.11	6.4e-3	0.98	0.99	0.042	0.027
apcsp-11x4	0.54	9.9	0.10	4.3	0.25	0.14	5.7e-3	0.97	0.99	0.051	0.028
apcsp-11x5	0.21	8.7	0.067	1.7	0.38	0.19	8.2e-3	0.97	0.98	0.052	0.042
apcsp-11x6	0.026	8.7	0.084	1.2	0.32	0.24	7.0e-3	0.96	0.98	0.057	0.045

Table A2. Cont.

Name	x^*							R^2		nRMSE	
	$c_{l,0}$	$c_{l,\alpha}$	$c_{d,0}$	$c_{d,\alpha}$	δ	θ_{tip}	c_{tip}	C_{FT}	C_{MQ}	C_{FT}	C_{MQ}
apcsp-11x7	0.033	7.6	0.091	1.3	0.18	0.27	6.1e-3	0.95	0.97	0.063	0.045
apcsp-11x8	2.0e-3	9.5	0.11	1.5	0.30	0.30	5.4e-3	0.94	0.96	0.068	0.049
apcsp-11x9	0.014	9.7	0.11	2.4	0.18	0.34	3.8e-3	0.90	0.93	0.087	0.062
apcsp-14x13	5.6e-3	8.1	0.081	2.7	0.37	0.36	6.9e-3	0.89	0.94	0.096	0.060
apcsp-4.2x2	0.29	6.0	0.083	3.9	0.17	0.16	3.2e-3	0.98	0.99	0.038	0.024
apcsp-7x6	5.8e-4	5.1	0.13	1.9	0.33	0.32	4.5e-3	0.94	0.98	0.067	0.033
apcsp-7x9	0.016	7.4	0.18	3.4	0.36	0.50	2.4e-3	0.82	0.94	0.11	0.054
apcsp-8x10	0.014	6.8	0.46	3.2	0.11	0.47	2.4e-3	0.89	0.97	0.074	0.036
apcsp-8x4	0.010	9.9	0.11	3.0	0.21	0.21	3.3e-3	0.98	0.99	0.041	0.030
apcsp-8x5	1.6e-3	9.6	0.15	2.7	0.33	0.25	3.6e-3	0.97	0.99	0.046	0.027
apcsp-8x6	4.2e-3	5.6	0.13	1.5	0.23	0.29	5.0e-3	0.95	0.99	0.063	0.031
apcsp-8x7	5.2e-4	9.6	0.18	2.7	0.36	0.32	3.4e-3	0.89	0.96	0.098	0.054
apcsp-8x8	1.9e-3	8.3	0.26	3.0	0.20	0.39	2.5e-3	0.88	0.96	0.093	0.046
apcsp-8x9	5.3e-3	9.3	0.47	3.8	0.22	0.46	1.9e-3	0.83	0.94	0.090	0.046
apcsp-9x10	0.028	9.8	0.25	3.0	0.23	0.41	2.6e-3	0.92	0.93	0.076	0.057
apcsp-9x6	1.5e-3	6.2	0.078	1.4	0.24	0.27	6.5e-3	0.95	0.97	0.060	0.043
apcsp-9x7	9.4e-3	8.9	0.11	1.9	0.20	0.30	3.9e-3	0.94	0.95	0.076	0.058
apcsp-9x8	5.7e-3	7.9	0.20	2.7	0.11	0.33	3.3e-3	0.92	0.98	0.086	0.041
apcsp-9x9	2.8e-3	9.6	0.23	4.4	0.39	0.38	3.2e-3	0.92	0.98	0.073	0.036
da4002-5x1.58	0.16	6.3	0.080	3.5	0.11	0.14	4.0e-3	0.97	0.98	0.057	0.036
da4002-5x2.65	9.4e-3	7.2	0.11	3.5	0.11	0.21	3.1e-3	0.99	0.99	0.037	0.028
da4002-5x3.75	2.3e-3	8.8	0.15	4.5	0.13	0.29	2.3e-3	0.98	0.99	0.045	0.023
da4002-5x4.92	6.0e-4	8.7	0.19	5.0	0.25	0.38	2.3e-3	0.96	0.99	0.059	0.029
da4002-9x2.85	1.4e-3	9.7	0.070	2.6	0.23	0.16	5.6e-3	0.99	0.98	0.032	0.034
da4002-9x4.76	0.039	8.5	0.087	2.3	0.11	0.22	4.9e-3	0.99	0.99	0.030	0.030
da4002-9x6.75	0.019	7.9	0.082	2.8	0.21	0.29	5.3e-3	0.98	0.98	0.037	0.033
da4002-9x8.95	0.029	8.4	0.090	3.9	0.16	0.37	4.0e-3	0.97	0.98	0.053	0.035
da4022-5x3.75	0.31	7.3	0.074	4.9	0.38	0.23	8.3e-3	0.89	0.73	0.093	0.13
da4022-9x6.75	0.029	7.2	0.066	2.0	0.28	0.25	0.012	0.88	0.69	0.091	0.13
da4052-5x1.58	0.24	6.5	0.063	5.0	0.26	0.10	4.4e-3	0.99	0.87	0.025	0.10
da4052-5x2.65	0.38	8.4	0.090	5.0	0.23	0.15	3.3e-3	1.0	0.94	0.016	0.067
da4052-5x3.75	6.6e-3	6.4	0.080	3.0	0.26	0.24	5.7e-3	0.93	0.83	0.072	0.10
da4052-5x4.92	0.29	6.7	0.084	4.7	0.19	0.28	3.4e-3	0.99	0.98	0.033	0.034
da4052-9x2.85	4.7e-3	5.1	0.051	2.1	0.14	0.13	8.3e-3	0.99	0.94	0.028	0.068
da4052-9x4.76	2.1e-3	7.1	0.068	1.7	0.18	0.19	6.4e-3	1.0	0.95	0.021	0.053
da4052-9x6.75	0.031	6.2	0.054	2.3	0.21	0.25	8.3e-3	0.93	0.83	0.077	0.099
da4052-9x8.95	0.24	7.6	0.059	4.4	0.29	0.31	5.3e-3	0.97	0.98	0.049	0.038
ef-130x70	0.51	7.1	0.058	4.7	0.30	0.16	4.4e-3	0.98	0.99	0.037	0.028
grcp-10x6	5.0e-3	7.1	0.091	0.94	0.12	0.23	5.5e-3	0.98	0.98	0.042	0.034
grcp-10x8	0.011	9.3	0.14	2.3	0.14	0.30	3.5e-3	0.95	0.97	0.063	0.043
grcp-11x4	0.44	8.8	0.078	3.0	0.23	0.12	6.0e-3	0.97	0.98	0.054	0.041
grcp-11x6	0.15	7.6	0.084	1.4	0.13	0.18	6.0e-3	0.97	0.98	0.053	0.044
grcp-11x8	0.011	8.2	0.078	1.8	0.36	0.29	6.1e-3	0.96	0.97	0.059	0.047
grcp-9x4	0.42	9.2	0.088	3.7	0.38	0.13	5.4e-3	0.98	0.99	0.040	0.030
grcp-9x6	0.020	7.9	0.11	1.4	0.19	0.24	4.7e-3	0.97	0.99	0.050	0.033
grcsp-10x6	0.70	9.6	0.095	2.1	0.32	0.22	6.0e-3	0.98	0.98	0.040	0.041
grcsp-10x8	3.4e-3	9.3	0.13	1.8	0.18	0.34	4.2e-3	0.96	0.98	0.060	0.038
grcsp-9x5	3.4e-3	8.8	0.059	1.8	0.18	0.20	4.7e-3	0.99	1.0	0.026	0.016
grcsp-9x6	2.3e-3	6.3	0.077	1.4	0.25	0.31	6.7e-3	0.97	0.99	0.048	0.027
grsn-10x6	0.021	8.1	0.054	1.4	0.28	0.22	7.9e-3	0.99	0.99	0.031	0.034

Table A2. Cont.

Name	x^*							R^2		<i>nRMSE</i>	
	$c_{l,0}$	$c_{l,\alpha}$	$c_{d,0}$	$c_{d,\alpha}$	δ	θ_{tip}	c_{tip}	C_{FT}	C_{MQ}	C_{FT}	C_{MQ}
grsn-10x7	5.1e-3	9.3	0.083	1.5	0.18	0.27	5.4e-3	0.98	0.97	0.042	0.049
grsn-11x10	0.013	8.6	0.12	0.94	0.23	0.31	6.6e-3	0.98	0.98	0.045	0.042
grsn-11x6	0.022	9.7	0.059	1.6	0.26	0.19	7.7e-3	0.99	0.98	0.034	0.036
grsn-11x7	3.7e-3	9.6	0.081	1.7	0.11	0.23	5.6e-3	0.98	0.99	0.040	0.036
grsn-11x8	4.9e-3	8.3	0.080	1.2	0.10	0.25	6.5e-3	0.98	0.97	0.040	0.049
grsn-9x4	0.48	9.8	0.097	3.5	0.14	0.15	5.0e-3	0.99	0.99	0.036	0.023
grsn-9x5	5.4e-3	8.8	0.073	1.5	0.28	0.21	6.5e-3	0.99	0.99	0.036	0.031
grsn-9x6	0.016	8.7	0.080	1.4	0.28	0.25	6.3e-3	0.98	0.98	0.041	0.036
grsn-9x7	6.8e-3	9.8	0.12	1.3	0.31	0.31	5.2e-3	0.98	0.96	0.046	0.052
gwsdd-10x6	0.63	9.8	0.075	1.9	0.23	0.16	5.6e-3	0.99	0.99	0.030	0.032
gwsdd-11x7	0.48	6.4	0.043	1.7	0.25	0.16	0.011	0.99	0.99	0.027	0.034
gwsdd-2.5x0.8	0.20	4.6	0.053	4.9	0.12	0.092	3.6e-3	1.0	0.71	0.019	0.076
gwsdd-2.5x1	0.30	5.2	0.052	5.0	0.16	0.098	3.6e-3	1.0	0.94	0.016	0.060
gwsdd-3x2	0.43	5.9	0.055	4.8	0.30	0.16	4.4e-3	1.0	0.98	0.018	0.031
gwsdd-3x3	0.37	3.8	0.059	3.1	0.17	0.25	5.2e-3	0.99	1.0	0.023	0.014
gwsdd-4.5x3	0.32	4.6	0.037	3.3	0.34	0.16	7.5e-3	0.99	0.99	0.022	0.029
gwsdd-4.5x4	0.42	4.9	0.072	2.6	0.27	0.23	5.7e-3	1.0	0.98	0.021	0.038
gwsdd-4x2.5	0.39	5.1	0.042	4.8	0.12	0.15	5.5e-3	1.0	0.97	0.014	0.043
gwsdd-4x4	0.38	5.6	0.089	4.0	0.34	0.26	5.0e-3	0.99	1.0	0.031	0.016
gwsdd-5x3	0.45	6.5	0.042	5.0	0.34	0.14	6.4e-3	1.0	0.98	0.014	0.036
gwsdd-5x4.3	0.42	4.2	0.050	3.4	0.20	0.20	7.6e-3	0.96	0.81	0.059	0.095
gwsdd-9x5	0.53	5.4	0.042	3.1	0.12	0.14	8.8e-3	0.99	0.99	0.025	0.032
gwssf-10x4.7	0.48	5.1	0.032	3.8	0.28	0.14	0.017	1.0	0.99	0.019	0.025
gwssf-10x8	0.75	7.6	0.054	5.0	0.32	0.18	0.011	1.0	0.99	0.020	0.030
gwssf-11x4.7	0.63	6.0	0.044	4.8	0.11	0.12	0.014	0.99	0.98	0.025	0.042
gwssf-11x8	0.67	7.8	0.057	4.9	0.35	0.18	0.013	0.99	0.98	0.034	0.036
gwssf-8x4.3	0.56	5.8	0.039	4.5	0.14	0.14	8.5e-3	0.99	0.99	0.023	0.028
gwssf-8x6	0.93	8.9	0.071	4.5	0.27	0.19	6.1e-3	0.99	0.98	0.033	0.033
gwssf-9x4.7	0.55	5.7	0.046	4.8	0.15	0.13	0.012	0.99	0.98	0.029	0.038
gwssf-9x7	0.61	6.3	0.059	4.8	0.20	0.20	9.7e-3	0.98	0.99	0.042	0.028
kavfk-11x6	0.40	9.1	0.090	2.1	0.36	0.17	8.1e-3	0.97	0.98	0.046	0.039
kavfk-11x7.75	0.46	9.5	0.11	1.7	0.22	0.22	6.3e-3	0.99	0.98	0.035	0.037
kavfk-9x4	0.13	8.8	0.075	2.2	0.16	0.14	5.5e-3	0.98	0.99	0.043	0.034
kavfk-9x6	4.3e-3	8.1	0.083	1.6	0.31	0.25	6.4e-3	0.99	0.99	0.033	0.028
kpf-96x70	0.46	2.8	0.091	1.7	0.13	0.18	0.011	0.99	0.98	0.024	0.033
kyosho-10x6	7.5e-3	9.8	0.080	2.4	0.29	0.26	4.8e-3	0.96	0.99	0.055	0.028
kyosho-10x7	0.011	7.8	0.10	1.3	0.18	0.31	4.7e-3	0.93	0.93	0.072	0.063
kyosho-11x7	0.028	8.2	0.11	0.85	0.15	0.27	5.4e-3	0.96	0.96	0.058	0.059
kyosho-11x9	1.8e-3	9.7	0.11	1.9	0.34	0.35	4.4e-3	0.93	0.93	0.067	0.057
kyosho-9x6	0.041	8.5	0.12	0.92	0.22	0.25	5.0e-3	0.98	0.98	0.040	0.035
ma-11x10	7.8e-3	7.7	0.14	1.2	0.11	0.34	4.4e-3	0.91	0.88	0.084	0.080
ma-11x4	0.30	6.0	0.049	0.87	0.19	0.10	0.011	0.95	0.99	0.066	0.031
ma-11x6	0.028	8.5	0.081	0.65	0.21	0.20	6.7e-3	0.95	0.96	0.063	0.057
ma-11x7	0.043	9.6	0.10	0.61	0.22	0.21	5.7e-3	0.95	0.96	0.063	0.058
ma-11x8	5.8e-3	8.9	0.094	0.82	0.34	0.27	6.4e-3	0.95	0.94	0.065	0.063
ma-11x9	0.031	8.9	0.13	0.90	0.26	0.30	5.2e-3	0.94	0.93	0.063	0.055
ma-9x4	5.8e-3	9.6	0.10	1.1	0.17	0.17	4.4e-3	0.96	0.97	0.059	0.047
ma-9x6	0.021	9.5	0.12	1.3	0.21	0.25	4.0e-3	0.94	0.94	0.068	0.064
ma-9x8	0.026	9.2	0.17	1.4	0.20	0.33	3.4e-3	0.91	0.91	0.084	0.076
mae-10x7	0.93	4.9	0.12	1.3	0.11	0.19	7.9e-3	0.95	0.97	0.057	0.049
mae-11x7	0.49	3.4	0.066	1.3	0.35	0.19	0.017	0.97	0.98	0.039	0.035
mae-9x6	0.95	6.9	0.21	2.8	0.26	0.20	5.3e-3	0.97	0.99	0.041	0.024

Table A2. *Cont.*

Name	x^*							R^2		$nRMSE$	
	$c_{l,0}$	$c_{l,\alpha}$	$c_{d,0}$	$c_{d,\alpha}$	δ	θ_{tip}	c_{tip}	C_{FT}	C_{MQ}	C_{FT}	C_{MQ}
magf-10x6	2.6e-4	4.3	0.035	0.47	0.32	0.23	0.013	0.97	0.97	0.049	0.045
magf-10x8	6.2e-3	8.9	0.11	0.92	0.22	0.29	5.1e-3	0.97	0.96	0.054	0.052
magf-11x4	0.28	9.5	0.068	1.8	0.24	0.14	6.3e-3	0.97	0.98	0.049	0.037
magf-11x5	0.12	8.0	0.065	0.87	0.27	0.17	7.4e-3	0.97	0.95	0.052	0.053
magf-11x8	5.9e-3	8.5	0.11	0.86	0.14	0.28	5.4e-3	0.96	0.97	0.055	0.047
magf-7x4	0.23	10	0.19	2.8	0.11	0.19	2.6e-3	0.98	0.98	0.035	0.033
magf-8x4	0.013	7.7	0.076	1.1	0.28	0.20	5.7e-3	0.98	0.99	0.039	0.034
magf-9x4	6.6e-3	8.3	0.062	1.3	0.33	0.18	6.4e-3	0.97	0.97	0.049	0.043
magf-9x5	6.8e-4	5.1	0.052	0.74	0.16	0.22	8.0e-3	0.98	0.98	0.045	0.037
magf-9x7	8.0e-3	8.5	0.11	1.1	0.12	0.29	4.2e-3	0.97	0.97	0.047	0.043
mas-10x5	0.76	6.7	0.13	3.8	0.23	0.15	6.6e-3	0.99	0.99	0.033	0.035
mas-10x7	9.5e-3	9.7	0.13	0.54	0.30	0.26	5.5e-3	0.96	0.97	0.061	0.046
mas-11x6	0.014	9.7	0.14	1.5	0.36	0.22	5.4e-3	0.96	0.99	0.056	0.034
mas-11x7	0.21	8.7	0.12	1.8	0.28	0.22	5.8e-3	0.98	0.99	0.043	0.034
mas-11x8	0.043	8.2	0.14	0.60	0.14	0.26	5.5e-3	0.95	0.97	0.063	0.047
mas-9x5	2.8e-4	6.0	0.12	1.3	0.32	0.21	6.2e-3	0.98	1.0	0.036	0.018
mas-9x6	0.023	9.0	0.15	1.7	0.29	0.24	4.4e-3	0.97	0.99	0.043	0.025
mas-9x7	0.74	8.5	0.16	1.7	0.15	0.21	4.4e-3	0.98	0.99	0.039	0.033
mi-3.2x2.2	0.56	4.8	0.052	4.7	0.15	0.14	4.1e-3	0.98	0.93	0.042	0.056
mi-4x2.7	0.43	4.9	0.072	4.7	0.14	0.12	5.3e-3	0.98	0.73	0.038	0.12
mi-5x3.5	0.21	3.1	0.018	4.4	0.12	0.10	0.015	0.98	0.80	0.041	0.11
mit-4.3x3.5	0.36	6.2	0.061	3.3	0.37	0.16	6.4e-3	0.97	0.92	0.050	0.074
mit-5x4	0.61	6.8	0.097	4.8	0.20	0.21	4.2e-3	0.98	0.99	0.042	0.029
pl-100x80	7.3e-3	6.7	0.10	2.4	0.22	0.31	2.4e-3	0.95	0.97	0.066	0.048
pl-57x20	0.96	5.7	0.13	2.4	0.17	0.13	2.6e-3	1.0	0.94	0.019	0.063
rusp-11x4	0.35	5.9	0.053	2.9	0.28	0.12	0.011	0.98	0.99	0.040	0.026
vp-140x45	0.26	4.2	0.027	4.4	0.19	0.091	7.9e-3	0.99	0.96	0.038	0.048
zin-11x7	0.22	8.3	0.15	2.6	0.32	0.19	6.2e-3	0.99	1.0	0.030	0.012
zin-9x6	0.56	9.3	0.22	3.3	0.36	0.18	4.8e-3	0.99	1.0	0.025	0.017

Table A3. Results of the model as described in Section 4 for all propellers tested under oblique flow. Dimensioned units are in SI units (i.e., θ_{tip} is in radians, and c_{tip} is in meters). Data for gre-9x5 is provided by [7].

Name	x								R^2					$nRMSE$					
	$c_{I,0}$	$c_{I,\alpha}$	$c_{d,0}$	$c_{d,\alpha}$	$c_{m,0}$	$c_{m,\alpha}$	δ	θ_{tip}	c_{tip}	C_{FT}	C_{FH}	C_{MQ}	C_{MR}	C_{MP}	C_{FT}	C_{FH}	C_{MQ}	C_{MR}	C_{MP}
ance-12x6	0.0	4.1	0.050	0.39	0.0	0.0	0.20	0.20	0.017	0.87	0.89	0.53	0.93	-0.36	0.10	0.060	0.19	0.069	0.22
ance-9x5	0.0	3.9	0.050	0.43	0.0	0.0	0.20	0.22	0.013	0.94	0.90	0.77	0.92	-0.55	0.048	0.063	0.082	0.061	0.25
apce-10x7	0.0	3.8	0.050	1.0	0.0	0.0	0.20	0.28	9.7e-3	0.90	0.86	0.88	0.99	-0.84	0.055	0.077	0.039	0.024	0.31
apce-12x6	0.0	5.0	0.050	0.88	0.0	0.0	0.20	0.20	0.010	0.97	0.86	0.72	0.92	-0.35	0.043	0.087	0.12	0.061	0.23
apce-6x4	0.0	3.3	0.050	1.2	0.0	0.0	0.20	0.27	7.1e-3	0.78	0.66	0.86	0.94	-0.28	0.071	0.11	0.056	0.059	0.17
apce-8x6	0.0	3.3	0.050	0.89	0.0	0.0	0.20	0.30	9.4e-3	0.94	0.84	0.90	0.97	-0.58	0.052	0.080	0.053	0.041	0.19
apce-8x8	0.0	2.6	0.050	1.1	0.0	0.0	0.20	0.40	9.2e-3	0.83	0.92	0.85	0.99	-0.81	0.077	0.055	0.064	0.028	0.25
apcsf-10x4.7	0.0	5.2	0.050	0.39	0.0	0.0	0.20	0.19	0.015	0.84	0.91	-0.71	0.73	-0.54	0.074	0.062	0.16	0.11	0.28
apcsf-8x3.5	0.0	5.2	0.050	6.1e-5	0.0	0.0	0.20	0.17	0.013	0.83	0.86	-0.93	0.82	-0.43	0.083	0.084	0.25	0.084	0.27
ef4b-10x6	0.0	1.7	0.050	8.2e-6	0.0	0.0	0.20	0.24	0.019	0.87	0.89	0.27	0.62	-0.34	0.079	0.078	0.17	0.14	0.24
grc-10x4	0.0	3.3	0.050	1.4e-4	0.0	0.0	0.20	0.16	0.011	0.90	0.67	0.40	0.45	-2.1e-3	0.080	0.099	0.18	0.11	0.17
hqp-7x4.5	0.0	2.7	0.050	0.49	0.0	0.0	0.20	0.26	0.012	0.95	0.87	0.68	0.97	-0.062	0.044	0.085	0.089	0.041	0.17
hqp-8x4.5	0.0	4.7	0.050	2.0	0.0	0.0	0.20	0.22	8.2e-3	0.87	0.94	-0.44	0.94	-1.3	0.070	0.061	0.18	0.061	0.37
ma3b-10x5	0.0	2.3	0.050	0.39	0.0	0.0	0.20	0.20	0.013	0.85	0.81	0.79	0.52	-0.14	0.10	0.094	0.12	0.15	0.16
ma3b-8x6	0.0	2.0	0.050	0.71	0.0	0.0	0.20	0.30	0.010	0.84	0.96	0.74	0.77	-0.016	0.086	0.048	0.089	0.13	0.15
mae-12x6	0.0	3.6	0.050	1.2	0.0	0.0	0.20	0.20	0.016	0.95	0.94	-0.27	0.75	-0.15	0.052	0.057	0.19	0.11	0.13
magf-8x7	0.0	1.8	0.050	0.88	0.0	0.0	0.20	0.35	0.010	0.85	0.96	0.77	0.84	-0.28	0.082	0.046	0.081	0.11	0.15
mamr-10x4.5	0.0	5.2	0.050	0.29	0.0	0.0	0.20	0.18	0.015	0.95	0.92	-0.77	0.79	-0.23	0.061	0.061	0.30	0.10	0.24
mamr-8x4.5	0.0	4.5	0.050	0.82	0.0	0.0	0.20	0.22	0.012	0.94	0.90	0.55	0.93	-0.59	0.051	0.063	0.12	0.061	0.26
gre-9x5	0.0	4.6	0.050	0.84	0.0	0.0	0.20	0.22	7.3e-3	0.88	0.84	0.55	0.86	-2.3	0.065	0.075	0.074	0.061	0.46

Table A4. Results of the model as described in Section 4 for all propellers tested under axial flow in the dataset provided by [68]. Dimensioned units are in SI units (i.e., θ_{tip} is in radians, and c_{tip} is in meters).

Name	x						R^2		nRMSE		
	$c_{l,0}$	$c_{l,\alpha}$	$c_{d,0}$	$c_{d,\alpha}$	δ	θ_{tip}	c_{tip}	C_{FT}	C_{MQ}	C_{FT}	C_{MQ}
apc29ff-9x5	0.0	4.7	0.050	1.3	0.20	0.22	8.3e-3	0.89	0.88	0.10	0.10
apce-10x5	0.0	5.7	0.050	0.68	0.20	0.20	9.0e-3	0.93	0.92	0.081	0.085
apce-10x7	0.0	3.9	0.050	0.97	0.20	0.28	9.0e-3	0.90	0.95	0.094	0.064
apce-11x10	0.0	2.6	0.050	1.2	0.20	0.36	0.010	0.73	0.92	0.15	0.071
apce-11x5.5	0.0	5.4	0.050	0.53	0.20	0.20	9.1e-3	0.97	0.92	0.054	0.083
apce-11x7	0.0	4.4	0.050	0.62	0.20	0.25	0.010	0.94	0.94	0.077	0.074
apce-11x8	0.0	3.7	0.050	0.90	0.20	0.29	9.6e-3	0.88	0.91	0.10	0.089
apce-11x8.5	0.0	3.3	0.050	1.0	0.20	0.31	9.7e-3	0.86	0.91	0.12	0.090
apce-14x12	0.0	2.9	0.050	1.3	0.20	0.34	0.010	0.77	0.90	0.15	0.087
apce-17x12	0.0	3.6	0.050	1.5	0.20	0.28	0.013	0.72	0.90	0.16	0.089
apce-19x12	0.0	4.8	0.050	0.91	0.20	0.25	0.014	0.90	0.90	0.093	0.089
apce-9x4.5	0.0	4.7	0.050	0.47	0.20	0.20	9.9e-3	0.97	0.96	0.051	0.054
apce-9x6	0.0	3.7	0.050	0.59	0.20	0.27	9.9e-3	0.97	0.94	0.057	0.074
apcff-4.2x4	0.0	2.3	0.050	1.2	0.20	0.38	5.3e-3	0.93	0.96	0.078	0.049
apcff-9x4	0.0	5.4	0.050	1.4	0.20	0.18	9.4e-3	0.97	0.97	0.051	0.051
apcsf-10x4.7	0.0	5.6	0.050	0.23	0.20	0.19	0.014	0.88	0.12	0.092	0.24
apcsf-10x7	0.0	3.8	0.050	0.52	0.20	0.28	0.014	0.97	0.95	0.046	0.061
apcsf-11x3.8	0.0	5.9	0.050	1.7e-5	0.20	0.14	0.017	0.88	-3.0	0.097	0.52
apcsf-11x4.7	0.0	6.2	0.050	2.4e-5	0.20	0.17	0.015	0.87	-0.71	0.10	0.35
apcsf-11x7	0.0	4.3	0.050	0.58	0.20	0.25	0.017	0.95	0.81	0.065	0.12
apcsf-9x4.7	0.0	4.2	0.050	0.12	0.20	0.21	0.013	0.99	0.86	0.029	0.10
apcsf-9x6	0.0	3.9	0.050	0.73	0.20	0.27	0.013	0.89	0.76	0.090	0.13
apcsp-10x6	0.0	4.7	0.050	1.3	0.20	0.24	9.6e-3	0.83	0.77	0.12	0.13
apcsp-10x8	0.0	3.0	0.050	1.2	0.20	0.32	9.8e-3	0.79	0.90	0.13	0.079
apcsp-11x4	0.0	7.9	0.050	2.9	0.20	0.14	9.4e-3	0.70	-0.22	0.16	0.31
apcsp-11x5	0.0	7.1	0.050	1.9	0.20	0.18	9.3e-3	0.81	0.37	0.13	0.23
apcsp-11x6	0.0	5.8	0.050	1.7	0.20	0.22	9.5e-3	0.83	0.52	0.12	0.20
apcsp-11x7	0.0	4.9	0.050	1.6	0.20	0.25	9.4e-3	0.84	0.67	0.12	0.16
apcsp-11x8	0.0	4.2	0.050	1.3	0.20	0.29	9.4e-3	0.84	0.79	0.11	0.12
apcsp-11x9	0.0	3.5	0.050	1.5	0.20	0.33	9.6e-3	0.68	0.74	0.15	0.12
apcsp-14x13	0.0	2.8	0.050	1.3	0.20	0.37	0.013	0.78	0.91	0.14	0.075
apcsp-4.2x2	0.0	3.6	0.050	1.6	0.20	0.19	5.2e-3	0.97	0.98	0.045	0.032
apcsp-9x6	0.0	3.6	0.050	1.1	0.20	0.27	9.7e-3	0.92	0.95	0.078	0.058
apcsp-9x7	0.0	3.2	0.050	1.0	0.20	0.31	8.5e-3	0.86	0.91	0.11	0.082
da4002-5x1.58	0.0	3.9	0.050	3.6e-5	0.20	0.13	0.011	0.79	0.93	0.15	0.073
da4002-5x2.65	0.0	2.1	0.050	0.61	0.20	0.21	0.011	0.98	0.88	0.040	0.10
da4002-5x3.75	0.0	1.8	0.050	0.78	0.20	0.30	0.011	0.97	0.91	0.054	0.083
da4002-5x4.92	0.0	1.4	0.050	0.82	0.20	0.39	0.011	0.94	0.97	0.076	0.054
da4002-9x2.85	0.0	4.5	0.050	1.5e-3	0.20	0.13	0.020	0.61	0.58	0.19	0.17
da4002-9x4.76	0.0	2.6	0.050	0.13	0.20	0.21	0.019	0.97	0.86	0.052	0.10
da4002-9x6.75	0.0	1.9	0.050	0.47	0.20	0.30	0.020	0.98	0.76	0.044	0.13
da4002-9x8.95	0.0	1.5	0.050	0.63	0.20	0.40	0.019	0.95	0.75	0.070	0.13
da4022-5x3.75	0.0	1.7	0.050	0.38	0.20	0.30	0.014	0.63	0.35	0.17	0.20
da4022-9x6.75	0.0	1.7	0.050	0.089	0.20	0.30	0.026	0.71	0.32	0.14	0.19
da4052-5x3.75	0.0	3.2	0.050	1.4	0.20	0.30	5.6e-3	0.76	0.61	0.13	0.16
da4052-9x6.75	0.0	3.1	0.050	0.86	0.20	0.30	0.010	0.82	0.62	0.12	0.15
ef-130x70	0.0	3.8	0.050	0.70	0.20	0.21	6.5e-3	0.98	0.89	0.043	0.093
grcp-10x6	0.0	3.6	0.050	0.56	0.20	0.24	0.011	0.97	0.97	0.051	0.047
grcp-10x8	0.0	2.8	0.050	0.88	0.20	0.32	9.8e-3	0.91	0.93	0.086	0.067
grcp-11x4	0.0	4.7	0.050	0.33	0.20	0.14	0.011	0.96	0.95	0.058	0.064
grcp-11x6	0.0	3.7	0.050	0.46	0.20	0.22	0.011	0.92	0.71	0.083	0.15
grcp-11x8	0.0	3.2	0.050	0.87	0.20	0.29	0.011	0.90	0.95	0.087	0.058
grcp-9x4	0.0	3.9	0.050	0.76	0.20	0.18	8.7e-3	0.96	0.95	0.052	0.062
grcp-9x6	0.0	3.3	0.050	0.85	0.20	0.27	8.9e-3	0.94	0.94	0.071	0.069
grcsp-10x6	0.0	4.9	0.050	0.94	0.20	0.24	0.011	0.89	0.66	0.10	0.17
grcsp-10x8	0.0	3.6	0.050	1.1	0.20	0.32	0.011	0.85	0.79	0.11	0.12

Table A4. Cont.

Name	x						R^2		nRMSE		
	$c_{l,0}$	$c_{l,\alpha}$	$c_{d,0}$	$c_{d,\alpha}$	δ	θ_{tip}	c_{tip}	C_{FT}	C_{MQ}	C_{FT}	C_{MQ}
grcsp-9x5	0.0	3.8	0.050	0.42	0.20	0.22	9.2e-3	0.97	0.64	0.053	0.17
grcsp-9x6	0.0	3.9	0.050	1.4	0.20	0.27	0.011	0.75	0.48	0.14	0.20
grsn-10x6	0.0	3.1	0.050	0.13	0.20	0.24	0.015	0.97	0.62	0.053	0.18
grsn-10x7	0.0	3.0	0.050	0.30	0.20	0.28	0.015	0.97	0.84	0.055	0.11
grsn-11x6	0.0	3.3	0.050	1.1e-5	0.20	0.22	0.017	0.95	0.33	0.068	0.24
grsn-11x8	0.0	2.6	0.050	0.16	0.20	0.29	0.017	0.92	0.40	0.085	0.23
grsn-9x5	0.0	3.2	0.050	0.23	0.20	0.22	0.014	0.98	0.81	0.047	0.12
grsn-9x7	0.0	2.8	0.050	0.43	0.20	0.31	0.014	0.94	0.93	0.074	0.073
gwsdd-10x6	0.0	3.0	0.050	0.015	0.20	0.24	0.013	0.91	0.13	0.091	0.26
gwsdd-11x7	0.0	3.0	0.050	4.4e-3	0.20	0.25	0.014	0.86	-0.17	0.11	0.32
gwsdd-2.5x0.8	0.0	1.6	0.050	5.0e-4	0.20	0.13	9.8e-3	0.97	-6.6	0.049	0.39
gwsdd-2.5x1	0.0	1.5	0.050	2.3e-4	0.20	0.16	9.0e-3	0.89	-6.9	0.10	0.71
gwsdd-3x2	0.0	1.5	0.050	7.4e-6	0.20	0.27	0.010	0.86	-0.52	0.11	0.30
gwsdd-3x3	0.0	2.0	0.050	0.64	0.20	0.40	6.4e-3	0.82	0.26	0.13	0.22
gwsdd-4.5x3	0.0	2.6	0.050	0.40	0.20	0.27	7.3e-3	0.85	0.10	0.12	0.25
gwsdd-4.5x4	0.0	2.5	0.050	0.60	0.20	0.35	7.0e-3	0.86	0.42	0.11	0.19
gwsdd-4x2.5	0.0	1.8	0.050	9.8e-7	0.20	0.25	0.011	0.83	-0.88	0.13	0.34
gwsdd-4x4	0.0	2.1	0.050	0.74	0.20	0.40	7.0e-3	0.83	0.45	0.12	0.21
gwsdd-5x3	0.0	2.6	0.050	0.052	0.20	0.24	8.9e-3	0.85	-0.11	0.12	0.27
gwsdd-5x4.3	0.0	2.2	0.050	0.33	0.20	0.34	8.7e-3	0.77	0.16	0.14	0.20
gwsdd-9x5	0.0	3.5	0.050	1.2e-5	0.20	0.22	0.012	0.92	0.29	0.080	0.24
gwssf-10x4.7	0.0	5.9	0.050	0.38	0.20	0.19	0.015	0.97	0.68	0.050	0.16
gwssf-10x8	0.0	3.2	0.050	0.39	0.20	0.32	0.014	0.81	0.075	0.12	0.27
gwssf-11x4.7	0.0	5.9	0.050	2.3e-7	0.20	0.17	0.016	0.97	0.13	0.045	0.25
gwssf-11x8	0.0	3.3	0.050	0.60	0.20	0.29	0.016	0.87	0.46	0.099	0.18
gwssf-9x4.7	0.0	4.5	0.050	0.36	0.20	0.21	0.013	0.93	0.79	0.076	0.13
gwssf-9x7	0.0	3.2	0.050	0.74	0.20	0.31	0.014	0.85	0.39	0.10	0.19
kpf-96x70	0.0	2.4	0.050	0.76	0.20	0.29	0.012	0.97	0.61	0.047	0.15
kyosho-10x6	0.0	4.0	0.050	1.3	0.20	0.24	0.010	0.85	0.90	0.11	0.079
kyosho-10x7	0.0	3.4	0.050	0.98	0.20	0.28	0.010	0.71	0.58	0.15	0.16
kyosho-11x7	0.0	4.1	0.050	0.70	0.20	0.25	0.011	0.88	0.75	0.11	0.14
kyosho-11x9	0.0	2.9	0.050	0.84	0.20	0.33	0.011	0.77	0.73	0.12	0.11
kyosho-9x6	0.0	3.6	0.050	0.59	0.20	0.27	9.5e-3	0.96	0.95	0.056	0.057
ma-11x4	0.0	3.5	0.050	5.2e-5	0.20	0.14	0.015	0.91	-0.12	0.087	0.30
ma-11x6	0.0	3.0	0.050	0.031	0.20	0.22	0.015	0.94	0.74	0.074	0.14
ma-11x7	0.0	2.6	0.050	0.076	0.20	0.25	0.015	0.89	0.35	0.095	0.22
ma-11x8	0.0	2.4	0.050	0.21	0.20	0.29	0.016	0.91	0.75	0.083	0.13
ma-9x4	0.0	3.1	0.050	1.9e-3	0.20	0.18	0.013	0.95	0.77	0.064	0.13
ma-9x6	0.0	2.6	0.050	0.35	0.20	0.27	0.012	0.90	0.85	0.086	0.099
mae-10x7	0.0	3.4	0.050	0.69	0.20	0.28	0.013	0.90	0.34	0.085	0.21
mae-11x7	0.0	3.6	0.050	0.94	0.20	0.25	0.015	0.85	-0.53	0.090	0.30
mae-9x6	0.0	2.9	0.050	1.1	0.20	0.27	0.012	0.90	-0.38	0.077	0.29
magf-10x6	0.0	2.7	0.050	0.11	0.20	0.24	0.015	0.95	0.82	0.067	0.12
magf-10x8	0.0	2.3	0.050	0.21	0.20	0.32	0.015	0.94	0.73	0.074	0.14
mas-10x5	0.0	4.0	0.050	1.5	0.20	0.20	0.012	0.90	-0.45	0.086	0.35
mas-10x7	0.0	3.1	0.050	0.49	0.20	0.28	0.011	0.92	0.91	0.086	0.082
mas-11x6	0.0	3.3	0.050	0.89	0.20	0.22	0.012	0.94	0.90	0.065	0.088
mas-11x7	0.0	3.1	0.050	0.64	0.20	0.25	0.012	0.95	0.93	0.064	0.076
mas-11x8	0.0	3.0	0.050	0.44	0.20	0.29	0.013	0.92	0.90	0.083	0.080
mas-9x5	0.0	2.7	0.050	0.92	0.20	0.22	0.011	0.97	0.94	0.043	0.063
mas-9x7	0.0	2.7	0.050	0.41	0.20	0.31	0.011	0.91	0.80	0.087	0.12
mi-3.2x2.2	0.0	2.7	0.050	0.35	0.20	0.27	4.7e-3	0.80	0.20	0.12	0.19
mi-4x2.7	0.0	2.5	0.050	0.54	0.20	0.27	5.3e-3	0.65	0.32	0.17	0.19
mi-5x3.5	0.0	2.0	0.050	0.036	0.20	0.28	7.5e-3	0.30	-1.9	0.25	0.41
mit-4.3x3.5	0.0	2.2	0.050	0.36	0.20	0.32	5.8e-3	0.60	-0.13	0.18	0.28
mit-5x4	0.0	2.8	0.050	0.89	0.20	0.32	6.4e-3	0.87	0.78	0.11	0.14
pl-100x80	0.0	3.5	0.050	1.4	0.20	0.32	4.0e-3	0.92	0.94	0.084	0.067
pl-57x20	0.0	5.1	0.050	5.5e-4	0.20	0.14	8.4e-3	-0.96	-9.5	0.42	0.85
vp-140x45	0.0	4.7	0.050	2.8e-4	0.20	0.13	6.7e-3	0.98	0.46	0.043	0.18

Table A5. Results of the model fitting as described in Section 5 for all propellers tested under oblique flow. Data for gre-9x5 is provided by [7].

Name	k*												R ²					nRMSE						
	C _{FT} ^{static}	k ₁	k ₂	k ₃	k ₄	k ₅	C _{MQ} ^{static}	k ₆	k ₇	k ₈	k ₉	k ₁₀	k ₁₁	k ₁₂	C _{FT}	C _{FH}	C _{MQ}	C _{MR}	C _{MP}	C _{FT}	C _{FH}	C _{MQ}	C _{MR}	C _{MP}
ance-12x6	0.028	-0.061	0.14	-0.25	0.023	-1.0e-7	3.8e-3	1.0e-3	0.021	-0.062	0.022	-1.1e-8	4.4e-3	8.1e-8	0.99	0.91	0.99	0.94	0.10	0.026	0.056	0.029	0.061	0.18
ance-9x5	0.030	-0.058	0.14	-0.30	0.029	-3.7e-8	4.1e-3	4.0e-3	0.019	-0.070	0.027	-4.2e-8	8.0e-3	7.1e-8	0.99	0.97	0.96	0.96	0.54	0.022	0.037	0.032	0.045	0.13
apce-10x7	0.029	-0.027	0.14	-0.34	0.034	-3.6e-9	4.7e-3	4.1e-3	0.019	-0.065	0.029	-1.4e-10	6.6e-3	3.2e-8	0.97	0.98	0.94	0.94	0.49	0.030	0.029	0.026	0.055	0.16
apce-12x6	0.022	-0.078	0.12	-0.18	0.021	6.6e-9	2.7e-3	-2.8e-4	0.011	-0.045	0.017	-8.7e-9	5.1e-3	1.7e-8	0.99	0.99	0.97	0.87	0.29	0.029	0.025	0.037	0.077	0.17
apce-6x4	0.029	-0.038	0.16	-0.26	0.047	7.1e-8	5.2e-3	5.9e-4	0.018	-0.054	0.026	2.7e-8	-8.1e-4	2.5e-7	0.95	0.96	0.95	0.91	-0.36	0.035	0.037	0.034	0.071	0.18
apce-8x6	0.034	-0.038	0.14	-0.32	0.043	-1.4e-6	5.8e-3	3.6e-3	0.022	-0.068	0.032	-2.1e-8	4.5e-3	4.4e-8	0.98	0.96	0.94	0.94	0.11	0.031	0.041	0.042	0.059	0.14
apce-8x8	0.037	-1.2e-3	0.14	-0.32	0.055	5.3e-8	9.2e-3	-3.4e-3	0.037	-0.039	0.039	-3.7e-8	4.2e-3	1.2e-7	0.95	0.97	0.92	0.99	0.020	0.041	0.036	0.047	0.027	0.19
apcsf-10x4.7	0.032	-0.065	0.17	-0.41	0.025	-2.6e-8	4.2e-3	2.8e-3	0.012	-0.062	0.026	-1.5e-8	0.015	5.4e-8	0.98	0.96	0.96	0.94	0.53	0.024	0.042	0.025	0.050	0.15
apcsf-8x3.5	0.030	-0.078	0.19	-0.33	0.030	-3.2e-8	3.8e-3	7.0e-4	7.8e-3	-0.054	0.027	-1.4e-7	0.012	1.2e-7	0.99	0.96	0.97	0.91	0.44	0.016	0.042	0.034	0.060	0.17
ef4b-10x6	0.037	-0.091	0.21	-0.48	0.032	2.4e-8	5.8e-3	-4.7e-3	0.017	-0.067	0.026	-1.3e-8	0.018	2.5e-8	0.98	0.98	0.96	0.89	0.44	0.030	0.031	0.041	0.075	0.16
grc-10x4	0.016	-0.083	-1.6e-3	-0.21	0.012	8.1e-9	1.7e-3	-4.3e-3	2.2e-4	-0.023	7.6e-3	4.5e-8	-1.4e-3	8.3e-9	0.99	0.86	0.98	0.25	3.9e-3	0.030	0.065	0.032	0.12	0.17
hqp-7x4.5	0.032	-0.059	0.11	-0.30	0.035	1.0e-7	5.2e-3	1.7e-3	0.025	-0.057	0.030	2.3e-7	1.5e-3	7.0e-8	0.98	0.96	0.92	0.91	-3.4e-3	0.032	0.048	0.045	0.072	0.17
hqp-8x4.5	0.028	-0.022	0.080	-0.42	0.029	-7.8e-8	4.8e-3	-1.7e-3	0.023	-0.036	0.031	1.5e-7	5.2e-3	1.7e-7	0.97	0.95	0.97	0.95	0.19	0.031	0.056	0.027	0.055	0.22
ma3b-10x5	0.024	-0.097	-3.6e-3	-0.24	0.019	6.1e-9	4.0e-3	-7.7e-3	3.4e-3	-0.053	0.014	5.7e-8	-6.7e-3	1.5e-8	0.97	0.89	0.96	0.48	0.16	0.043	0.069	0.051	0.16	0.14
ma3b-8x6	0.033	-0.048	0.023	-0.34	0.034	5.6e-10	6.7e-3	2.5e-3	3.5e-3	-0.090	0.025	1.4e-7	-1.9e-3	5.9e-8	0.93	0.96	0.94	0.63	-0.060	0.056	0.044	0.042	0.16	0.15
mae-12x6	0.024	-0.046	2.7e-3	-0.31	0.019	4.0e-9	3.8e-3	-7.0e-6	1.1e-3	-0.039	0.018	3.0e-8	-4.6e-3	9.9e-9	0.97	0.97	0.95	0.76	0.25	0.038	0.042	0.038	0.11	0.11
magf-8x7	0.025	1.8e-3	7.2e-3	-0.30	0.032	-4.8e-8	6.3e-3	-9.2e-4	4.7e-3	-0.055	0.021	1.2e-7	-2.7e-3	-7.2e-9	0.94	0.96	0.93	0.80	0.22	0.051	0.047	0.045	0.12	0.12
mamr-10x4.5	0.029	-0.076	0.15	-0.37	0.028	2.4e-8	3.8e-3	-5.8e-4	0.013	-0.051	0.021	-2.1e-8	8.8e-3	4.5e-8	0.99	0.98	0.98	0.89	0.33	0.025	0.027	0.033	0.074	0.18
mamr-8x4.5	0.036	-0.067	0.17	-0.37	0.039	-2.4e-8	5.3e-3	1.2e-3	0.014	-0.064	0.032	-4.3e-9	0.012	5.5e-8	0.99	0.96	0.96	0.93	0.45	0.025	0.041	0.038	0.060	0.15
gre-9x5	0.023	-0.053	-0.012	-0.32	0.015	2.2e-4	2.7e-3	7.3e-3	4.0e-3	-0.080	0.020	7.2e-4	0.017	1.0e-3	0.92	0.94	0.77	0.79	0.47	0.055	0.045	0.053	0.075	0.18

Table A6. Results of the model fitting as described in Section 5 for all propellers tested under axial flow in the dataset provided by [68].

Name	C_{FT}^{static}	k^*			R^2		$nRMSE$	
		k_1	k_3	C_{MQ}^{static}	k_6	k_8	C_{FT}	C_{MQ}
ance-8.5x6	0.028	-0.017	-0.37	4.2e-3	0.012	-0.097	0.99	0.98
ance-8.5x7	0.030	-1.6e-3	-0.40	5.0e-3	9.5e-3	-0.086	0.99	0.96
apcff-9x4	0.023	-0.064	-0.30	3.1e-3	2.1e-3	-0.070	0.98	0.99
apcff-9x5	0.025	-0.022	-0.40	3.6e-3	9.4e-3	-0.095	0.98	0.98
apccf-7.4x8.25	0.037	8.5e-3	-0.31	8.4e-3	0.012	-0.074	0.98	0.97
apccf-7.8x6	0.027	9.5e-3	-0.36	5.3e-3	9.8e-3	-0.081	0.98	0.98
apccf-7.8x7	0.027	0.026	-0.34	6.7e-3	5.8e-3	-0.066	0.99	0.98
apce-10x5	0.025	-0.055	-0.32	3.1e-3	7.1e-3	-0.087	0.98	0.98
apce-10x7	0.028	-6.8e-3	-0.40	4.2e-3	0.011	-0.090	0.98	0.98
apce-11x10	0.027	0.045	-0.41	6.2e-3	7.4e-3	-0.071	0.98	0.95
apce-11x5.5	0.023	-0.069	-0.26	2.6e-3	4.4e-3	-0.076	0.97	0.97
apce-11x7	0.028	-0.028	-0.36	3.6e-3	0.012	-0.094	0.98	0.97
apce-11x8	0.027	4.7e-3	-0.43	4.1e-3	0.011	-0.089	0.98	0.96
apce-11x8.5	0.027	0.015	-0.42	4.5e-3	0.011	-0.087	0.98	0.96
apce-14x12	0.024	0.041	-0.43	5.0e-3	6.0e-3	-0.066	0.98	0.96
apce-17x12	0.023	0.035	-0.48	4.1e-3	8.1e-3	-0.075	0.98	0.95
apce-19x12	0.024	-1.7e-4	-0.44	3.2e-3	0.012	-0.094	0.98	0.95
apce-8x4	0.025	-0.072	-0.20	3.3e-3	3.1e-3	-0.067	0.99	0.99
apce-8x6	0.030	7.5e-3	-0.37	5.9e-3	7.4e-3	-0.074	0.98	0.97
apce-8x8	0.032	0.032	-0.33	9.0e-3	6.0e-3	-0.064	0.98	0.96
apce-9x4.5	0.026	-0.071	-0.30	3.2e-3	4.4e-3	-0.082	0.98	0.98
apce-9x6	0.030	-0.043	-0.31	4.2e-3	9.9e-3	-0.092	0.99	0.99
apce-9x7.5	0.032	0.012	-0.39	6.5e-3	7.1e-3	-0.075	0.98	0.96
apce-9x9	0.034	0.021	-0.34	8.3e-3	7.1e-3	-0.070	0.98	0.96
apcff-4.2x4	0.033	-5.4e-3	-0.30	9.2e-3	3.7e-3	-0.077	1.0	0.99
apcff-9x4	0.023	-0.075	-0.29	3.2e-3	3.7e-4	-0.070	0.98	0.99
apcsf-10x4.7	0.031	-0.062	-0.41	4.0e-3	2.9e-3	-0.067	0.99	0.98
apcsf-10x7	0.040	-0.063	-0.30	6.1e-3	5.9e-3	-0.080	0.99	0.97
apcsf-11x3.8	0.023	-0.063	-0.50	2.6e-3	4.4e-4	-0.043	0.99	0.98
apcsf-11x4.7	0.029	-0.060	-0.47	3.6e-3	1.5e-3	-0.059	0.99	0.97
apcsf-11x7	0.040	-0.065	-0.33	6.1e-3	6.1e-3	-0.084	0.99	0.98
apcsf-8x3.8	0.027	-0.053	-0.38	3.6e-3	1.5e-3	-0.053	0.99	0.98
apcsf-8x6	0.039	-0.036	-0.31	7.0e-3	6.9e-3	-0.077	0.99	0.97
apcsf-9x3.8	0.025	-0.058	-0.46	3.2e-3	5.5e-4	-0.051	0.99	0.97
apcsf-9x4.7	0.030	-0.074	-0.38	3.9e-3	1.7e-4	-0.056	1.0	0.99
apcsf-9x6	0.040	-0.051	-0.32	6.3e-3	7.4e-3	-0.083	0.98	0.96
apcsf-9x7.5	0.045	-0.040	-0.30	8.9e-3	2.8e-3	-0.069	0.98	0.94
apcsp-10x10	0.030	1.7e-3	-0.25	8.3e-3	3.1e-3	-0.059	0.97	0.99
apcsp-10x3	0.017	-0.061	-0.35	2.1e-3	-7.9e-4	-0.054	0.97	0.99
apcsp-10x4	0.023	-0.077	-0.27	3.0e-3	2.3e-3	-0.073	0.98	0.99
apcsp-10x5	0.027	-0.049	-0.36	3.6e-3	6.1e-3	-0.085	0.98	0.99
apcsp-10x6	0.029	-0.012	-0.43	4.1e-3	0.012	-0.097	0.98	0.97
apcsp-10x7	0.028	3.7e-3	-0.45	4.7e-3	0.011	-0.093	0.98	0.96
apcsp-10x8	0.029	0.032	-0.46	5.4e-3	0.012	-0.091	0.98	0.95
apcsp-10x9	0.029	0.032	-0.38	6.9e-3	8.5e-3	-0.074	0.98	0.96
apcsp-11x3	0.017	-0.067	-0.31	2.1e-3	-2.2e-6	-0.053	0.98	0.99
apcsp-11x4	0.020	-0.077	-0.22	2.7e-3	1.0e-3	-0.061	0.97	0.99
apcsp-11x5	0.025	-0.060	-0.31	3.3e-3	5.7e-3	-0.083	0.97	0.98
apcsp-11x6	0.028	-0.034	-0.36	4.0e-3	9.4e-3	-0.091	0.97	0.98
apcsp-11x7	0.030	-0.022	-0.35	4.5e-3	0.011	-0.090	0.97	0.97
apcsp-11x8	0.030	-4.1e-3	-0.37	4.9e-3	0.014	-0.095	0.97	0.97
apcsp-11x9	0.030	0.032	-0.42	5.7e-3	0.014	-0.089	0.98	0.94
apcsp-14x13	0.029	0.033	-0.38	6.7e-3	7.4e-3	-0.067	0.98	0.93
apcsp-4.2x2	0.021	-0.055	-0.32	3.6e-3	-3.8e-3	-0.049	0.98	0.99
apcsp-7x6	0.024	2.2e-3	-0.26	5.8e-3	5.6e-3	-0.061	0.99	0.99

Table A6. Cont.

Name	C_{FT}^{static}	k^*			R^2			$nRMSE$		
		k_1	k_3	C_{MQ}^{static}	k_6	k_8	C_{FT}	C_{MQ}	C_{FT}	
apcsp-7x9	0.027	0.047	-0.27	0.010	5.0e-3	-0.049	0.98	0.94	0.033	0.053
apcsp-8x10	0.030	0.020	-0.21	0.011	3.4e-3	-0.049	0.98	0.97	0.033	0.035
apcsp-8x4	0.022	-0.056	-0.23	3.3e-3	3.3e-3	-0.071	0.98	0.99	0.041	0.026
apcsp-8x5	0.024	-0.036	-0.26	4.1e-3	5.8e-3	-0.073	0.98	0.99	0.040	0.021
apcsp-8x6	0.026	-0.011	-0.29	5.1e-3	8.8e-3	-0.075	0.98	0.99	0.043	0.028
apcsp-8x7	0.026	0.033	-0.40	5.5e-3	0.012	-0.083	0.98	0.97	0.045	0.047
apcsp-8x8	0.027	0.034	-0.31	7.4e-3	9.3e-3	-0.066	0.98	0.96	0.034	0.043
apcsp-8x9	0.026	0.043	-0.28	9.1e-3	9.2e-3	-0.059	0.98	0.95	0.030	0.041
apcsp-9x10	0.030	0.014	-0.26	7.5e-3	9.9e-3	-0.063	0.98	0.92	0.037	0.061
apcsp-9x6	0.029	-0.019	-0.37	4.7e-3	8.9e-3	-0.087	0.97	0.98	0.045	0.041
apcsp-9x7	0.028	0.011	-0.41	4.8e-3	0.014	-0.096	0.98	0.96	0.038	0.050
apcsp-9x8	0.027	0.015	-0.34	6.4e-3	6.7e-3	-0.069	0.97	0.97	0.050	0.044
apcsp-9x9	0.027	7.2e-3	-0.24	8.0e-3	2.3e-3	-0.053	0.97	0.98	0.043	0.036
da4002-5x1.58	0.019	-0.077	-0.31	3.0e-3	-2.8e-3	-0.063	0.97	0.98	0.057	0.036
da4002-5x2.65	0.025	-0.046	-0.37	4.9e-3	-1.9e-3	-0.074	0.99	0.99	0.027	0.028
da4002-5x3.75	0.032	-0.028	-0.33	7.5e-3	-5.1e-4	-0.078	0.99	1.0	0.023	0.019
da4002-5x4.92	0.037	-3.0e-3	-0.28	0.012	3.6e-4	-0.077	1.0	1.0	0.017	0.020
da4002-9x2.85	0.021	-0.063	-0.41	2.8e-3	8.9e-4	-0.080	0.99	0.98	0.028	0.036
da4002-9x4.76	0.028	-0.056	-0.34	4.2e-3	3.6e-3	-0.085	0.99	0.99	0.024	0.033
da4002-9x6.75	0.035	-0.039	-0.31	6.7e-3	1.9e-3	-0.075	0.99	0.98	0.023	0.038
da4002-9x8.95	0.038	-0.011	-0.29	0.010	-1.8e-3	-0.062	1.0	0.98	0.020	0.038
da4022-5x3.75	0.054	-0.12	-0.33	0.012	-0.014	-0.082	0.89	0.73	0.093	0.13
da4022-9x6.75	0.050	-0.11	-0.36	9.1e-3	-6.7e-4	-0.11	0.88	0.69	0.091	0.13
da4052-5x1.58	0.014	-0.085	-0.22	2.0e-3	-3.2e-3	-0.041	1.0	0.87	0.024	0.10
da4052-5x2.65	0.023	-0.090	-0.20	3.5e-3	-2.7e-3	-0.058	1.0	0.94	0.016	0.067
da4052-5x3.75	0.038	-0.054	-0.44	8.1e-3	-6.0e-3	-0.087	0.93	0.83	0.068	0.10
da4052-5x4.92	0.036	-0.041	-0.28	8.9e-3	-0.010	-0.051	1.0	0.98	0.019	0.035
da4052-9x2.85	0.014	-0.051	-0.47	2.0e-3	-6.5e-4	-0.070	1.0	0.94	0.022	0.067
da4052-9x4.76	0.023	-0.056	-0.37	3.2e-3	4.2e-3	-0.090	1.0	0.96	0.012	0.050
da4052-9x6.75	0.034	-0.039	-0.42	6.1e-3	1.5e-3	-0.089	0.94	0.83	0.071	0.10
da4052-9x8.95	0.034	-0.015	-0.32	8.2e-3	-5.8e-3	-0.053	1.0	0.98	0.015	0.040
ef-130x70	0.026	-0.074	-0.27	3.8e-3	-2.8e-3	-0.050	0.98	0.99	0.037	0.026
grcp-10x6	0.025	-0.044	-0.30	3.4e-3	8.3e-3	-0.082	0.98	0.98	0.037	0.035
grcp-10x8	0.027	-5.8e-3	-0.32	4.7e-3	0.010	-0.080	0.98	0.97	0.038	0.042
grcp-11x4	0.016	-0.057	-0.34	1.9e-3	8.0e-4	-0.056	0.97	0.98	0.053	0.041
grcp-11x6	0.021	-0.057	-0.29	2.7e-3	4.8e-3	-0.076	0.97	0.98	0.052	0.043
grcp-11x8	0.028	-0.014	-0.32	4.5e-3	0.010	-0.081	0.98	0.97	0.042	0.048
grcp-9x4	0.017	-0.056	-0.28	2.3e-3	1.4e-3	-0.057	0.98	0.99	0.039	0.029
grcp-9x6	0.025	-0.029	-0.33	3.8e-3	8.4e-3	-0.083	0.98	0.99	0.038	0.034
grcsp-10x6	0.032	-0.040	-0.33	4.6e-3	9.8e-3	-0.087	0.99	0.99	0.027	0.032
grcsp-10x8	0.035	5.1e-5	-0.35	6.4e-3	0.014	-0.088	0.99	0.98	0.025	0.040
grcsp-9x5	0.023	-0.049	-0.34	2.9e-3	4.5e-3	-0.080	1.0	1.0	0.019	0.014
grcsp-9x6	0.034	-0.018	-0.33	6.1e-3	0.011	-0.088	0.99	0.99	0.023	0.026
grsn-10x6	0.030	-0.066	-0.33	3.9e-3	8.1e-3	-0.10	0.99	0.99	0.028	0.023
grsn-10x7	0.034	-0.040	-0.36	4.8e-3	0.014	-0.11	0.99	0.98	0.029	0.038
grsn-11x10	0.039	-0.025	-0.35	6.1e-3	0.019	-0.11	1.0	0.99	0.020	0.034
grsn-11x6	0.028	-0.077	-0.34	3.5e-3	5.1e-3	-0.098	0.99	0.99	0.034	0.029
grsn-11x7	0.029	-0.046	-0.41	4.0e-3	8.2e-3	-0.10	0.99	0.99	0.029	0.028
grsn-11x8	0.033	-0.043	-0.38	4.5e-3	0.013	-0.12	0.99	0.99	0.028	0.037
grsn-9x4	0.024	-0.073	-0.34	3.2e-3	6.3e-4	-0.073	0.99	0.99	0.035	0.022
grsn-9x5	0.028	-0.052	-0.40	3.9e-3	7.4e-3	-0.10	0.99	0.99	0.028	0.025
grsn-9x6	0.033	-0.052	-0.35	4.8e-3	0.011	-0.11	0.99	0.99	0.034	0.026
grsn-9x7	0.038	-0.025	-0.35	6.0e-3	0.021	-0.12	0.99	0.98	0.024	0.036
gwsddd-10x6	0.025	-0.052	-0.37	3.0e-3	6.0e-3	-0.083	0.99	0.99	0.022	0.022
gwsddd-11x7	0.028	-0.066	-0.34	3.3e-3	4.9e-3	-0.083	0.99	0.99	0.023	0.024
gwsddd-2.5x0.8	0.016	-0.076	-0.47	2.6e-3	-9.9e-3	1.0e-3	1.0	0.72	0.017	0.075
gwsddd-2.5x1	0.019	-0.089	-0.44	2.9e-3	-5.9e-3	-0.027	1.0	0.94	0.015	0.060

Table A6. Cont.

Name	C_{FT}^{static}	k^*			R^2			$nRMSE$		
		k_1	k_3	C_{MQ}^{static}	k_6	k_8	C_{FT}	C_{MQ}	C_{FT}	
gwsdd-3x2	0.035	-0.087	-0.38	5.8e-3	-8.7e-3	-0.048	1.0	0.98	0.013	0.032
gwsdd-3x3	0.050	-0.069	-0.33	0.012	-0.013	-0.055	1.0	1.0	0.010	0.015
gwsdd-4.5x3	0.031	-0.075	-0.34	4.8e-3	-5.6e-3	-0.049	1.0	0.99	0.019	0.030
gwsdd-4.5x4	0.040	-0.071	-0.27	7.6e-3	-9.3e-4	-0.068	1.0	0.98	0.016	0.039
gwsdd-4x2.5	0.033	-0.11	-0.32	5.2e-3	-0.012	-0.034	1.0	0.97	0.014	0.043
gwsdd-4x4	0.044	-0.050	-0.33	0.011	-9.7e-3	-0.058	1.0	1.0	0.014	0.016
gwsdd-5x3	0.028	-0.094	-0.30	3.9e-3	-5.0e-3	-0.047	1.0	0.98	0.014	0.036
gwsdd-5x4.3	0.040	-0.094	-0.24	7.2e-3	-7.8e-3	-0.048	0.96	0.81	0.060	0.094
gwsdd-9x5	0.026	-0.089	-0.24	3.3e-3	-3.9e-4	-0.056	0.99	0.99	0.026	0.027
gwssf-10x4.7	0.034	-0.11	-0.32	4.6e-3	-3.8e-3	-0.051	1.0	0.99	0.019	0.023
gwssf-10x8	0.040	-0.088	-0.31	6.2e-3	-2.0e-3	-0.065	1.0	0.99	0.018	0.026
gwssf-11x4.7	0.030	-0.10	-0.39	3.9e-3	-3.3e-3	-0.047	0.99	0.98	0.024	0.039
gwssf-11x8	0.039	-0.060	-0.45	6.3e-3	-2.5e-3	-0.071	0.99	0.98	0.024	0.034
gwssf-8x4.3	0.028	-0.082	-0.34	3.7e-3	-4.3e-3	-0.042	0.99	0.99	0.022	0.027
gwssf-8x6	0.037	-0.057	-0.37	5.7e-3	2.4e-3	-0.073	0.99	0.99	0.024	0.026
gwssf-9x4.7	0.031	-0.11	-0.29	4.1e-3	-5.2e-3	-0.040	0.99	0.98	0.030	0.037
gwssf-9x7	0.041	-0.077	-0.34	7.1e-3	-7.6e-3	-0.053	0.98	0.99	0.040	0.029
kavfk-11x6	0.026	-0.071	-0.29	3.5e-3	5.1e-3	-0.083	0.97	0.99	0.046	0.034
kavfk-11x7.75	0.032	-0.076	-0.23	4.5e-3	8.5e-3	-0.090	0.99	0.99	0.035	0.029
kavfk-9x4	0.019	-0.065	-0.40	2.4e-3	8.9e-4	-0.075	0.98	0.99	0.042	0.032
kavfk-9x6	0.031	-0.045	-0.33	4.8e-3	8.3e-3	-0.092	1.0	0.99	0.021	0.031
kpf-96x70	0.054	-0.10	-0.35	0.012	1.3e-3	-0.081	1.0	0.98	0.019	0.035
kyosh-10x6	0.026	-5.3e-3	-0.42	4.2e-3	7.5e-3	-0.083	1.0	0.98	0.019	0.031
kyosh-10x7	0.028	0.017	-0.42	4.4e-3	0.016	-0.095	0.98	0.94	0.035	0.061
kyosh-11x7	0.029	-0.016	-0.37	3.9e-3	0.017	-0.11	0.98	0.97	0.038	0.047
kyosh-11x9	0.029	9.9e-3	-0.33	4.9e-3	0.016	-0.083	0.98	0.93	0.033	0.057
kyosh-9x6	0.029	-0.055	-0.26	4.0e-3	0.011	-0.093	0.98	0.99	0.037	0.027
ma-11x10	0.030	0.023	-0.40	5.0e-3	0.020	-0.098	0.98	0.91	0.039	0.069
ma-11x4	0.016	-0.061	-0.49	1.9e-3	2.1e-3	-0.078	0.95	0.99	0.064	0.032
ma-11x6	0.024	-0.021	-0.51	3.0e-3	0.011	-0.11	0.97	0.97	0.048	0.050
ma-11x7	0.025	-0.029	-0.44	3.2e-3	0.011	-0.099	0.97	0.96	0.052	0.057
ma-11x8	0.028	-8.4e-4	-0.44	3.8e-3	0.017	-0.11	0.98	0.95	0.036	0.056
ma-11x9	0.029	4.5e-3	-0.40	4.2e-3	0.017	-0.097	0.99	0.94	0.031	0.053
ma-9x4	0.019	-0.037	-0.47	2.5e-3	5.6e-3	-0.087	0.97	0.97	0.052	0.045
ma-9x6	0.026	-1.6e-3	-0.46	3.7e-3	0.015	-0.11	0.97	0.96	0.044	0.050
ma-9x8	0.029	0.030	-0.42	4.8e-3	0.020	-0.10	0.99	0.93	0.033	0.066
mae-10x7	0.033	-0.028	-0.30	5.2e-3	0.012	-0.076	0.97	0.97	0.047	0.046
mae-11x7	0.032	-0.035	-0.27	5.2e-3	8.4e-3	-0.065	0.98	0.98	0.029	0.032
mae-9x6	0.028	-0.023	-0.28	5.4e-3	6.7e-3	-0.058	0.99	0.99	0.024	0.023
magf-10x6	0.026	-0.024	-0.42	3.4e-3	0.012	-0.10	0.99	0.98	0.031	0.042
magf-10x8	0.032	-0.016	-0.36	4.6e-3	0.018	-0.11	0.99	0.97	0.030	0.044
magf-11x4	0.018	-0.049	-0.46	2.0e-3	1.8e-3	-0.066	0.97	0.98	0.045	0.039
magf-11x5	0.021	-0.048	-0.42	2.5e-3	4.7e-3	-0.076	0.97	0.95	0.048	0.056
magf-11x8	0.032	-0.012	-0.39	4.5e-3	0.017	-0.11	0.99	0.97	0.030	0.041
magf-7x4	0.021	-0.053	-0.25	3.4e-3	3.7e-3	-0.070	0.98	0.99	0.033	0.029
magf-8x4	0.023	-0.050	-0.37	3.1e-3	6.7e-3	-0.090	0.99	0.99	0.034	0.028
magf-9x4	0.021	-0.052	-0.39	2.6e-3	4.0e-3	-0.080	0.98	0.97	0.045	0.045
magf-9x5	0.025	-0.040	-0.38	3.4e-3	8.2e-3	-0.091	0.98	0.98	0.037	0.036
magf-9x7	0.032	-0.018	-0.35	4.6e-3	0.016	-0.10	0.99	0.97	0.023	0.041
mas-10x5	0.024	-0.051	-0.24	3.9e-3	2.7e-3	-0.052	0.99	0.99	0.030	0.030
mas-10x7	0.029	-0.016	-0.40	4.0e-3	0.016	-0.11	0.98	0.98	0.042	0.037
mas-11x6	0.021	-0.040	-0.28	3.2e-3	7.5e-3	-0.078	0.96	0.99	0.053	0.031
mas-11x7	0.024	-0.056	-0.22	3.6e-3	6.4e-3	-0.075	0.98	0.99	0.042	0.030
mas-11x8	0.029	-0.035	-0.31	4.2e-3	0.015	-0.098	0.96	0.98	0.056	0.039
mas-9x5	0.019	-0.045	-0.22	3.3e-3	6.0e-3	-0.072	0.98	1.0	0.033	0.017
mas-9x6	0.025	-0.050	-0.23	3.9e-3	7.1e-3	-0.075	0.98	0.99	0.040	0.025
mas-9x7	0.030	-0.056	-0.23	4.5e-3	0.010	-0.082	0.98	0.99	0.037	0.022

Table A6. Cont.

Name	k*			R ²			nRMSE			
	C _{FT} ^{static}	k ₁	k ₃	C _{MQ} ^{static}	k ₆	k ₈	C _{FT}	C _{MQ}	C _{FT}	C _{MQ}
mi-3.2x2.2	0.031	-0.080	-0.32	4.6e-3	-6.5e-3	-0.021	0.98	0.93	0.041	0.056
mi-4x2.7	0.026	-0.075	-0.41	4.2e-3	-7.0e-3	-0.026	0.98	0.73	0.036	0.12
mi-5x3.5	0.025	-0.11	-0.45	3.3e-3	-0.015	0.027	0.98	0.80	0.041	0.11
mit-4.3x3.5	0.041	-0.048	-0.80	7.3e-3	-4.6e-3	-0.093	0.98	0.92	0.036	0.072
mit-5x4	0.047	-0.047	-0.53	9.7e-3	-7.7e-3	-0.074	1.0	0.99	0.021	0.027
pl-100x80	0.033	6.2e-3	-0.41	6.9e-3	7.9e-3	-0.088	0.99	0.98	0.026	0.040
pl-57x20	0.036	-0.074	-0.38	6.0e-3	7.8e-3	-0.083	1.0	0.96	8.5e-3	0.056
rusp-11x4	0.019	-0.071	-0.30	2.4e-3	5.8e-5	-0.057	0.98	0.99	0.040	0.025
vp-140x45	0.016	-0.063	-0.45	1.8e-3	-4.6e-3	-0.017	0.99	0.96	0.036	0.048
zin-11x7	0.021	-0.053	-0.24	3.7e-3	2.8e-3	-0.065	0.99	1.0	0.028	0.017
zin-9x6	0.022	-0.050	-0.24	4.2e-3	4.4e-3	-0.066	0.99	1.0	0.021	0.013

Appendix B. Remaining Partial Derivatives from Section 5

$$\Lambda := \sqrt{(\delta - 1)\sigma(-8c_{l,0}(1 + \delta) + c_{l,\alpha}(c_{l,\alpha}(\delta - 1)\sigma - 16\theta_{\text{tip}}))} \quad (\text{A1})$$

$$\frac{\partial C_{FH}^x}{\partial \lambda_c} \Big|_{\lambda_c=0, \mu=0} = 0 \quad (\text{A2})$$

$$\frac{\partial C_{FH}^x}{\partial \mu} \Big|_{\lambda_c=0, \mu=0} = -\frac{1}{2\delta}\sigma((\delta - 1)(2c_{d,0}\delta + \theta_{\text{tip}}(-(2c_{d,\alpha} - c_{l,\alpha})\lambda_i(0,0) + 2c_{d,\alpha}\theta_{\text{tip}})) + \quad (\text{A3})$$

$$c_{l,0}\delta\lambda_i(0,0)\ln(\delta)) \quad (\text{A4})$$

$$\frac{\partial^2 C_{FH}^x}{\partial \lambda_c^2} \Big|_{\lambda_c=0, \mu=0} = 0 \quad (\text{A5})$$

$$\frac{\partial^2 C_{FH}^x}{\partial \lambda_c \partial \mu} \Big|_{\lambda_c=0, \mu=0} = -\frac{2\sigma\lambda_i(0,0)((-2c_{d,\alpha} - c_{l,\alpha})(\delta - 1)\theta_{\text{tip}} + c_{l,0}\delta\ln(\delta))}{4\delta\Lambda} \quad (\text{A6})$$

$$\frac{\partial^2 C_{FH}^x}{\partial \mu^2} \Big|_{\lambda_c=0, \mu=0} = 0 \quad (\text{A7})$$

$$\frac{\partial C_{MQ}^x}{\partial \lambda_c} \Big|_{\lambda_c=0, \mu=0} = ((\delta - 1)\sigma\lambda_i(0,0)(-2c_{l,0}(1 + \delta) + c_{d,\alpha}c_{l,\alpha}\sigma - c_{l,\alpha}^2\sigma - c_{d,\alpha}c_{l,\alpha}\delta\sigma + c_{l,\alpha}^2\delta\sigma + \quad (\text{A8})$$

$$8c_{d,\alpha}\theta_{\text{tip}} - 4c_{l,\alpha}\theta_{\text{tip}} - c_{d,\alpha}\Lambda + c_{l,\alpha}\Lambda)) / \Lambda \quad (\text{A9})$$

$$\frac{\partial C_{MQ}^x}{\partial \mu} \Big|_{\lambda_c=0, \mu=0} = 0 \quad (\text{A10})$$

$$\frac{\partial^2 C_{MQ}^x}{\partial \lambda_c^2} \Big|_{\lambda_c=0, \mu=0} = ((\delta - 1)^2\sigma^2(8c_{l,0}^2(1 + \delta)^2 - 4c_{l,0}(-c_{d,\alpha} + c_{l,\alpha})(1 + \delta)(3c_{l,\alpha}(\delta - 1)\sigma + \quad (\text{A11})$$

$$2(\Lambda - 4\theta_{\text{tip}})) + c_{l,\alpha}(c_{l,\alpha}^2(\delta - 1)^2\sigma^2 + c_{l,\alpha}(\delta - 1)\sigma(\Lambda - 24\theta_{\text{tip}}) + \quad (\text{A12})$$

$$16\theta_{\text{tip}}(-\Lambda + 2\theta_{\text{tip}})) - c_{d,\alpha}(c_{l,\alpha}^2(\delta - 1)^2\sigma^2 + c_{l,\alpha}(\delta - 1)\sigma(\Lambda - 24\theta_{\text{tip}}) + \quad (\text{A13})$$

$$16\theta_{\text{tip}}(-\Lambda + 4\theta_{\text{tip}}))) / \Lambda^3 \quad (\text{A14})$$

$$\frac{\partial^2 C_{MQ}^x}{\partial \lambda_c \partial \mu} \Big|_{\lambda_c=0, \mu=0} = 0 \quad (\text{A15})$$

$$\frac{\partial^2 C_{MQ}^x}{\partial \mu^2} \Big|_{\lambda_c=0, \mu=0} = -((\delta - 1)\sigma(2(c_{d,0}\delta + c_{d,\alpha}\theta_{\text{tip}}^2)\Lambda - c_{l,0}(1 + \delta)\sigma(c_{l,\alpha}(\delta - 1)\theta_{\text{tip}} + \quad (\text{A16})$$

$$c_{l,0}\delta \ln(\delta)) + 2\sigma(c_{l,\alpha}\lambda_i(0,0) - c_{d,\alpha}(\lambda_i(0,0) - \theta_{\text{tip}}))(c_{l,\alpha}(\delta - 1)\theta_{\text{tip}} + \dots) \quad (\text{A17})$$

$$c_{l,0}\delta \ln(\delta)) - 2(c_{d,\alpha} - c_{l,\alpha})\sigma(\lambda_i(0,0) - \theta_{\text{tip}})(c_{l,\alpha}(\delta - 1)\theta_{\text{tip}} + \dots) \quad (\text{A18})$$

$$c_{l,0}\delta \ln(\delta))) / (2\delta\Lambda) \quad (\text{A19})$$

$$\frac{\partial C_{MR}^x}{\partial \lambda_c} \Big|_{\lambda_c=0, \mu=0} = 0 \quad (\text{A20})$$

$$\frac{\partial C_{MR}^x}{\partial \mu} \Big|_{\lambda_c=0, \mu=0} = \frac{1}{16}(\delta - 1)\sigma(-8c_{l,0}(1 + \delta) + c_{l,\alpha}(8\lambda_i(0,0) - 16\theta_{\text{tip}})) \quad (\text{A21})$$

$$\frac{\partial^2 C_{MR}^x}{\partial \lambda_c^2} \Big|_{\lambda_c=0, \mu=0} = 0 \quad (\text{A22})$$

$$\frac{\partial^2 C_{MR}^x}{\partial \lambda_c \partial \mu} \Big|_{\lambda_c=0, \mu=0} = \frac{1}{16}c_{l,\alpha}(\delta - 1)\sigma\left(4 + \frac{4c_{l,\alpha}(\delta - 1)\sigma}{\Lambda}\right) \quad (\text{A23})$$

$$\frac{\partial^2 C_{MR}^x}{\partial \mu^2} \Big|_{\lambda_c=0, \mu=0} = 0 \quad (\text{A24})$$

$$\frac{\partial C_{MP}^x}{\partial \lambda_c} \Big|_{\lambda_c=0, \mu=0} = 0 \quad (\text{A25})$$

$$\frac{\partial C_{MP}^x}{\partial \mu} \Big|_{\lambda_c=0, \mu=0} = \frac{c_{\text{tip}}\sigma(c_{m,\alpha}(\delta - 1)(8\lambda_i(0,0) - 16\theta_{\text{tip}}) - 16c_{m,0}\delta \ln(\delta))}{16\delta R} \quad (\text{A26})$$

$$\frac{\partial^2 C_{MP}^x}{\partial \lambda_c^2} \Big|_{\lambda_c=0, \mu=0} = 0 \quad (\text{A27})$$

$$\frac{\partial^2 C_{MP}^x}{\partial \lambda_c \partial \mu} \Big|_{\lambda_c=0, \mu=0} = \frac{c_{m,\alpha}c_{\text{tip}}(\delta - 1)\sigma\left(4 + \frac{4c_{l,\alpha}(\delta - 1)\sigma}{\Lambda}\right)}{16\delta R} \quad (\text{A28})$$

$$\frac{\partial^2 C_{MP}^x}{\partial \mu^2} \Big|_{\lambda_c=0, \mu=0} = 0 \quad (\text{A29})$$

References

- Ragni, D.; van Oudheusden, B.W.; Scarano, F. Non-intrusive aerodynamic loads analysis of an aircraft propeller blade. *Exp. Fluids* **2011**, *51*, 361–371. doi:10.1007/s00348-011-1057-7. [[CrossRef](#)]
- Westmoreland, W.; Tramel, R.; Barber, J. Modeling Propeller Flow-Fields Using CFD. In 46th AIAA Aerospace Sciences Meeting and Exhibit, Reno, NV, USA, 7–10 January 2008.
- Favier, D.; Maresca, C.; Fratello, G. Experimental and numerical study of the propeller/fixed wing interaction. *J. Aircr.* **1991**, *28*, 365–373. doi:10.2514/3.46036. [[CrossRef](#)]
- Rothhaar, P.M.; Murphy, P.C.; Bacon, B.J.; Gregory, I.M.; Grauer, J.A.; Busan, R.C.; Croom, M.A. NASA Langley Distributed Propulsion VTOL TiltWing Aircraft Testing, Modeling, Simulation, Control, and Flight Test Development. In Aviation Technology, Integration, and Operations Conference, Atlanta, GA, USA, 16–20 June 2014.
- Theys, B.; Dimitriadis, G.; Hendrick, P.; De Schutter, J. Experimental and numerical study of micro-aerial-vehicle propeller performance in oblique flow. *J. Aircr.* **2017**, *54*, 1076–1084. doi:10.2514/1.C033618. [[CrossRef](#)]
- Khan, W.; Nahon, M. Modeling and Control of a Highly-Maneuverable Fixed-Wing UAV. In *CASI 60th Aeronautics Conference and AGM (Aero13): Aerospace Clusters: Where are we Headed*; CASI: Quebec City, QC, Canada, 2012.
- Theys, B.; Dimitriadis, G.; Andrianne, T.; Hendrick, P.; De Schutter, J. Wind tunnel testing of a VTOL MAV propeller in tilted operating mode. In Proceedings of the International Conference on Unmanned Aircraft Systems, Orlando, FL, USA, 27–30 May 2014.

8. Sartori, D.; Wou, D.; Pei, L.; Yu, W. A Revisited Approach to Lateral Acceleration Modeling for Quadrotor UAVs State Estimation. In Proceedings of the IEEE/RSJ International Conference on Intelligent Robots and Systems, Madrid, Spain, 1–5 October 2018.
9. Martin, P.; Salaün, E. The true role of accelerometer feedback in quadrotor control. In *IEEE International Conference on Robotics and Automation*; IEEE: Anchorage, AK, USA, 2018.
10. Leishman, R.C.; Macdonald, J.C.; Beard, R.W.; McLain, T.W. Quadrotors and Accelerometers: State Estimation with an Improved Dynamic Model. *IEEE Control Syst. Mag.* **2014**, *34*, 28–41. doi:10.1109/MCS.2013.2287362. [[CrossRef](#)]
11. Padfield, G.D. *Helicopter Flight Dynamics*; John Wiley & Sons: Chichester, UK, 2008.
12. Talbot, P.D.; Corliss, L.D. A mathematical force and moment model of a uh-1h helicopter for flight dynamics simulations. *NASA Tech. Rep.* **73254**. **1977**.
13. Sun, S.; de Visser, C.C.; Chu, Q. Quadrotor Gray-Box Model Identification from High-Speed Flight Data. *J. Aircr.* **2019**, *56*, 645–661. [[CrossRef](#)]
14. Sartori, D.; Yu, W. Experimental Characterization of a Propulsion Systems for Multi-rotor UAVs. *J. Intell. Robot. Syst.* **2019**. [[CrossRef](#)]
15. Gill, R.; D’Andrea, R. Propeller thrust and drag in forward flight. In *IEEE Conference on Control Technology and Applications*; IEEE: Mauna Lani, HI, USA, 2017.
16. Amir, M.Y.; Abbass, V. Modeling of Quadrotor Helicopter Dynamics. In *International Conference on Smart Manufacturing Application*; IEEE: Gyeonggi-do, Korea, 2008.
17. Mellinger, D.; Michael, N.; Kumar, V. Trajectory generation and control for precise aggressive maneuvers with quadrotors. *Int. J. Robot. Res.* **2012**, *31*, 664–674. doi:10.1177/0278364911434236. [[CrossRef](#)]
18. Wang, J.; Bierling, T.; Achtelik, M.; Hocht, L.; Holzapfel, F.; Zhao, W.; Hiong, G.T. Attitude free position control of a quadcopter using dynamic inversion. *AIAA Infotech@ Aerosp.* **2011**, 29–31. doi:10.2514/6.2011-1583. [[CrossRef](#)]
19. Schulz, M.; Augugliaro, F.; Ritz, R.; D’Andrea, R. High-speed, steady flight with a quadrocopter in a confined environment using a tether. In *IEEE/RSJ International Conference on Intelligent Robots and Systems*; IEEE: Hamburg, Germany, 2015.
20. Bouadi, H.; Bouchoucha, M.; Tadjine, M. Modelling and stabilizing control laws design based on backstepping for an UAV type-quadrotor. *IFAC Proc. Vol.* **2007**, *40*, 245–250. doi:10.3182/20070903-3-FR-2921.00043. [[CrossRef](#)]
21. Fernando, H.C.T.E.; De Silva, A.T.A.; De Zoysa, M.D.C.; Dilshan, K.A.D.C.; Munasinghe, S.R. Modelling, simulation and implementation of a quadrotor UAV. In *IEEE 8th International Conference on Industrial and Information Systems*; IEEE: Peradeniya, Sri Lanka, 2013.
22. Koehl, A.; Rafaralahy, H.; Boutayeb, M.; Martinez, B. Aerodynamic Modelling and Experimental Identification of a Coaxial-Rotor UAV. *J. Intell. Robot. Syst.* **2012**, *68*, 53–68. doi:10.1007/s10846-012-9665-x. [[CrossRef](#)]
23. Ansari, U.; Bajodah, A.H.; Hamayun, M.T. Quadrotor Control Via Robust Generalized Dynamic Inversion and Adaptive Non-Singular Terminal Sliding Mode. *Asian J. Control* **2019**, *21*, 1237–1249. doi:10.1002/asjc.1800. [[CrossRef](#)]
24. Wang, S.; Polyakov, A.; Zheng, G. Quadrotor Control Design under Time and State Constraints: Implicit Lyapunov Function Approach. In Proceedings of the European Control Conference; Naples, Italy, 25–28 June 2019.
25. Mohammed, R. Quadrotor Control Using Fractional-Order $PI^{\lambda}D^{\mu}$ Control. *J. Adv. Comp. Eng. Tech.* **2019**, *5*, 1–10.
26. Malo Tamayo, A.J.; Villaseñor Ríos, C.A.; Ibarra Zannatha, J.M.; Orozco Soto, S.M. Quadrotor Input-Output Linearization and Cascade Control. *IFAC-Pap. OnLine* **2018**, *51*, 437–442. doi:10.1016/j.ifacol.2018.07.317. [[CrossRef](#)]
27. Kun, D.W.; Hwang, I. Linear Matrix Inequality-Based Nonlinear Adaptive Robust Control of Quadrotor. *J. Guid. Control Dyn.* **2016**, *39*, 996–1008. doi:10.2514/1.G001439. [[CrossRef](#)]
28. Stepaniak, M.J.; Van Graas, F.; De Haag, M.U. Design of an Electric Propulsion System for a Quadrotor Unmanned Aerial Vehicle. *J. Aircr.* **2009**, *46*, 1050–1058. doi:10.2514/1.38409. [[CrossRef](#)]

29. Alkowatly, M.T.; Becerra, V.M.; Holderbaum, W. Bioinspired Autonomous Visual Vertical Control of a Quadrotor Unmanned Aerial Vehicle. *J. Guid. Control Dyn.* **2015**, *38*, 249–262. doi:10.2514/1.G000634. [CrossRef]
30. Lu, Q.; Ren, B.; Parameswaran, S. Shipboard Landing Control Enabled by an Uncertainty and Disturbance Estimator. *J. Guid. Control Dyn.* **2018**, *41*, 1502–1520. doi:10.2514/1.G003073. [CrossRef]
31. Alabsi, M.I.; Fields, T.D. Real-Time Closed-Loop System Identification of a Quadcopter. *J. Aircr.* **2019**, *56*, 324–335. doi:10.2514/1.C034219 [CrossRef]
32. Bouadi, H.; Mora-Camino, F. Modeling and Adaptive Flight Control for Quadrotor Trajectory Tracking. *J. Aircr.* **2018**, *55*, 666–681. doi:10.2514/1.C034477. [CrossRef]
33. Dawkins, J.; DeVries, L. Modeling, Trim Analysis, and Trajectory Control of a Micro-Quadrotor with Wings. *Drones* **2018**, *2*, 21. doi:10.3390/drones2020021. [CrossRef]
34. Leishman, J.G. *Principles of Helicopter Aerodynamics*, 2nd ed.; Cambridge University Press: Cambridge, MA, USA, 2006.
35. McCormick, B.W. *Aerodynamics of V/STOL Flight*; Academic Press Inc.: Cambridge, MA, USA, 1967.
36. Wheatley, J.B. *An Aerodynamic Analysis of the Autogiro Rotor with a Comparison between Calculated and Experimental Results*; NACA Technical Report 487; Langley Aeronautical Lab, National Advisory Committee for Aeronautics: Hampton, VA, USA, 1935.
37. Rich, M. Model Development, System Identification, and Control of a Quadrotor Helicopter. Master' dissertation, Iowa State University, Ames, IA, USA, 2012.
38. Hoffmann, G.; Huang, H.; Waslander, S.; Tomlin, C. Quadrotor Helicopter Flight Dynamics and Control: Theory and Experiment. In *AIAA Guidance, Navigation and Control Conference and Exhibit*; AIAA: Hilton Head, SC, USA, 2012.
39. Mohiuddin, A.; Taha, T.; Zweiri, Y.; Gan, D. UAV Payload Transportation via RTDP Based Optimized Velocity Profiles. *Energies* **2019**, *12*, 16. doi:10.3390/en12163049. [CrossRef]
40. Fay, G. Derivation of the aerodynamic forces for the mesicopter simulation. *Standord Univ.* **2001**. Available online: <https://media.gradebuddy.com/documents/340594/59482841-8400-4d1d-890d-8932a64a24d1.pdf> (accessed on 1 September 2019).
41. Bouabdallah, S.; Siegwart, R. Full control of a quadrotor. In *International Conference on Intelligent Robots and Systems*; IEEE: San Diego, CA, USA, 2007.
42. González-Rocha, J.; Woolsey, C.A.; Sultan, C.; De Wekker, S.F.J. Sensing Wind from Quadrotor Motion. *J. Guid. Control Dyn.* **2019**, *42*, 836–852. doi:10.2514/1.G003542. [CrossRef]
43. Quigley, M.; Goodrich, M.A.; Griffiths, S.; Eldredge, A.; Beard, R.W. Target Acquisition, Localization, and Surveillance Using a Fixed-Wing Mini-UAV and Gimbaled Camera. In *IEEE International Conference on Robotics and Automation*; IEEE: Barcelona, Spain, 2005.
44. Laiacker, M.; Kondak, K.; Schwarzbach, M.; Muskardin, T. Vision aided automatic landing system for fixed wing UAV. In *IEEE/RSJ International Conference on Intelligent Robots and Systems*; IEEE: Tokyo, Japan, 2013.
45. Escareño, J.; Stone, R.H.; Sanchez, A.; Lozano, R. Modeling and control strategy for the transition of a convertible tail-sitter UAV. In *European Control Conference*; IEEE: Kos, Greece, 2007.
46. Bayraktar, S.; Fainekos, G.E.; Pappas, G.J. Experimental cooperative control of fixed-wing unmanned aerial vehicles. In *43rd IEEE Conference on Decision and Control*; IEEE: Nassau, Bahamas, 2004.
47. Kohno, S.; Uchiyama, K. Design of robust controller of fixed-wing UAV for transition flight. In *International Conference on Unmanned Aircraft Systems*; IEEE: Orlando, FL, USA, 2014.
48. Lozano, R. *Unmanned Aerial Vehicles: Embedded Control*; John Wiley & Sons: Hoboken, NJ, USA, 2013.
49. Oner, K.T.; Cetinsoy, E.; Sirimoglu, E.; Hancer, C.; Unel, M.; Aksit, M.F.; Gulez, K.; Kandemir, I. Mathematical modeling and vertical flight control of a tilt-wing UAV. *Turk. J. Electr. Eng. Comp. Sci.* **2012**, *20*, 149–157.
50. Knoebel, N.; Osborne, S.; Snyder, D.; McLain, T.; Beard, R.; Eldredge, A. Preliminary Modeling, Control, and Trajectory Design for Miniature Autonomous Tailsitters. In *AIAA Guidance, Navigation, and Control Conference and Exhibit*; AIAA: Keystone, CO, USA, 2012.
51. Luo, Y.; Chao, H.; Di, L.; Chen, Y.Q. Lateral directional fractional order (PI) α control of a small fixed-wing unmanned aerial vehicles: controller designs and flight tests. *IET Control Theory Appl.* **2011**, *5*, 2156–2167. [CrossRef]

52. De Blauwe, H.; Bayraktar, S.; Feron, E.; Lokumcu, F. Flight Modeling and Experimental Autonomous Hover Control of a Fixed Wing Mini-UAV at High Angle of Attack. In *AIAA Guidance, Navigation and Control Conference and Exhibit*; AIAA: Hilton Head, SC, USA, 2012.
53. Venkataraman, R.; Seiler, P. System Identification for a Small, Rudderless, Fixed-Wing Unmanned Aircraft. *J. Aircr.* **2019**, *56*, 1126–1134. doi:10.2514/1.C035141. [CrossRef]
54. Dorobantu, A.; Murch, A.; Mettler, B.; Balas, G. System Identification for Small, Low-Cost, Fixed-Wing Unmanned Aircraft. *J. Aircr.* **2013**, *50*, 1117–1130. doi:10.2514/1.C032065. [CrossRef]
55. Waszak, M.; Davidson, J.; Ifju, P. Simulation and Flight Control of an Aeroelastic Fixed Wing Micro Aerial Vehicle. In *AIAA Atmospheric Flight Mechanics Conference and Exhibit*; AIAA: Monterey, CA, USA, 2012.
56. Triputra, F.; Trilaksono, B.; Adiono, T.; Sasongko, R.; Dahsyat, M. Nonlinear Dynamic Modeling of a Fixed-Wing Unmanned Aerial Vehicle: A Case Study of Wulung. *J. Mechatron. Electr. Power Veh. Technol.* **2015**, *6*, 19–30. doi:10.14203/j.mev.2015.v6.19-30. [CrossRef]
57. Yuksek, B.; Vuruskan, A.; Ozdemir, U.; Yukselen, M.A.; Inalhan, G. Transition flight modeling of a fixed-wing VTOL UAV. *J. Intel. Robot. Syst.* **2016**, *84*, 83–105. doi:10.1007/s10846-015-0325-9 [CrossRef]
58. Selig, M. Modeling full-envelope aerodynamics of small UAVs in realtime. In *AIAA Atmospheric Flight Mechanics Conference*; AIAA: Toronto, ON, Canada, 2010.
59. Beard, R.W.; McLain, T.W. *Small Unmanned Aircraft: Theory and Practice*; Princeton University Press: Princeton, NJ, USA, 2012.
60. Liu, C.; Chen, W.-H. Disturbance Rejection Flight Control for Small Fixed-Wing Unmanned Aerial Vehicles. *J. Guid. Control Dyn.* **2016**, *39*, 2810–2819. doi:10.2514/1.G001958. [CrossRef]
61. Verling, S.; Weibel, B.; Boosfeld, M.; Alexis, K.; Burri, M.; Siegwart, R. Full Attitude Control of a VTOL tailsitter UAV. In *IEEE International Conference on Robotics and Automation*; IEEE: Stockholm, Sweden, 2016.
62. Powers, C.; Mellinger, D.; Kushleyev, A.; Kothmann, B.; Kumar, V. Influence of aerodynamics and proximity effects in quadrotor flight. In *Experimental Robotics*; Springer: Heidelberg, Germany, 2013. doi:10.1007/978-3-319-00065-7_21. [CrossRef]
63. Kaya, D.; Kutay, A.T. Aerodynamic modeling and parameter estimation of a quadrotor helicopter. In *AIAA Atmospheric Flight Mechanics Conference*; AIAA: Atlanta, GA, USA, 2014.
64. Phung, D.-K.; Morin, P. Modeling and Energy Evaluation of Small Convertible UAVs. *IFAC Proc. Vol.* **2013**, *46*, 212–219. doi:10.3182/20131120-3-FR-4045.00004. [CrossRef]
65. Khan, W.; Nahon, M. A propeller model for general forward flight conditions. *Int. J. Intell. Unmanned Syst.* **2015**, *3*, 72–92. doi:10.1108/IJIUS-06-2015-0007. [CrossRef]
66. Orsag, M.; Bogdan, S. *Influence of Forward and Descent Flight on Quadrotor Dynamics*; INTECH Open Access: London, UK, 2012.
67. Russell, C.R.; Jung, J.; Willink, G.; Glasner, B. Wind tunnel and hover performance test results for multicopter UAS vehicles. In *72nd AHS Int. Annu. Forum Technol. Disp.*; AHS: West Palm Beach, FL, USA, 2016.
68. Brandt, J.B.; Deters, R.W.; Ananda, G.K.; Selig, M.S. UIUC Propeller Data Site. Available online: <http://m-selig.ae.illinois.edu/props/propDB.html> (accessed on 7 July 2016).
69. Deters, R.W.; Krishnan, A.; Kumar, G.; Selig, M.S. Reynolds number effects on the performance of small-scale propellers. In *32nd AIAA Applied Aerodynamics Conference*; AIAA: Atlanta, GA, USA, 2014.
70. Darmofal, D.; Drela, M.; Uranga, A. *Introduction to Aerodynamics - Lecture Notes*; Massachusetts Institute of Technology: Cambridge, MA, USA, 2016.
71. Vahid, O.; Eslaminasab, N.; Golnaraghi, M.F. Friction-induced vibration in lead screw systems: mathematical modeling and experimental studies. *J. Vib. Acoust.* **2009**, *131*, 021003. doi:10.1115/1.3025837. [CrossRef]
72. Kamalzadeh, A.; Erkorkmaz, K. Accurate tracking controller design for high-speed drives. *Intern. J. Mach. Tools Manuf.* **2007**, *47*, 1393–1400. doi:10.1016/j.ijmachtools.2006.08.027. [CrossRef]
73. Medeiros, V.; Ramon, L.; Ramos, G.S.; Gabriel, J.; Nascimento, T.P.; C. Lima Filho, A.; Brito, A.V. A Novel Approach for Brushless DC Motors Characterization in Drones Based on Chaos. *Drones* **2018**, *2*, 2. doi:10.3390/drones2020014. [CrossRef]
74. Jones, E.; Oliphant, T.; Peterson, P. SciPy: Open Source Scientific Tools for Python. Available online: <http://www.scipy.org/> (accessed on 1 February 2019).
75. Storn, R.; Price, K. Differential evolution—A simple and efficient heuristic for global optimization over continuous spaces. *J. Glob. Optim.* **1997**, *11*, 341–359. doi:10.1023/A:1008202821328. [CrossRef]

76. Alexander, D.L.J.; Tropsha, A.; Winkler, D.A. Beware of R²: Simple, Unambiguous Assessment of the Prediction Accuracy of QSAR and QSPR Models. *J. Chem. Inf. Model.* **2015**, *55*, 1316–1322. doi:10.1021/acs.jcim.5b00206. [[CrossRef](#)]
77. Shcherbakov, M.V.; Brebels, A.; Shcherbakova, N.L.; Tyukov, A.P.; Janovsky, T.A.; Kamaev, V.A. A survey of forecast error measures. *World Appl. Scie. J.* **2013**, *24*, 171–176. doi:0.5829/idosi.wasj.2013.24.itmies.80032. [[CrossRef](#)]
78. *Propeller Geometry: Terms and Definitions*; Michigan Wheel Engineering, Federal Propellers: Grand Rapids, MI, USA, 2000.
79. Rechs, R.J. *An Introduction to Muscle Powered Ultra-Light Gas Blimps*; Marc de Piolenc: Iligan City, Philippines, 1998.
80. Chovancová, A.; Fico, T.; Chovanec, L.; Hubinsk, P. Mathematical Modelling and Parameter Identification of Quadrotor (a survey). *Procedia Eng.* **2014**, *96*, 172–181. doi:10.1016/j.proeng.2014.12.139. [[CrossRef](#)]
81. Diamond, S.; Boyd, S. CVXPY: A Python-Embedded Modeling Language for Convex Optimization. *J. Mach. Learn. Res.* **2016**, *17*, 1–5.
82. Agrawal, A.; Verschueren, R.; Diamond, S.; Boyd, S. A Rewriting System for Convex Optimization Problems. *J. Control Dec.* **2018**, *5*, 42–60. [[CrossRef](#)]



© 2019 by the authors. Licensee MDPI, Basel, Switzerland. This article is an open access article distributed under the terms and conditions of the Creative Commons Attribution (CC BY) license (<http://creativecommons.org/licenses/by/4.0/>).